# Innovative Approaches in Spectral Flow Cytometry

ARTICLE COLLECTION


WILEY | CURRENT PROTOCOLS A Wiley Brand | Cytometry PART A ISAC Journal of Quantitative Cell Science

Sponsored by: CYTEK®

# Contents

# Introduction

Until recently, scientists have been limited in the number of fluorochromes they can analyze per sample on their conventional flow cytometer, due in part to the availability of spectrally resolvable dyes and the detection limits of the hardware. Over the past several decades, there have been significant advances in available reagents and dye chemistry, with hardware sticking to the same paradigm of designating one primary detector per color. With spectral flow cytometry, the entire emission spectrum of the dye can now be measured and analyzed, allowing for both improved resolution of markers and higher dimensional experiments.

In this collection, we present a series of research articles detailing applications and innovative approaches enabled by spectral flow cytometry. Deep immunophenotying can be done using both conventional and spectral flow cytometry. In Niewold et al (2020), they directly compare conventional and spectral flow cytometry using a series of benchmark tests for different signal attributes, signal analysis methods, and application to complex panels and different sample types. Their analytic comparison found that the spectral approaches displayed clear advantages in detection and analysis over conventional flow cytometry approaches. Similarly, Soh et al (2022) take advantage of the increased resolution afforded by spectral flow cytometry to address therapeutic outcomes in acute myeloid leukemia (AML). Determining the effectiveness of therapeutic intervention in AML through the identification of residual myeloid leukemic cells has become a key prognostic indicator for hematological diseases but presents several challenges. The group evaluates a 27-marker panel for the detection of residual leukemic cells after treatment for AML utilizing spectral flow cytometry, obtaining the ability to distinguish cells in a normally heterogenous population consistently.

With the ability to resolve the full spectrum of a fluorochrome even ones with similar peak emission, spectral flow cytometry has empowered novel applications. For example, one means for identifying multiple samples at the same time is to employ a system known as “barcoding”. In the case of peripheral blood mononuclear cells (PBMCs), using different antibodies to CD45 can be used for the barcode system. In Junker and Teixeira (2021), created a barcoding protocol that allows for simultaneous analysis of PBMCs from 20 individual donors and measure changes in a mode of action study in unfixed cells. More challenging cell populations can also be visualized in high-dimensional panels with spectral flow cytometry. For cell-based therapies, engraftment pools of hematopoietic stem cells (HSCs) can come from different sources such as bone marrow and cord blood that requires thorough characterization. A third but less accessible population is from fetal liver, which has been noted to display superior engraftment potential compared to the others. In order to characterize this cell population, Vanuytsel et al (2022) reports on a novel high-dimensional panel to evaluate the engraftment potential of HSCs from fetal liver. Finally, cell-based reporter assays, such as Förster resonance energy transfer (FRET), are also unlocked thanks to spectral flow cytometry. Henderson et al (2021) show that both conventional flow cytometry and spectral flow cytometry can be used with FRET-based sensors for enzymatic activity of protein kinases, interrogating signal pathways and changes in cellular activity. They conclude that spectral flow cytometry allowed for real-time measurement of FRET with greater resolution compared to conventional flow cytometry.

In summary, this article collection will educate the reader as to recent innovations in the applications empowered by spectral flow cytometry, from measurements of cellular activity to the evaluation of therapeutic interventions. As new methodologies emerge that utilize the flexibility and capabilities of spectral flow cytometry are developed, researchers will be able to gain greater biological insights into cell biology and disease.

By Jeremy Petravicz, PhD, Senior Editor,
*Current Protocols*

# References


Niewold, P., Ashhurst, T.M., Smith, A.L. and King, N.J.C. (2020), Evaluating spectral cytometry for immune profiling in viral disease. *Cytometry*, 97: 1165-1179. https://doi.org/10.1002/cyto.a.24211

Soh, KT, Conway, A, Liu, X, Wallace, PK. Development of a 27-color panel for the detection of measurable residual disease in patients diagnosed with acute myeloid leukemia. *Cytometry*. 2022. https://doi.org/10.1002/cyto.a.24667

Junker, F, Camillo Teixeira, P. Barcoding of live peripheral blood mononuclear cells to assess immune cell phenotypes using full spectrum flow cytometry. *Cytometry*. 2022; https://doi.org/10.1002/cyto.a.24543

Vanuytsel, K, Yeung, AK, Dowrey, TW, Murphy, GJ, Belkina, AC. Comprehensive phenotyping of hematopoietic stem and progenitor cells in the human fetal liver. *Cytometry*. 2022; 1– 6. https://doi.org/10.1002/cyto.a.24540

Henderson, J, Havranek, O, Ma, MCJ, et al. Detecting Förster resonance energy transfer in living cells by conventional and spectral flow cytometry. *Cytometry*. 2022; 101: 818– 834. https://doi.org/10.1002/cyto.a.24472

# EMPOWERING YOUR DISCOVERY

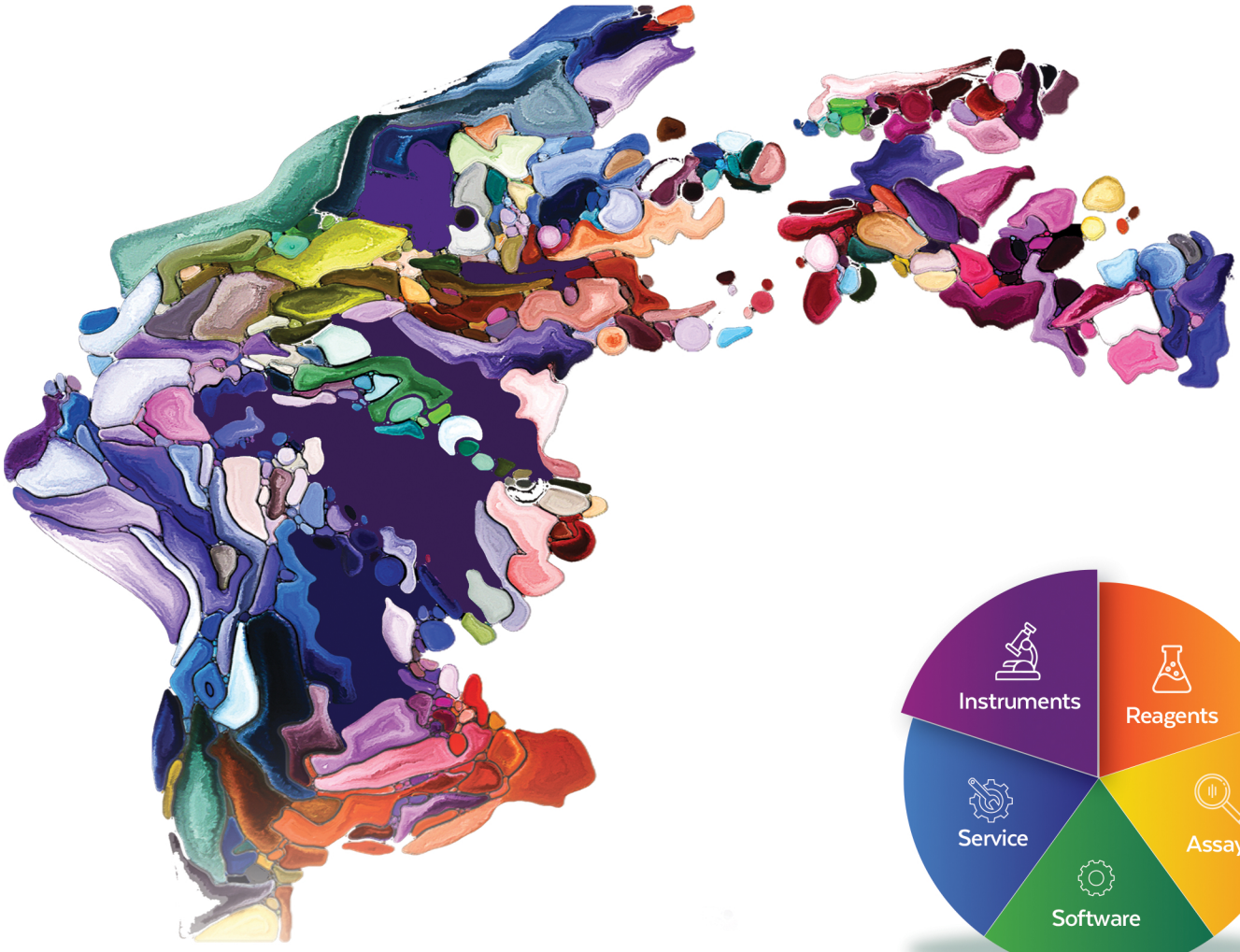

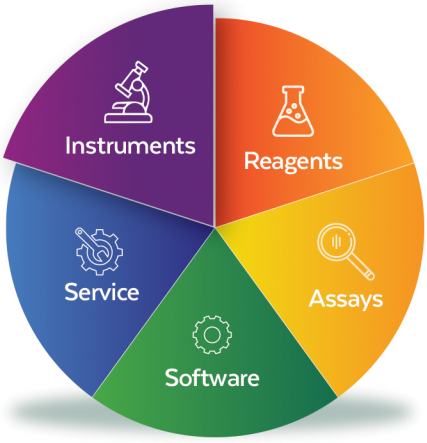


## Cytek® Northern Lights™ System

Full spectrum flow cytometry empowers your single cell discovery - with fewer hurdles and easy-to-follow workflows. Join leading scientists and researchers at academic and pharmaceutical institutions who are accelerating time to insight with flexible panel design and expanded reagent options.

- **Ease-of-use:** Cytek Assay Settings come with every system, simplifying instrument setup and removing the need to optimize individual detectors.
- **Compatibility with Existing Panels:** Capable of running any assay from your current 1-3 laser system.
- **Enhanced Sensitivity and Resolution:** Easily gate and resolve rare and dim cell populations.

There has never been a better time to join the shift to Full Spectrum Profiling™ (FSP™).


CYTEK®
TRANSCEND THE CONVENTIONAL
cytekbio.com

ISAC CYTOMETRY Journal of Quantitative Cell Science PART A

MIFlowCyt

# Evaluating spectral cytometry for immune profiling in viral disease

Paula Niewold,[1†] Thomas Myles Ashhurst,[2†] Adrian Lloyd Smith,[2] Nicholas Jonathan Cole King[1,2*]

[1]Discipline of Pathology, Charles Perkins Centre, The Faculty of Medicine and Health, Camperdown, New South Wales, Australia

[2]Sydney Cytometry Core Research Facility, Charles Perkins Centre, The Centenary Institute and The University of Sydney, Johns Hopkins Drive, Camperdown, New South Wales, Australia

Received 4 November 2019; Revised 23 June 2020; Accepted 25 June 2020

Grant sponsor: International Society for the Advancement of Cytometry (ISAC), Grant number Marylou Ingram Scholars Program; Grant sponsor: Merridew Foundation; Grant sponsor: National Health and Medical Research Council, Grant number: 1088242

Additional Supporting Information may be found in the online version of this article.

*Correspondence to: Nicholas Jonathan Cole King, Charles Perkins Centre, D17, Johns Hopkins Dr, University of Sydney, Camperdown, NSW 2050, Australia
Email: nicholas.king@sydney.edu.au

†These authors contributed equally to this work.

Published online 17 September 2020 in Wiley Online Library (wileyonlinelibrary.com)

DOI: 10.1002/cyto.a.24211



## Abstract

In conventional fluorescence cytometry, each fluorophore present in a panel is measured in a target detector, through the use of wide band-pass optical filters. In contrast, spectral cytometry uses a large number of detectors with narrow band-pass filters to measure a fluorophore's signal across the spectrum, creating a more detailed fluorescent signature for each fluorophore. The spectral approach shows promise in adding flexibility to panel design and improving the measurement of fluorescent signal. However, few comparisons between conventional and spectral systems have been reported to date. We therefore sought to compare a modern conventional cytometry system with a modern spectral system, and to assess the quality of resulting datasets from the point of view of a flow cytometry user. Signal intensity, spread, and resolution were compared between the systems. Subsequently, the different methods of separating fluorophore signals were compared, where compensation mathematically separates multiple overlapping fluorophores and unmixing relies on creating a detailed fluorescent signature across the spectrum to separate the fluorophores. Within the spectral data set, signal spread and resolution were comparable between compensation and unmixing. However, for some highly overlapping fluorophores, unmixing resolved the two fluorescence signals where compensation did not. Finally, data from mid- to large-size panels were acquired and were found to have comparable resolution for many fluorophores on both instruments, but reduced levels of spreading error on our spectral system improved signal resolution for a number of fluorophores, compared with our conventional system. Furthermore, autofluorescence extraction on the spectral system allowed for greater population resolution in highly autofluorescent samples. Overall, the implementation of a spectral cytometry approach resulted in data that are comparable to that generated on conventional systems, with a number of potential advantages afforded by the larger number of detectors, and the integration of the spectral unmixing approach. 

## Key terms

spectral cytometry; unmixing; compensation; high-dimensional; polychromatic; viral encephalitis

## Introduction

### Fluorescence Cytometry and Spreading Error

Flow cytometry is a technique that utilizes the emission of multiple fluorescently labeled antibodies excited by a laser to measure the simultaneous expression of various proteins on single cells. The high sensitivity and high-throughput nature of this technique, in conjunction with the increasing numbers of available fluorophore labels, make it suitable for the characterization of many cell subsets under a wide variety of conditions. In conventional cytometry, individual detectors (often photomultiplier tubes [PMTs]) are used to record the signal from specific target fluorophores following excitation with a laser (Fig. 1A) via selective optical filters

with wide band-pass properties, to maximize the amount of light collected (Fig. 1B). As such, each detector is effectively tailored to a particular fluorophore, restricting the range of fluorophores that can be used on these systems, thus limiting reagent flexibility. Many fluorophores that are used simultaneously may have overlapping emission spectra, leading to spillover of one fluorophore into a nontarget detector (Fig. 1C,D). However, the process of compensation can mathematically correct for the overlap of signal from a target fluorophore into all other nontarget detectors (Fig. 1E) (1, 2). Through the application of linear algebra, the spillover of each fluorophore into all detectors is corrected such that each detector effectively contains information for only a single dye. This is achieved by multiplying the measured signal in each detector by the inverse of a mixing matrix, scaled columns wise to 1 (3). Errors or uncertainty in photon counting complicates the correction of mixed signals resulting from spillover, as they are not described by a Gaussian distribution. Thus, applying a linear correction to the nonlinear counted photons results in an error in the distribution of the spillover fluorophore signal in nontarget detectors. This is referred to as spreading error (SE) (4). It manifests as an increased width of the signal from a spillover fluorophore in a nontarget detector after compensation, and the spread of this signal increases as the fluorescence intensity of the spillover fluorophore increases. Importantly, compensation does not introduce this error, but rather the process of compensation moves the signal distribution to the low end of a logarithmic or bi-exponential/Logicle scale. As a result, this signal distribution appears to expand. SE can complicate separating the negative and positive populations that are being measured in that detector. The construction of high-quality panels requires careful panel design to reduce the intensity of signals that have a large degree of SE, as not all fluorophores will exhibit the same level of SE in all detectors. Recently, advances in instrumentation and dye development have led to the development of panels that can incorporate more than 25 fluorophores simultaneously across five or more excitation lasers (5-7), with reports of 40-color panels beginning to emerge.

## Spectral Cytometry

An alternative approach to measuring multiple overlapping fluorophores on single cells is through the use of spectral cytometry. The use of spectral approaches for flow cytometry was demonstrated as early as 2004 by Robinson et al. (8, 9), resulting in a patent (10) and its subsequent licensing to Sony for a commercial spectral flow cytometer (11). Since then, a number of studies have demonstrated the utility of the spectral approach in various flow cytometry experiments (11-16) including the use of panels with more than 20 colors (16), with 40 colors on a spectral system recently reported (17). This technique aims to measure as much of the whole emission spectrum of a fluorophore as possible, across a large number of detectors with narrow band-pass properties, rather than the peak emission in a single detector with wide band-pass properties. Additionally, differential excitation of fluorophores by multiple lasers further increases the granularity of this spectral signature. This design allows for the measurement of any fluorophore that is sufficiently excited by the lasers in use, avoiding the fluorophore-specific detector design characteristic of conventional systems. The signals measured across multiple detectors (Fig. 1F–I) create a detailed fluorescence "signature" for each fluorophore, allowing each of these unique fluorescent signatures to be "unmixed" from one another. Key to this approach is the use of a large number of detectors on each laser line, more than are utilized in conventional systems (Fig. 1J,K). This process potentially allows fluorophores with similar emission properties, which would normally be measured in the same detector on a conventional system, to be measured simultaneously on a spectral system and separated using conventional compensation approaches, or through unmixing based on their differential spectral signatures (Fig. 1L,M). In addition, using this approach, a signature can be determined for cellular autofluorescence in individual samples, allowing for the unmixing of autofluorescence from affected channels, as well as the measurement of autofluorescence as an additional feature. Taken together, the large number of incorporated detectors, the spectral unmixing approach, and the detailed signatures generated for each fluorophore enables the building of large and flexible fluorescent panels that are capable of incorporating highly overlapping dyes.

In conventional compensation, the correction of signal measured in all nontarget detectors is achieved through the inversion of a mixing matrix. In other fields, such as remote sensing and spectral microscopy, various methods of spectral unmixing are applied (18). The unmixing approach used in the spectral system we tested deploys a least-squares linear unmixing calculation. This approach assumes a linear contribution of reference spectra to a mixed signal, where unmixing is achieved through the application of matrix pseudo-inversion. This approach is very similar to compensation (inversion), where the number of columns and rows are the same, where one fluorophore is assigned per detector, but in spectral unmixing (pseudo-inversion), the number of detectors is larger than the number of fluorophores, potentially making the inversion more accurate. The object of this approach is to deconstruct mixed fluorescent signals into separate components (i.e., each individual fluorescent signal), so that the origin of a photon can be reassigned statistically to the source fluorophore (13). This is not the only method of unmixing available, and some approaches may be more suitable when the individual reference spectra are not known. Various comparisons of these approaches have been made elsewhere (13, 19).

## Objectives of the Study

In this study, we sought to compare the performance of a conventional and a spectral cytometry system, specifically in signal quality, extent of spreading error, and signal resolution from spread for mid- to large-size panels, in a number of immunological contexts. Additionally, we sought to compare the results of compensation and unmixing when applied to

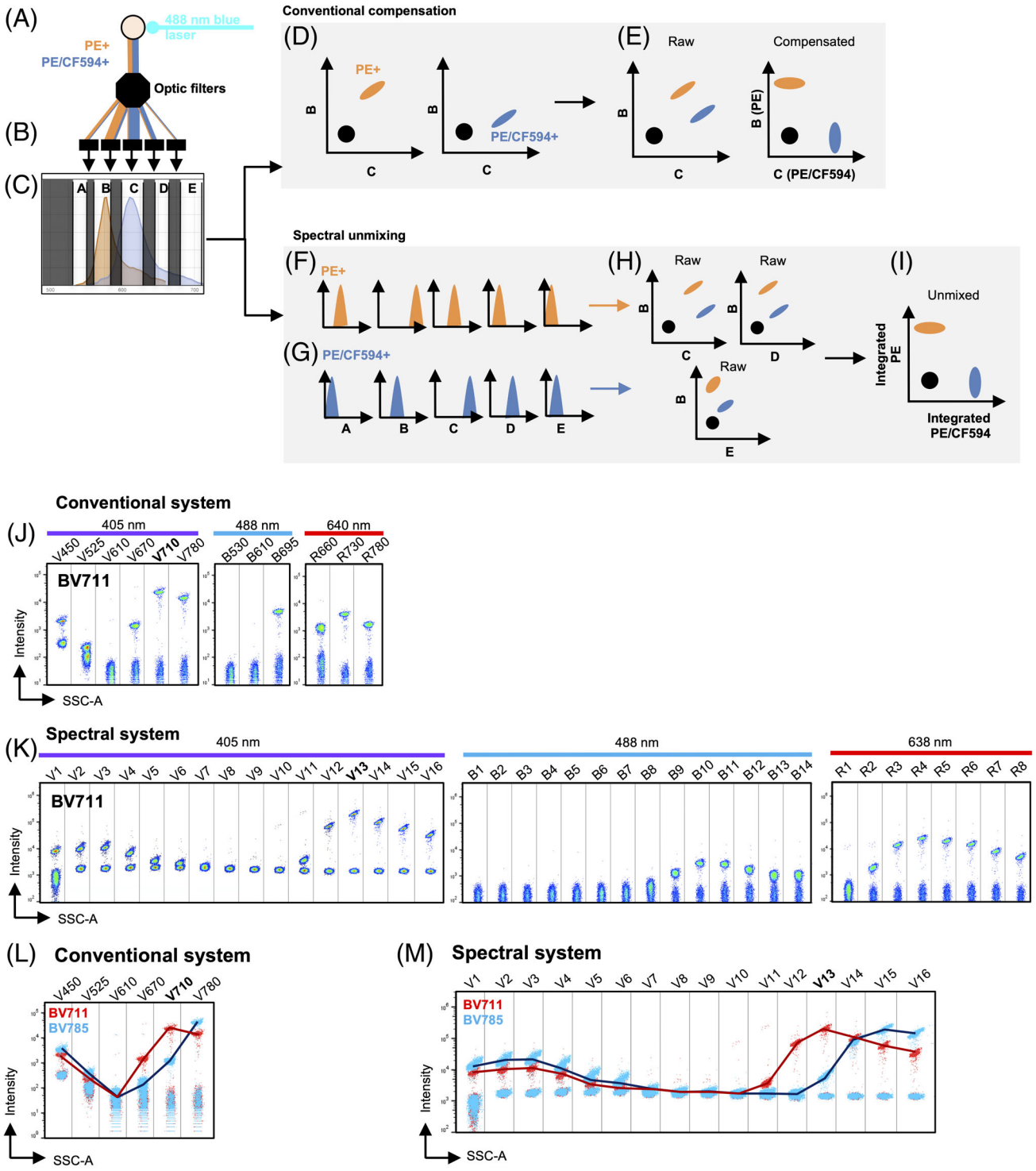


**Figure 1.** Conventional and spectral cytometry. A diagrammatic representation of conventional and spectral cytometry. In this example, (**A**) a blue 488 nm laser excites two fluorophores, PE and PE/CF594. (**B**) The emitted signal from both fluorophores is collected through optical filters, (**C**) and the relative signal arriving at each detector is shown. (**D**) Uncompensated raw data can then (**E**) be compensated to resolve the two signals. In spectral unmixing (**F** and **G**) signals are collected across a number of detectors, and (**H**) integrated signals are then unmixed from each other to generate (**I**) resolved signals. Compensation beads stained with BV711 plotted after acquisition (**J**) the conventional system and (**K**) spectral system. Profile of compensation beads stained with BV711 or BV785 when run on the (**L**) conventional or (**M**) spectral system, showing violet (405 nm) laser detectors only. [Color figure can be viewed at wileyonlinelibrary.com]

the data from the spectral system, to identify potential advantages of the spectral unmixing approach. Importantly, in comparing these systems, there are numerous differences in fluidics and optical design, and these designs do not necessarily reflect all conventional or spectral systems. As such, our aim was to assess these factors from the point of a view of a researcher applying flow cytometry experimentally, weighing the relative strengths and weaknesses in a research context, rather than providing a theoretical or mathematical comparison between the methods.

## Methods

### Mice and Anesthetics

Unless stated otherwise, all experiments were performed using female C57BL/6 mice aged between 8 and 12 weeks. Mice were purchased from the Animal Resources Centre (WA, Australia). All mice were housed (six per cage) in Hepa-filter cages with food and water supplied ad libitum as per the University of Sydney animal housing regulations. Ethical approval for the experimental use of mice was obtained from the Animal Ethics Committee at the University of Sydney, under protocols K20/8-2008/3/4863, K20/6-2012/3/5761, K20/11-2011/3/5660, and 2013/5660-273. Mice undergoing temporary anesthesia for intranasal inoculation, or other procedures, were injected *i.p.* with 250–300 ml of Avertin according to a weigh–volume nomogram. Mice undergoing terminal procedures were given 350–500 µl of anesthetic, followed by vena caval section and left ventricular cardiac perfusion with 30 ml of ice-cold PBS. Avertin anesthetic was prepared by dissolving 1 g of 2,2,2-tribromoethanol (Sigma-Aldrich) in 1 ml 2-methyl-2 butanol (Sigma-Aldrich). Heated tap water (50 ml) was then added to the solution and thoroughly mixed before sterilizing through a 0.2 mm syringe filter in 5 ml aliquots. The Avertin mixture was stored at −20°C in the dark until use.

### Inoculation of Mice with West Nile Virus

Supine, anesthetized mice were inoculated intranasally with 10 µl of West Nile virus (WNV), 5 µl per nostril. Mice were given a total of $6 \times 10^4$ plaque-forming units (PFU), the lethal dose for 100% ($LD_{100}$) of mice by this route of inoculation.

### Cell Isolation and Preparation

Bone marrow was prepared as described in reference (20). Mouse femurs were collected, and the distal and proximal ends removed with a scalpel or surgical scissors. The femur was then flushed with 1–3 ml of cold PBS (from a 5 ml syringe using a 33G needle) to collect BM cells into a 5 ml or 15 ml tube. Cells were then centrifuged at 500*g* for 5 min at 4°C to pellet the cells. Samples were then resuspended in 700 µl to 1 ml of fluorescence-activated cell sorting (FACS) buffer (PBS, 5 mM EDTA, 5% FCS), counted, and the desired cell numbers transferred to a 96-well plate for staining. Samples were kept on ice until antibody labeling later on the same day.

Spleens were removed from the peritoneal cavity and gently mashed through 70 µm cell strainers in 5 ml of cold PBS and centrifuged at 500*g* for 5 min at 4°C. Isolated spleen cells were then resuspended in 1–4 ml of FACS buffer and counted. After counting, cells were then placed in wells of a 96-well plate for cell staining. Samples were kept on ice until antibody labeling later on the same day.

Brain samples were prepared by cardiac perfusion with 30 ml of ice-cold PBS, under deep anesthesia to clear the blood vasculature. Brains were removed from the skull, and mechanically disrupted in cold PBS using a metal sieve. Brain homogenates were topped up to 18 ml of PBS and 2 ml of a 10X solution of deoxyribonuclease I (DNase I) and collagenase added for a final concentration of 1 mg/ml collagenase and 0.1 mg/ml DNase, and incubated at 37°C for 1 h. Alternatively, brains were placed into 9 ml of PBS in C-tubes (Miltenyi Biotech, Bergisch Gladbach, Germany), cut into eight sections, and kept at 4°C for up to 3 h on ice. Tubes then received 1 ml of 10X collagenase/DNase solution and the tissue was disrupted using a custom protocol on the GentleMacs auto-dissociator (Miltenyi Biotech, Bergisch Gladbach, Germany) for 30 min. Samples were then centrifuged (500*g*, 4°C, 10 min) and resuspended in 7 ml of a 30% Percoll solution (26.31% Percoll stock, 10% 1.5 M NaCl, 63.7% Media). This mixture was then slowly overlayed onto 3 ml of 80% Percoll (73.1% Percoll stock, 10% 1.5 M NaCl, 16.9% sterile $H_2O$) using a 10 ml pipette. The layered mixture was centrifuged at 1825*g* for 25 min at 25°C with the brake off. After centrifugation, the top layer of fat was removed and 2 ml of the cellular interface was pipetted into a new 15 ml tube and topped up with 5 ml FACS buffer, before centrifugation (500*g*, 4°C, 5 min) and resuspension in 250 µl of FACS buffer. Samples were kept on ice until flow cytometry antibody labeling later on the same day.

Cell suspensions from digested brain tissues were counted on a hemocytometer and assessed for viability using trypan blue exclusion. Bone marrow and spleen cell suspensions were analyzed on a XP-100 hematological analyzer (Sysmex, Kobe, Hyogo, Japan).

### Cell Staining

Samples were distributed into wells of a 96-well plate, typically $1 \times 10^6$ cells per well, centrifuged at 300–500*g* for 5 min at 4°C and the supernatant discarded. Samples were then resuspended in 50 µl PBS-containing Zombie NIR Live/Dead (1/1,000, BioLegend, San Diego, CA) and purified anti-mouse CD16/32 (1/100, BioLegend), incubated for 20 min at 4°C, and then topped up with PBS before centrifugation. Samples were then resuspended in 50 µl of antibody master mix, and incubated for a further 30 min at 4°C before centrifugation and washed twice. Antibody details are provided in Supporting Information Table S4. Samples were then fixed in 4% paraformaldehyde (PFA) or fixation buffer (BioLegend) for 10 min. After fixation, samples not requiring intracellular staining were washed once, centrifuged at 800*g* for 5 min, and resuspended in FACS buffer and kept at 4°C for up to 3 days until flow cytometric acquisition. Alternatively, samples were

processed for intracellular staining. For instrument comparisons and compensation/unmixing, UltraComp beads (Thermo Fisher Scientific, Waltham, MA), or quantum simply cellular beads (QSCB) were labeled with selected fluorophore-conjugated antibodies in the same conditions as cellular samples, including staining time, temperature, and fixation.

### Intracellular Staining

For intracellular staining of transcription factors, cells were washed in FACS buffer following fixation and permeabilized in 50–100 µl of FoxP3 fixation/permeabilization buffer (eBioscience, San Diego, CA) for 20 min at RT. After washing, samples were resuspended in 50 µl FoxP3 permeabilization buffer containing specific concentrations of intracellular antibodies. Samples were then incubated for 45 min at RT, washed in permeabilization buffer, and then washed in FACS buffer.

### Instrumentation

For flow cytometry, samples were analyzed on a 4-laser Becton-Dickinson (BD, Franklin Lakes, NJ) Fortessa X-20 (conventional system), a 5-laser BD LSR-II (conventional system), or a 3-laser Cytek Aurora (spectral system). Configurations are provided in the Supporting Information Tables S1–S3. All instruments were subject to daily QC procedures before the samples were acquired. The data in Figures 1 and 2 were generated on the BD Fortessa X-20 (conventional system) or Cytek Aurora (spectral system). For these comparisons, only the violet, blue, and red lasers were used with fluorophores that were compatible with both systems. The data in Figures 4–7 were generated on the BD Fortessa X-20, BD LSR-II, or Cytek Aurora, as specified in the figure legends. The data in Figure 3 were generated on the spectral system only.

### Data Analysis

For "peak channel" data, the channel with the peak signal for each fluorophore in each case was selected as the "target" detector, and compensation was performed in FlowJo v10.6.1 (BD). Of note, in the fluorochromes included in the study, each fluorophore peaked in a separate channel on the Aurora, as it has many more detectors than a conventional system; therefore, we did not need an approach to handle fluorochromes peaking in the same detector. Compensation for "virtual channel" data, and spectral unmixing, was performed in SpectroFlo software (Cytek Biosciences, Fremont, CA). Graphs were generated in PRISM (GraphPad, San Diego CA).

## Results

### Comparing Staining on the Conventional and Spectral System

Initially, we sought to compare the performance of a conventional and spectral system in terms of signal quality per fluorophore. To do this, we prepared compensation beads labeled with a variety of common fluorophores and recorded them on a conventional system (BD Fortessa X-20, using 12 detectors across 3 lasers) or a spectral system (Cytek Biosciences Aurora, Fremont, CA, using 38 detectors across 3 lasers). The spectral detectors allowed for measurement of fluorescence signal with a detection range up to at least $1 \times 10^6$, greater than the detection range up to $2.62 \times 10^5$ on the conventional system. For the fluorophore-bound beads analyzed in this experiment, the signal CVs were similar, suggesting similar signal quality (Supporting Information Fig. S1).

### Comparing Signal Spread and Resolution on the Conventional and Spectral Systems

To compare data generated on each system in terms of signal spread and resolution, we examined the signal from pairs of fluorophore-labeled compensation beads, plotting the signal from fluorophores in neighboring detectors excited by the same laser (Fig. 2A–D) or from fluorophore pairs that exhibit similar emission properties excited by different lasers (Fig. 2E–H). For each fluorophore pair, the spread of the offending positive signal (red) is shown against the positive signal in the receiving detector (blue). We made these comparisons for compensated data from the conventional (Fig. 2A,E) and spectral systems when using data recorded in the peak channel (Fig. 2B,F). We also made these comparisons for compensated fluorophores on the spectral system after aggregating each signal into virtual filters (Fig. 2C,G), to match the filter configuration of the conventional system as closely as possible. Finally, we made these comparisons for data acquired on the spectral system after unmixing (Fig. 2D, H). To quantify these relationships, we used two metrics: a spreading ratio and a resolution ratio (Fig. 2I). The spreading ratio was calculated as the 99th percentile of the offending fluorophore in the receiving detector, divided by the 99th percentile of unstained beads in the same channel. The resolution ratio was calculated as the median of the receiving fluorophore in the receiving detector, divided by the 99th percentile of the offending fluorophore in the same detector. A demonstration of how these metrics reflect patterns on the plots is provided in the Supporting Information Figure S2.

When we compared compensated data from the conventional (Fig. 2A,E) and spectral system (peak detectors, Fig. 2B, F), higher levels of spread of the positive signal into neighboring or cross laser detectors (red arrows) were evident on the conventional system when compared to the spectral system. When we quantified this (Fig. 2J), we found that the degree of spread across all measured fluorophores was higher overall for the conventional system compared with the spectral system. However, because the signal intensity in the receiving detector (blue) was higher for the conventional system compared with the spectral system, the increased spread did not have a large impact on the resolution of signal from spread. When we quantified the resolution of the signal of the fluorophore in the receiving detector (blue) against the spreading signal (red), we found some cases where, despite decreased spread on the spectral system when compared to the conventional system, no change was found in the resolution of blue from red signal (e.g., PE-CF594 vs PerCP/Cy5.5). However, in

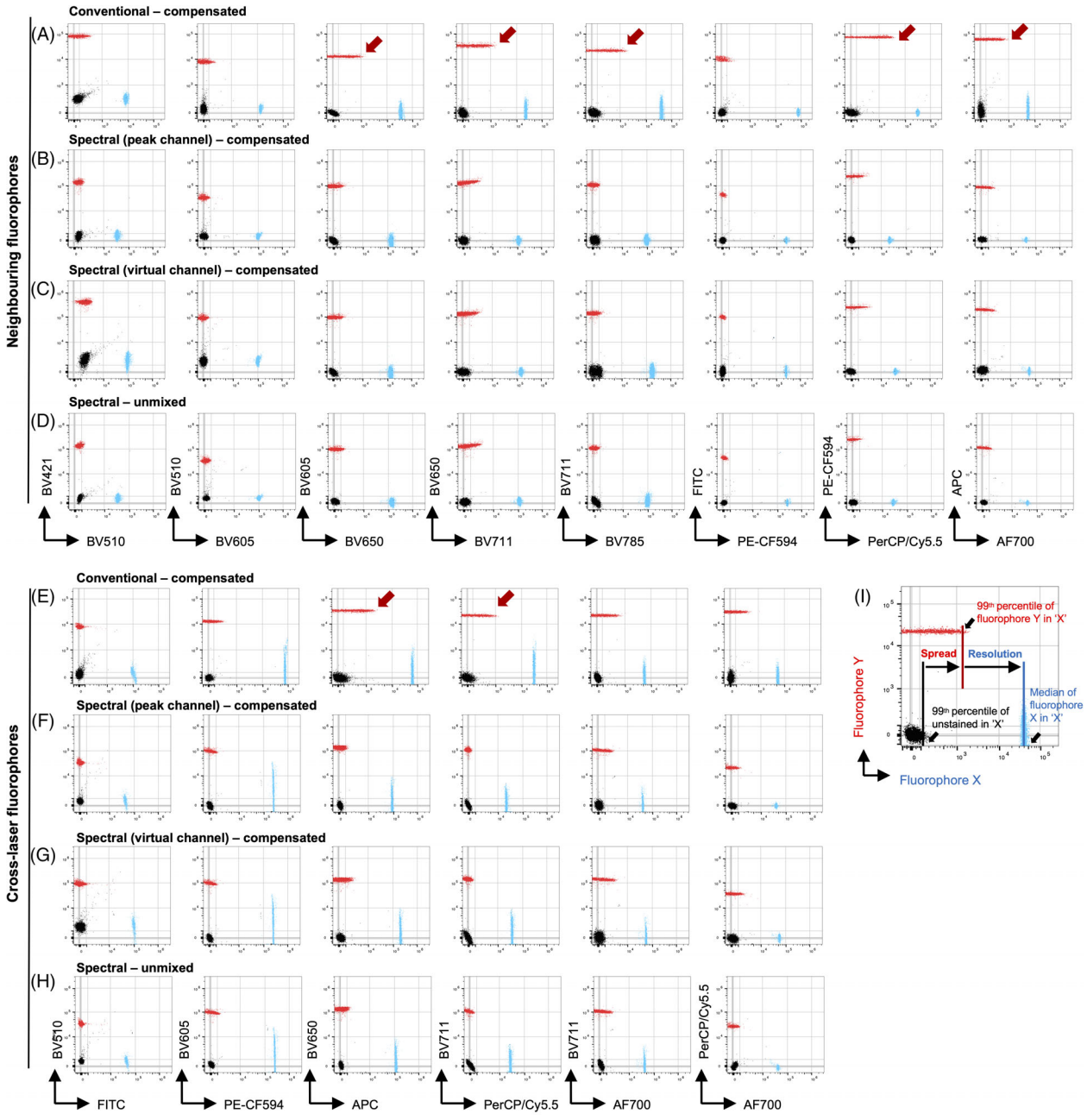


(J) **Signal spread**

| | | BV421/BV510 | BV510/BV605 | BV605/BV650 | BV650/BV711 | BV711/BV785 | FITC/PECF594 | PECF594/PerCPCy55 | APC/AF700 | BV510/FITC | BV605/PECF594 | BV650/APC | BV711/PerCPCy55 | BV711/AF700 | PerCPCy55/AF700 |
|---|---|---|---|---|---|---|---|---|---|---|---|---|---|---|---|
| Conventional | Compensated | 0.95 | 2.92 | 9.54 | 12.10 | 8.58 | 2.35 | 17.67 | 8.49 | 0.76 | 3.01 | 6.83 | 5.96 | 6.95 | 4.56 |
| Spectral (peak channels) | Compensated | 0.75 | 1.16 | 2.15 | 3.18 | 0.84 | 1.12 | 4.89 | 2.33 | 1.06 | 1.82 | 1.99 | 0.93 | 3.02 | 1.29 |
| Spectral (virtual channels) | Compensated | 0.62 | 1.17 | 2.20 | 2.31 | 0.80 | 1.07 | 5.09 | 1.97 | 0.97 | 1.79 | 2.42 | 1.11 | 2.97 | 1.57 |
| Spectral | Unmixed | 0.63 | 1.07 | 1.91 | 2.98 | 0.76 | 1.20 | 1.52 | 1.38 | 0.99 | 2.10 | 2.83 | 0.78 | 2.84 | 1.20 |

(K) **Signal resolution**

| | | | | | | | | | | | | | | | |
|---|---|---|---|---|---|---|---|---|---|---|---|---|---|---|---|
| Conventional | Compensated | 25.33 | 79.20 | 38.71 | 20.96 | 29.15 | 372.57 | 11.58 | 8.58 | 128.55 | 290.75 | 35.82 | 34.33 | 10.48 | 15.99 |
| Spectral (peak channels) | Compensated | 26.36 | 155.60 | 101.26 | 42.07 | 113.77 | 428.31 | 12.01 | 23.43 | 88.65 | 263.44 | 83.11 | 62.94 | 18.07 | 42.49 |
| Spectral (virtual channels) | Compensated | 29.53 | 166.41 | 97.03 | 55.52 | 135.11 | 441.84 | 13.82 | 27.22 | 103.30 | 264.27 | 92.18 | 63.61 | 18.02 | 34.14 |
| Spectral | Unmixed | 26.99 | 134.71 | 100.52 | 38.73 | 129.20 | 400.39 | 27.42 | 45.65 | 107.77 | 227.91 | 96.57 | 53.30 | 22.13 | 52.40 |

**Figure 2.** Legend on next page.

many cases, this reduction in spread was paired with an increase in the resolution of blue from red signal (e.g., BV711 vs BV785).

One possible explanation for these differences was that the "peak" detectors used on the spectral system were capturing different light spectra, due to their smaller band pass filter range (e.g., the FITC detector on the conventional system captures 500–550 nm, whereas the "peak" FITC detector on the Aurora captures 498–518 nm). To test this, we compensated data from the spectral system using virtual filters, where data were integrated from multiple detectors to match (as closely as possible) the band-pass filter range of the corresponding detector on the conventional system (Supporting Information Fig. S3). When we compared compensated data from these virtual channels against the compensated peak channel data, or data from the conventional system, we found little change in either spread or resolution values (Fig. 2C,G,J,K).

### Spectral Unmixing and Compensation

On many conventional systems, fluorophores with very similar peak emission properties are often captured using the same wide band-pass filter, meaning that only one of those fluorophores may be used in a given panel (e.g., APC and

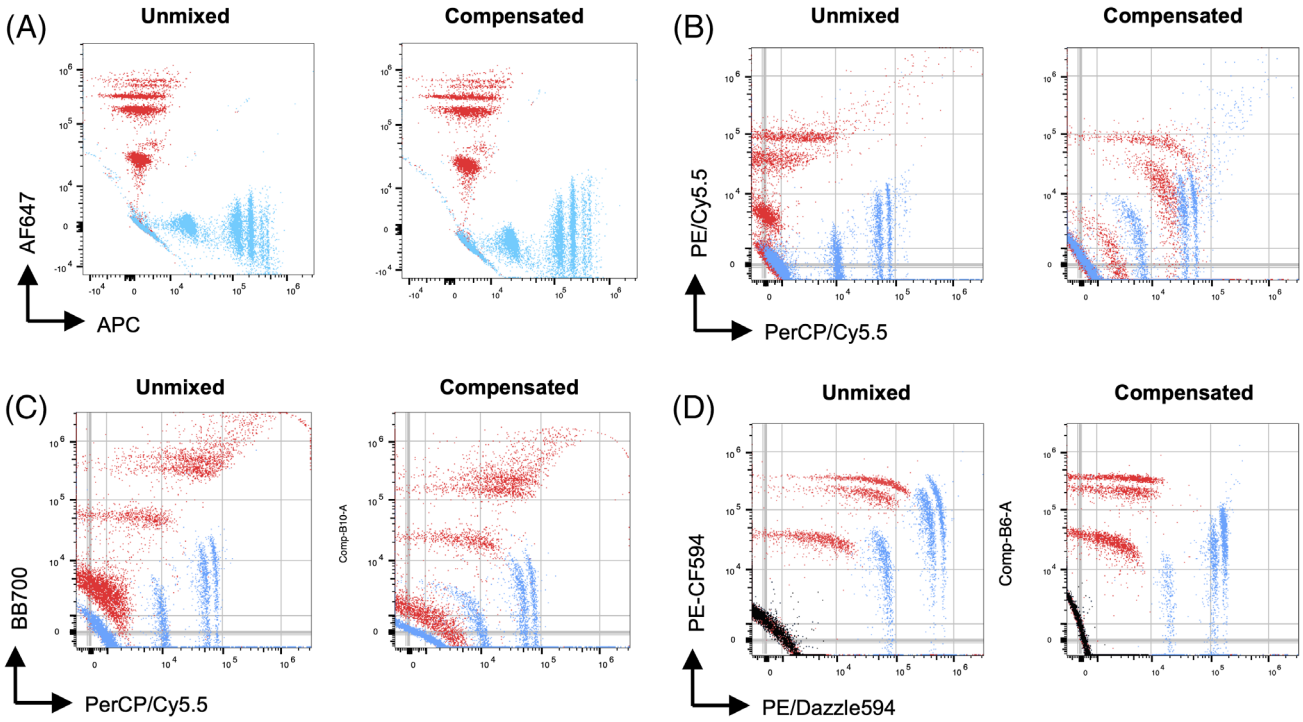


**Figure 3.** Comparing compensation and spectral unmixing on the spectral system. QSCBs labeled with various fluorophores, subject to spectral unmixing (SpectoFlo) or compensation (FlowJo). Beads were labeled with (**A**) AF647 and APC, (**B**) PE/Cy5.5 and PerCP/Cy5.5, (**C**) BB700 and PerCP/Cy5.5, or (**D**) PE-CF594 and PE/Dazzle594. In some cases, these fluorophores had the same "peak" detector. As such, for compensation, one fluorophore had to be assigned to a nonoptimal channel in order to perform compensation. [Color figure can be viewed at wileyonlinelibrary.com]

**Figure 2.** Signal comparisons between the conventional and spectral systems. Compensation beads labeled with various fluorophores plotted against each other. For the data in this figure, the fluorophores tested were excited using the same lasers on both the conventional (BD Fortessa X-20) and spectral (Cytek Aurora) systems. Of note, PE-CF594 was detected using the blue laser on both the spectral system and the conventional system, having a Yellow/Green 561 nm option available on the conventional system. The spread of one fluorophore signal (red) is plotted (and measured) against a (**A–D**) neighboring fluorophore (blue) on the same laser, or (**E–H**) another fluorophore (blue) with similar emission properties that is primarily excited by a different laser (cross-laser fluorophore). The degree of spread (red) and the resolution of signal (blue) from spread (red) are quantified by two ratios. Spread is calculated as the 99th percentile of the spreading fluorophore (red) in the receiving detector, divided by the 99th percentile of unstained beads in the same channel. Resolution is calculated as the median of the receiving fluorophore (blue) in the receiving detector, divided by the 99th percentile of the spreading signal (red). Spreading results for fluorophore pairs are provided in **J** (where increasing values are indicated by the intensity of color grading from white to red), and resolution results are provided in **K** (where increasing values are indicated by the intensity of color grading from white to blue). Comparisons were made for: (**A, E**) data from the conventional system when compensated, (**B, F**) data from the spectral system (using "peak" signal detectors only) when compensated, (**C, G**) data from the spectral system (using virtual channels derived from integrated signal) when compensated, and (**D, H**) data from the spectral system when unmixed. Details on the integration of signal into virtual channels are provided in the Supporting Information Figure S3. Red arrows indicate occasions where greater signal spread was observed for data from the conventional system, compared to data from the spectral system. [Color figure can be viewed at wileyonlinelibrary.com]

AF647). A key claim of the spectral approach is that dyes with similar emission properties can be analyzed simultaneously in sufficient detail on a spectral system to create a signature through the use of a larger number of detectors, allowing these signals to be spectrally "unmixed" from each other. However, as these comparisons are often made in the context of unmixing performed on a spectral system and compensation performed on a conventional system, the relative contributions of the system itself (detection methods, optical configurations, detection sensitivity, electronic noise, etc) and the signal correction process (compensation, unmixing) are often intertwined. While a thorough mathematical comparison of the signal correction approaches was outside the scope of this study, it has been studied elsewhere (19). However, in our study, we sought to determine if the *provided* unmixing approach gave any specific advantages over compensation in the context of a spectral analyzer (Fig. 2D,H). Overall, we found that unmixed and compensated data were largely comparable (Fig. 2J,K), where spread and resolution for unmixed data for the fluorophores examined were similar to compensated peak channel or virtual filter data from the spectral system. However, we did find some cases where unmixing led to reduced spread and increased resolution, such as in PE-CF594 vs PerCP/Cy5.5.

### Separation of Highly Overlapping Fluorophores Using Spectral Unmixing and Compensation

Despite this, we reasoned that spectral unmixing may result in improvements in signal resolution for fluorophores that had very similar peak emission properties, due to the more detailed spectral signature that can be measured on the Aurora. To test this, we labeled QSCB multilevel capture beads with a variety of fluorophores, including a number of highly overlapping fluorophores that would not normally be combined on a conventional system as they would be measured in the same detector. These samples were recorded on the spectral system and subject to compensation (using FlowJo v10.6.1) or spectral unmixing. For some dyes that are typically measured in the same detector but are spectrally distinct, such as AF647 and APC, we were able to successfully separate these signals using either compensation (peak channel) or spectral unmixing (Fig. 3A), although we did find better resolution in the unmixed data. However, for other dyes with similar emission properties, such as PE/Cy5.5 and PerCP/Cy5.5 (Fig. 3B) or BB700 and PerCP/Cy5.5 (Fig. 3C), we found that we these two signals were substantially better resolved from each other when subject to spectral unmixing, compared with (peak channel) compensation. Nevertheless, we also found some instances where compensation resulted in better signal resolution than unmixing (Fig. 3D).

### Comparing Leukocyte Panels on Conventional vs Spectral System

Importantly, we sought to explore the application of spectral cytometry for mid to large size panels from the perspective of a cytometry user and how this technology may apply to their research. Thus, we compared the resolution of cellular populations on the two systems. To do this we labeled bone marrow (BM) cells from mock- or West Nile virus (WNV)-infected mice with a panel of antibodies against typical leukocyte markers. After staining and fixation, each sample was split into two and run in parallel on a conventional system (using four lasers, compensated) and a spectral system (using three lasers, unmixed). Although different lasers were used on each system, we sought to determine if the staining patterns and frequencies of each population were comparable between systems. We adjusted the plots so that a comparable dynamic range was displayed for each system, and the frequencies of each population were calculated.

We examined BM cells from mock-infected animals and compared data generated on the spectral and conventional systems for singlets, cells, live cells, leukocytes (Fig. 4A–D), T cells, NK cells, NKT cells, $CD4^+$ T cells, $CD8\alpha^+$ T cells, plasmacytoid dendritic cells (PDCs), B cells, conventional dendritic cells (cDCs) (Fig. 4E–H), neutrophils, eosinophils, resident macrophages, $Ly6C^{hi}$ monocytes, and $Ly6C^{lo}$ monocytes (Fig. 4I–L). Overall, both the staining patterns and quantification of each of these populations were largely comparable between the two systems (Supporting Information Fig. S4A).

In addition to examining normal BM, we also sought to compare the resolution of each system on a more complex assay that included intranuclear staining. To this end, we designed a seven-color panel identifying regulatory T cells in the murine spleen. As with the BM samples, each sample was split into two and the same panel run in parallel on a conventional system (using four lasers, compensated) and a spectral system (using three lasers, unmixed). In each data set, we examined singlets, cells, live cells (Fig. 5A), T cells (Fig. 5B), $CD4^+$, and $CD8\alpha^+$ T cells (Fig. 5C). Within the $CD4^+$ T-cell population, $FoxP3^+CD25^+$ regulatory T cells were identified (Fig. 5D, left panel), using the fluorescence minus one (FMO) samples to determine the cut-off values for populations (Fig. 5D, center and right panel). Interestingly, we found two prominent differences in this case. The resolution of AF700 CD4 from the spread of BV711 CD8α was improved on the spectral system, as was the resolution of APC FoxP3 from background.

### Comparing Brain Samples Panels on Conventional vs Spectral System

We also sought to compare more highly autofluorescent samples. To do this we infected mice with WNV and isolated brain tissue for flow cytometry 7 days post infection. As with the BM, each sample was split into two and the same panel run in parallel on a conventional system (using four lasers, compensated) and a spectral system (using three lasers, unmixed). In each data set, we examined singlets, cells, live cells, leukocytes, (Fig. 6A–D), neutrophils, eosinophils, NK cells, NKT cells, $CD4^+$ T cells, $CD8\alpha^+$ T cells (Fig. 6E–H), PDCs, B cells, cDC, microglia, $Ly6C^{hi}$ and $Ly6C^{lo}$ infiltrating monocytes (Fig. 6I–L). Overall, we found staining patterns and quantification to be similar between the systems (Supporting Information Fig. S4B). However, population

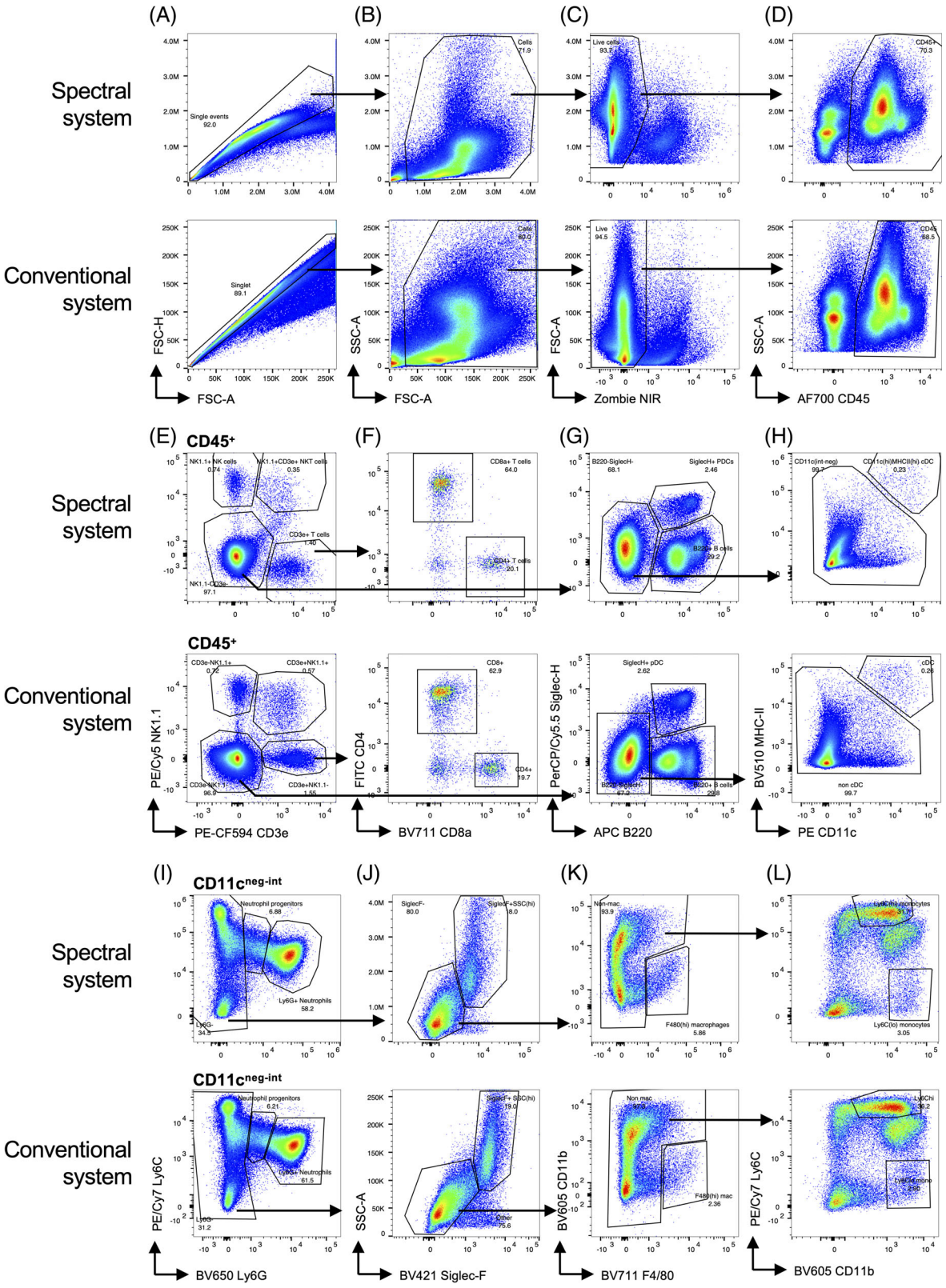


**Figure 4.** Legend on next page.

resolution in fluorophores being measured in areas of high autofluorescence clearly differed between the samples acquired on the conventional versus spectral system, as described below.

### Autofluorescence Extraction

An additional advantage of a spectral approach is in the separate measurement of autofluorescence. By measuring the whole fluorescent spectrum of unstained cells, and treating this fluorescent signature as another fluorophore, the autofluorescent signal can be used as another marker for cellular identification of, for example, neutrophils or senescent cells (21, 22). Alternatively, the autofluorescent signal can be reduced by unmixing the signal from other signals (referred to as extraction), potentially improving resolution in some channels, particularly for cells from highly autofluorescent organs like liver, brain and skin. To determine the extent to which autofluorescence extraction improves resolution, we sought to compare highly autofluorescent samples on both the conventional and spectral systems, including using autofluorescence extraction in the unmixing process for data generated on the Aurora.

The autofluorescence signal in the CNS samples was highest in the 500–650 nm region, in particular in the detectors for the violet laser, but there is also substantial signal measured from the blue laser. By comparing unmixed data, with or without including autofluorescence measured on unstained cells as a parameter, we determined whether autofluorescence extraction improved the resolution of signal in brain samples. In comparing the fluorescence spectrum of the unstained brain to the spectra of the various fluorophores, it is clear that the interference is largest with FITC and BV510 (Fig. 7A). This is also obvious in the labeled samples, with discrimination of individual populations being almost impossible due to autofluorescence interference (Fig. 7B). When autofluorescence extraction was applied, the populations became clear (Fig. 7C), increasing the resolution ratio of the measured populations (defined as the median of the positive population, divided by the 99th percentile of the negative population). BV605 is still in this region where autofluorescence impacts the signal (Fig. 7D), although the interference is much less than with FITC and BV510 (Fig. 7E, F). When examining the spectrum around the 780 nm region (Fig. 7G), autofluorescence makes little difference to the signal in these samples, and thus subtraction of autofluorescence does not substantially improve resolution (Fig. 7H,I).

## Discussion

Spectral cytometry provides a number of potential advantages over conventional cytometry through the detailed measurement of the fluorescent spectrum for each fluorophore. In this study, we sought to compare the performance of a spectral cytometry system with conventional system. Overall, the systems were comparable for the applications we tested when performing compensation or spectral unmixing on either system. However, a number of differences between the two approaches were apparent.

### Signal Comparability of the Systems

Overall, the resolution of signal from background on the systems was comparable. In comparing signal resolution, we looked at two main factors: signal from background (e.g., the separation between the negative and positive population) and signal spread. The former showed greater resolution of signal from background for the fluorophores on the conventional system, while for the latter we found a decrease in signal spread from measurements made on the spectral system, compared to the conventional system, and in many cases, this was accompanied by an increase in resolution of signal from spread. It is likely that the use of avalanche photodiode (APD) detectors on the spectral system contributes to the improved resolution of some of these signals, compared to the photomultiplier tube (PMT) detectors used on the conventional system, as APD have been shown to perform better in spectral regions over 650 nm due to increased sensitivity in these parts of the spectrum (23). Importantly, although the resolution of individual signals from background was lower on the spectral system compared to the conventional system in this comparison, the improved signal resolution from signal spread in most cases indicates better performance in a mixed panel context. Of note, in our comparison, we used two conventional cytometers with specific configurations, and as such, these comparisons may differ for other conventional cytometers.

### Spectral Unmixing vs Compensation

Importantly, spectral unmixing did not eliminate spreading error, despite increased signal resolution from spreading error in many cases. However, fluorophores that are very similar

**Figure 4.** Instrument comparison using a general leukocyte panel on bone marrow cells. Bone marrow cells were stained with a general immune panel and run on the three-laser spectral system or a four-laser conventional system. On the spectral system, PE and PE tandem fluorophores were excited with the blue laser, and on the conventional system, they were excited using the Yellow/Green 561 nm laser. Samples were gated for (**A**) singlets, (**B**) cells, (**C**) live cells, and (**D**) $CD45^+$ leukocytes. (**E**) T cells ($CD3\varepsilon^+NK1.1^-$), NKT cells ($CD3\varepsilon^+NK1.1^+$), and NK cells ($CD3\varepsilon^-NK1.1^+$) were gated, and (**F**) T cells were further subdivided into $CD4^+$ and $CD8\alpha^+$ subsets. (**G**) $CD3\varepsilon^-NK1.1^-$ cells were gated for B cells ($B220^+$Siglec-$H^-$) and PDCs ($B220^+$Siglec-$H^+$), and (**H**) $B220^-$Siglec-$H^-$ cells were then gated for $CD11c^{hi}$MHC-$II^{hi}$ cDCs. (**I**) $CD11c^{neg\text{-}int}$MHC-$II^{neg\text{-}int}$ cells were then gated for mature ($Ly6G^{hi}$) and immature ($Ly6G^{int}$) neutrophils, and (**J**) $Ly6G^-$ cells were then gated for Siglec-$F^+$ eosinophils. (**K**) Siglec-$F^-$ cells were then gated for $F4/80^+$ macrophages and (**L**) $Ly6C^{hi}CD11b^+$ monocytes. The plot axes were adjusted so that dynamic range could be directly compared between each system. [Color figure can be viewed at wileyonlinelibrary.com]

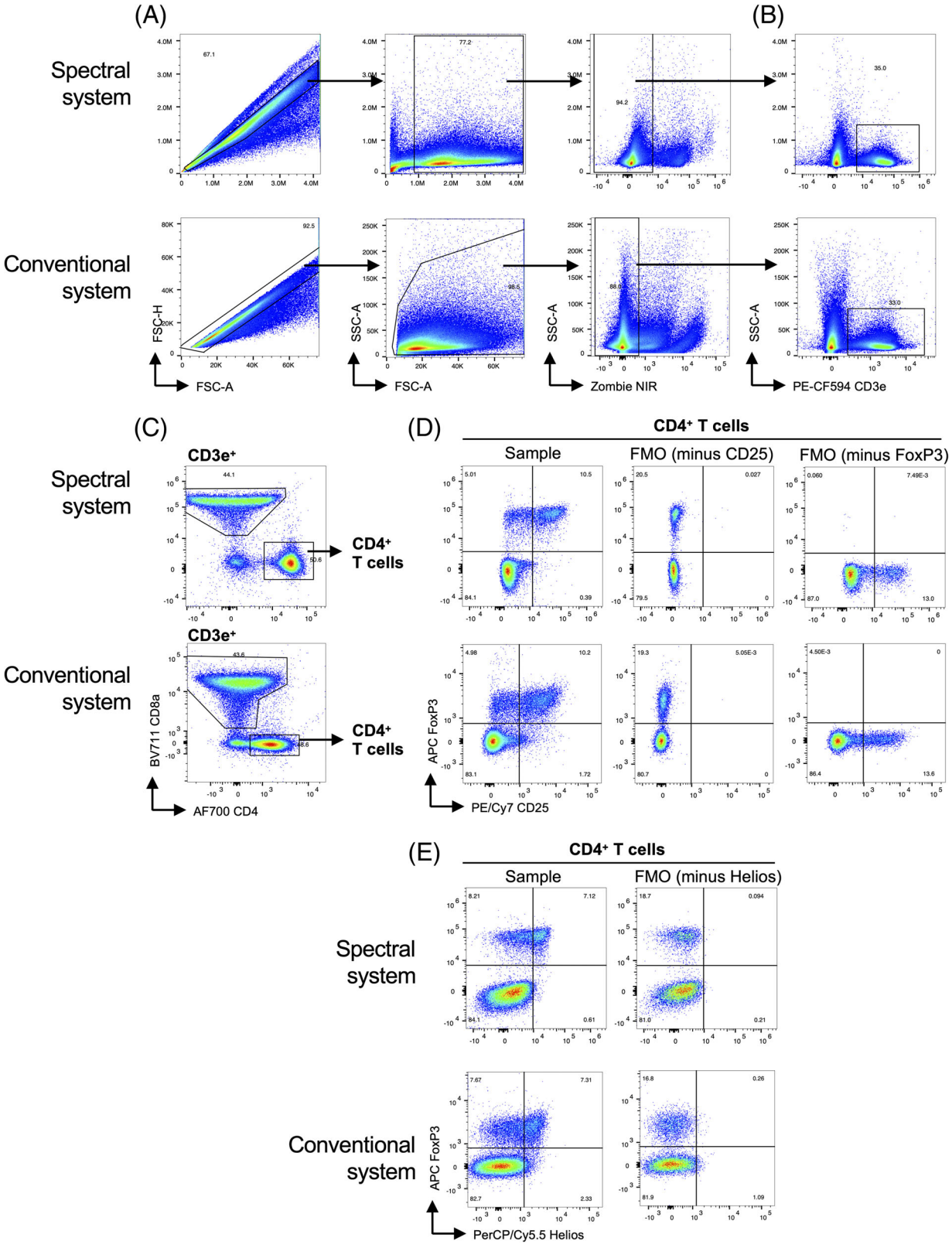


**Figure 5.** Instrument comparison using a T-cell panel on spleen cells. Samples acquired on a three-laser spectral system or five-laser conventional system. On the spectral system, PE and PE tandem fluorophores were excited with the blue laser, and on the conventional system they were excited using the Yellow/Green 561 nm laser. Samples were gated for (**A**) singlets, cells, live cells. (**B**) Samples were then gated for CD3ε$^+$ cells, which were then further subdivided into (**C**) CD4$^+$ and CD8α$^+$ subsets. T-cell subsets where then gated for various combinations of (**D**, **E**) FoxP3, CD25, and Helios, using fluorescence minus one (FMO) controls to guide the placement of gates. The plot axes were adjusted so that dynamic range could be directly compared between each system. [Color figure can be viewed at wileyonlinelibrary.com]

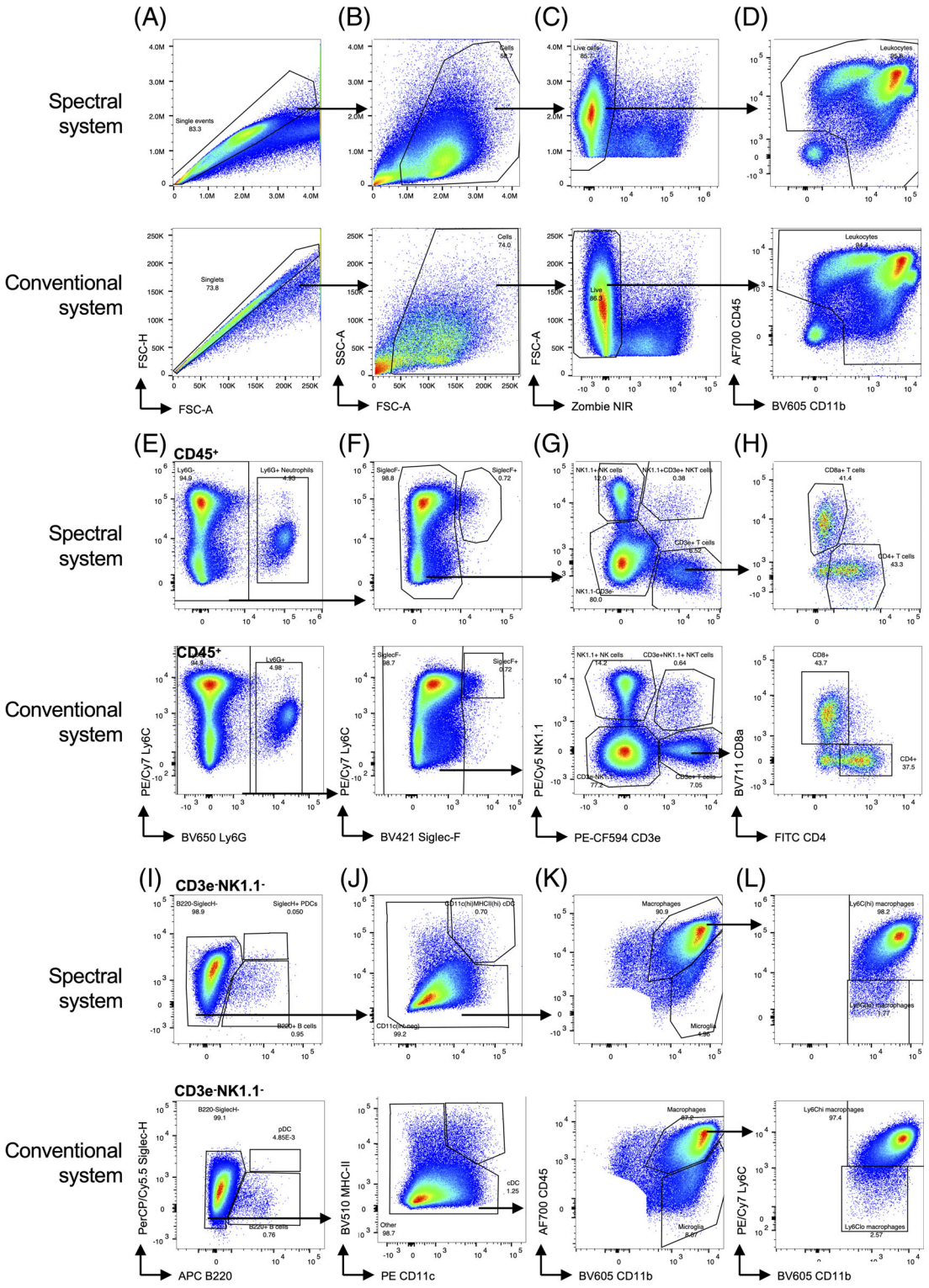


**Figure 6.** Instrument comparison using a general leukocyte panel on cells isolated from infected murine brains. WNV-infected murine brain samples were run on the three-laser spectral system or four-laser conventional system. On the spectral system, PE and PE tandem fluorophores were excited with the blue laser, and on the conventional system they were excited using the Yellow/Green 561 nm laser. Samples were gated for (**A**) singlets, (**B**) cells, (**C**) live cells, and (**D**) $CD45^+$ leukocytes. (**E**) $Ly6G^+$ neutrophils and (**F**) $Siglec\text{-}F^+$ eosinophils were gated, before gating (**G**) T cells ($CD3\varepsilon^+NK1.1^-$), NKT cells ($CD3\varepsilon^+NK1.1^+$), and NK cells ($CD3\varepsilon^-NK1.1^+$). (**H**) T cells were further subdivided into $CD4^+$ and $CD8\alpha^+$ subsets. (**I**) $CD3\varepsilon^-NK1.1^-$ cells were gated for B cells ($B220^+Siglec\text{-}H^-$) and PDCs ($B220^+Siglec\text{-}H^+$), and (H) $B220^-Siglec\text{-}H^-$ cells were then gated for $CD11c^{hi}MHC\text{-}II^{hi}$ cDCs. (**K**) Cells were then gated for $CD45^+CD11b^+$ infiltrating myeloid cells, and $CD45^{lo}CD11b^+$ microglia. (**L**) $CD45^+CD11b^+$ cells were then gated for $Ly6C^{hi}CD11b^+$ infiltrating monocyte-derived macrophages. The plot axes were adjusted so that dynamic range could be directly compared between each system. [Color figure can be viewed at wileyonlinelibrary.com]

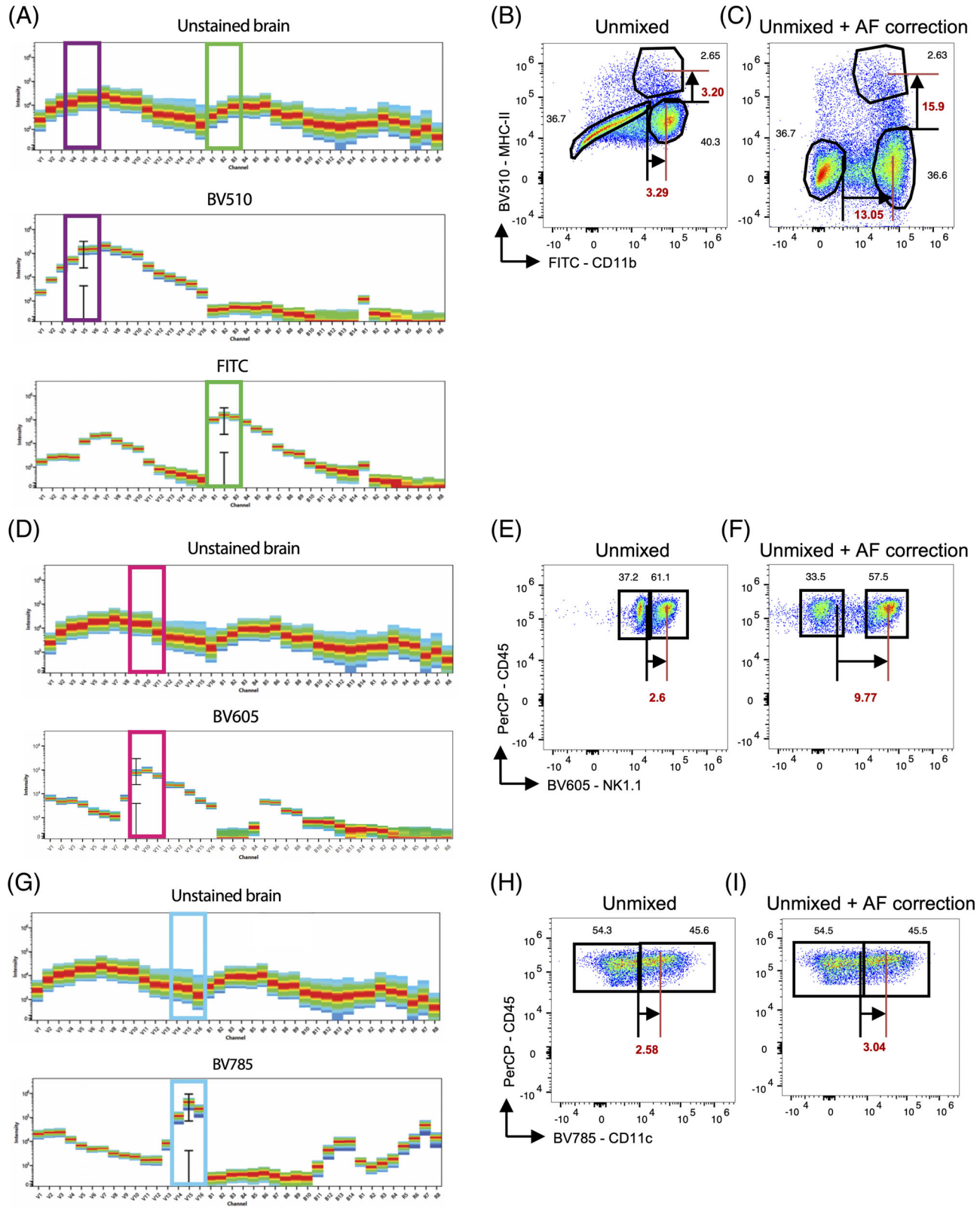


**Figure 7.** Legend on next page.

may gain an additional resolution from the measurement of the complete spectrum of each, enabling more accurate discrimination between them than can be achieved using compensation. This was observed for a number of highly overlapping fluorophores that we tested. However, in one comparison, (PE-CF594 vs PE/Dazzle594) compensation appeared to result in improved resolution over unmixing. It is possible that optimizing the use of specific channels on the spectral system could maximize the level of signal of target fluorophore relative to the spillover fluorophore being detected. In this case, compensated data might be able to separate the signals in a manner similar to unmixing. However, attempting to optimize this is time consuming, and in many cases, applying the unmixing approach appears to result in satisfactory results compared with compensation.

### Autofluorescence Extraction during Spectral Unmixing Increases Population Resolution in Autofluorescence Wavelength Ranges

A key advantage in performing spectral unmixing is the measurement and extraction of cellular autofluorescence in labeled cells. In regions of the spectrum that exhibit low cellular autofluorescence, or in cells that exhibit low autofluorescence, this is of little advantage. However, in autofluorescent cells, in spectral regions where high levels of cellular autofluorescence are observed, such as around the 500–600 nm region, autofluorescence extraction markedly improved the resolution of populations. This is a critical advantage applicable to a wide range of biological contexts, especially where autofluorescence impedes the use of a large number of fluorophores on certain cell types or tissues, as well as where the measurement of autofluorescence as an additional parameter may yield interesting biological insights.

### The Spectral Approach Allows for Far Greater Flexibility in Fluorophore Choice and Panel Design

A key component of panel design in conventional cytometry, is the choice of fluorophores that are able to be detected on a given system, considering the excitation lasers and optical filters available. For example, in our conventional system, the red laser has three associated detectors, with filters designed to capture APC (or AF647), AF700, and APC/Cy7 (or APC/H7), respectively. An outcome of using a larger number of detectors in the spectral system is greater flexibility afforded in the approach to panel design. This was most evident when fluorophores were used together that would normally occupy the same detector on a conventional system (e.g., APC, AF647). However, this is also relevant for fluorophores that are less overlapping, but when used in conventional cytometers, the choice of one or the other has to be made, for example, PerCP and PerCP/Cy5.5. As such, approaches to panel design need not begin with a review of which fluorophores are compatible with the instrument (based on the available filters), but rather a consideration of which possible combinations of fluorophores can be successfully resolved from one another. This allows selection from a wider range of fluorophores, rather than a limited list of instrument-compatible fluorophores.

### The Role of Spectral Cytometry among Conventional High-Dimensional Fluorescence and Mass Cytometry

In the field of single-cell science, the techniques of (conventional) flow cytometry, mass cytometry, image cytometry, and genomic cytometry (single-cell RNA sequencing and associated oligonucleotide reporters for antibody labeling (24)), have all developed their own strengths and weaknesses. Flow cytometry provides a high-throughput and cost-effective method of measuring few parameters (currently up to approx. 27 fluorophores published, with up to 40 fluorophores reported) on many cells with high-throughput (approx. 10,000 events/s). Mass cytometry, on the other hand, acquires cells at a much lower rate (approx. 300–400 events/s), but with more markers per cell (over 50 metals), with significantly reduced overlap between reporters. Single-cell sequencing measures cells at a very low throughput and high cost, but it is capable of measuring hundreds to thousands of genes per cell (RNA, transcriptome), and more recently has incorporated oligonucleotide-based reporters for antibody labeling of cells (proteome/epitome) (24), as well as epigenomic and other single cell measurements (25, 26). Ignoring cost, these technologies represent a spectrum between greater numbers of cells with fewer features per cell, and fewer cells with more features per cell per unit time. Spectral cytometry potentially improves on conventional flow cytometry by enabling the use of previously impracticable fluorophore series, thereby also providing increased flexibility of panel design, as well as incorporating autofluorescence measurement and extraction.

In contrast to the use of fluorescent molecules in flow cytometry, mass cytometry uses heavy metal tags and time-of-flight mass spectrometry readouts to measure antibody binding to cells. This method allows a much larger number of simultaneous markers than conventional flow cytometry. However, while mass cytometry is often used for rare and precious samples, the time investment in acquiring samples and performing analysis is higher than for flow cytometry. Thus, for researchers seeking to acquire and analyze data quickly, but requiring more colors than are available on conventional instruments, spectral cytometry provides a potential opportunity. Moreover, the use of the same fluorophore-

**Figure 7.** Autofluorescence correction performed on WNV-infected brain cells. (**A**) Spectral signatures generated on the spectral system for unstained cells, BV510-labeled beads, and FITC-labeled beads. Fully stained samples unmixed on the spectral system (**B**) without and (**C**) with autofluorescence correction. (**D**) Spectral signatures generated on the spectral system for unstained cells and BV605-labeled beads. Fully stained samples unmixed on the spectral system (E) without and (**F**) with autofluorescence correction. (**G**) Spectral signatures generated on the spectral system for unstained cells and BV785-labeled beads. Fully stained samples unmixed on the spectral system (**H**) without and (**I**) with autofluorescence correction for BV785-CD11c. For each plot, percentages of cells in each populations are show, as well a resolution ratio for each population, defined as the median of the positive population, divided by the 99th percentile of the negative population. [Color figure can be viewed at wileyonlinelibrary.com]

conjugated antibodies, staining, and analysis techniques as conventional cytometry make this a well-characterized, readily accessible technique, while also allowing an increased number of markers to be measured. Additionally, researchers using smaller panels may benefit from the flexibility of the system, with a larger range of fluorophores being compatible with the system, aiding panel design.

While spectral approaches to fluorescence cytometry have been developed for some time, spectral cytometry is an emerging technology in the commercial space and is still maturing. However, the nature of the spectral approach exhibits several clear advantages over conventional cytometry and should be incorporated into routine cytometry approaches where possible.

## Acknowledgments

Thomas Ashhurst is supported by the International Society for the Advancement of Cytometry (ISAC) Marylou Ingram Scholars Program. Paula Niewold is supported by the International Society for the Advancement of Cytometry (ISAC) Marylou Ingram Scholars Program. This work was supported by National Health and Medical Research Council Project Grant 1088242 and a grant from the Merridew Foundation.

## Author Contributions

**Paula Niewold:** Conceptualization-Lead, Data curation-Equal, Formal analysis-Equal, Investigation-Equal, Methodology-Equal, Project administration-Lead, Software-Equal, Supervision-Equal, Validation-Equal, Visualization-Equal, Writing-original draft-Lead, Writing-review & editing-Equal. **Thomas Ashhurst:** Conceptualization-Equal, Data curation-Equal, Formal analysis-Equal, Investigation-Equal, Methodology-Equal, Software-Equal, Validation-Equal, Visualization-Equal, Writing-original draft-Equal, Writing-review & editing-Equal. **Adrian Smith:** Conceptualization-Equal, Formal analysis-Supporting, Investigation-Supporting, Methodology-Supporting, Resources-Equal, Supervision-Equal, Writing-review & editing-Supporting. **Nicholas King:** Conceptualization-Supporting, Funding acquisition-Lead, Investigation-Supporting, Methodology-Supporting, Project administration-Supporting, Resources-Equal, Supervision-Equal, Writing-original draft-Supporting, Writing-review & editing-Equal.

## Literature Cited

1. Roederer M. Spectral compensation for flow cytometry: Visualization artifacts, limitations, and caveats. Cytometry 2001;45(3):194–205.
2. Roederer M. Compensation in flow cytometry. Curr Protoc Cytom 2002;22: 1.14.1–1.14.20. https://doi.org/10.1002/0471142956.cy0114s22
3. Bagwell CB, Adams EG. Fluorescence spectral overlap compensation for any number of flow cytometry parameters. Ann N Y Acad Sci 1993;677:167–184.
4. Nguyen R, Perfetto, S, Mahnke, YD, Chattopadhyay, P, Roederer, M. Quantifying spillover spreading for comparing instrument performance and aiding in multicolor panel design. Cytom Part A 2013;83A(3):306–315.
5. Ashhurst TM, Smith AL, King NJC. High-dimensional fluorescence cytometry. Curr Protoc Immunol 2017;119:5 8 1–5 8 38.
6. Mair F, Prlic M. OMIP-44: 28-color immunophenotyping of the human dendritic cell compartment. Cytometry A 2019;95A(8):925–926.
7. Nettey L, Giles AJ, Chattopadhyay PK. OMIP-050: A 28-color/30-parameter fluorescence flow cytometry panel to enumerate and characterize cells expressing a wide Array of immune checkpoint molecules. Cytometry A 2018;93A(11):1094–1096.
8. Robinson J, Rajaw B, Gregori G, Jones J, Patsekine V. Collection hardware for high speed multispectral single particle analysis. Congress of the International Society for Analytical Cytology 2004; p. 12.
9. Robinson J. Multispectral cytometry: The next generation. Biophoton Int 2004;8: 36–40.
10. Robinson JP, Rajwa B, Gregori G, Patsekin. Multispectral Detector and Analysis System. 2007; Purdue University, US patent 72,802,042,007.
11. Robinson JP. Spectral flow cytometry-Quo vadimus? Cytom Part A 2019;95A(8): 823–824.
12. Nolan JP, Duggan E, Liu E, Condello D, Dave I, Stoner SA. Single cell analysis using surface enhanced Raman scattering (SERS) tags. Methods 2012;57(3):272–279.
13. Nolan JP, Condello D. Spectral flow cytometry. Cur Protoc Cytom 2013;63(1):27. http://dx.doi.org/10.1002/0471142956.cy0127s63.
14. Nolan JP et al. Visible and near infrared fluorescence spectral flow cytometry. Cytom Part A 2013;83A(3):253–264.
15. Futamura K, Sekino M, Hata A, Ikebuchi R, Nakanishi Y, Egawa G, Kabashima K, Watanabe T, Furuki M, Tomura M. Novel full-spectral flow cytometry with multiple spectrally-adjacent fluorescent proteins and fluorochromes and visualization of in vivo cellular movement. Cytom Part A 2015;87A(9):830–842.
16. Schmutz S, Valente M, Cumano A, Novault S. Spectral cytometry has unique properties allowing multicolor analysis of cell suspensions isolated from solid tissues. PLoS One 2016;11(8):e0159961.
17. Park LM, Lannigan J, Jaimes, MC. OMIP-069: Forty-Color Full Spectrum Flow Cytometry Panel for Deep Immunophenotyping of Major Cell Subsets in Human Peripheral Blood. Cytometry Part A. 2020. https://doi.org/10.1002/cyto.a.24213.
18. Zimmermann T. Spectral imaging and linear unmixing in light microscopy. Adv Biochem Eng Biotechnol 2005;95:245–265.
19. Novo D, Gregori G, Rajwa B. Generalized unmixing model for multispectral flow cytometry utilizing nonsquare compensation matrices. Cytom A 2013;83A(5): 508–520.
20. Ashhurst TM, Cox DA, Smith Al, King NJC. Analysis of the bone marrow haematopoietic system using mass and flow cytometry. In: McGuire HM, Ashhurst TM, editors. Protocols in Mass Cytometry, Methods in Molecular Biology, New York, NY: Springer, 2019.
21. Dorward DA, Lucas CD, Alessandri AL, Marwick JA, Rossi F, Dransfield I, Haslett C, Dhaliwal K, Rossi AG. Technical advance: Autofluorescence-based sorting: Rapid and nonperturbing isolation of ultrapure neutrophils to determine cytokine production. J Leukoc Biol 2013;94(1):193–202.
22. Bertolo A, Baur M, Guerrero J, Pötzel T, Stoyanov J. Autofluorescence is a reliable in vitro marker of cellular senescence in human mesenchymal stromal cells. Sci Rep 2019;9(1):2074.
23. Lawrence WG, Varadi G, Entine G, Podniesinski E, Wallace PK. A comparison of avalanche photodiode and photomultiplier tube detectors for flow cytometry. SPIE BiOS 2008;6859. https://doi.org/10.1117/12.758958.
24. Stoeckius M, Hafemeister C, Stephenson W, Houck-Loomis B, Chattopadhyay PK, Swerdlow H, Satija R, Smibert P. Simultaneous epitope and transcriptome measurement in single cells. Nat Methods 2017;14(9):865–868.
25. Hu Y, Huang K, An Q, Guizhen D, Hu G, Xue J, Zhu X, Wang C, Xue Z, Fan G. Simultaneous profiling of transcriptome and DNA methylome from a single cell. Genome Biol 2016;17:88.
26. Mimitou E, Cheng A, Montalbano A, Hao S, Stoeckius M, Legut M, Roush T, Herrera A, Papalexi E, Ouyang Z, et al. Expanding the CITE-seq tool-kit: Detection of proteins, transcriptomes, clonotypes and CRISPR perturbations with multiplexing, in a single assay. Nat Methods 2018:16(5):409–412.

Received: 16 October 2021 | Revised: 26 April 2022 | Accepted: 15 June 2022

DOI: 10.1002/cyto.a.24667

ORIGINAL ARTICLE

ISAC CYTOMETRY Journal of Quantitative Cell Science PART A

# Development of a 27-color panel for the detection of measurable residual disease in patients diagnosed with acute myeloid leukemia

Kah Teong Soh | Alexis Conway | Xiaojun Liu | Paul K. Wallace

Department of Flow and Image Cytometry, Roswell Park Comprehensive Cancer Center, Buffalo, New York, USA

**Correspondence**
Kah Teong Soh, Roswell Park Comprehensive Cancer Center, Buffalo, NY, USA
Email: kahteong@buffalo.edu

## Abstract

Acute myeloid leukemia (AML) measurable residual disease (MRD) evaluated by multiparametric flow cytometry (MFC) is a surrogate for progression-free and overall survival in clinical trials and patient management. Due to the limited number of detection channels available in conventional flow cytometers, panels used for assessing AML MRD are typically split into multiple tubes. This cripples the simultaneous and correlated assessment of all myeloblast measurements. In response, we prototyped a single-tube 27-color MFC assay for the evaluation of AML MRD, incorporating all recommended markers. Marrow aspirates from 22 patients were processed for analysis using full spectrum flow cytometry (FSFC). The signal resolution of each marker was compared between samples stained with single antibody vs. the fully stained panel. The analytical accuracy for quantifying hematopoietic cells between our established 8-color assay and the new 27-color method were compared. Variations within an operator and between separate operators were assessed to evaluate the assays reproducibility. The limited of blank (LOB), limit of detection (LOD), and lower limit of quantification (LLOQ) of the 27-color method were empirically determined using limiting dilution experiments. The stability of antibody cocktails over a period of 120 h was also studied using cryopreserved marrow cells. The stain indices for all antibodies were lower in the fully stained panel compared to cells stained with one antibody but clear separations between negative and positive signals were achieved for all antibodies. Our results demonstrated a high concordance between the established 8-color method and the new 27-color assay for enumerating myeloblasts and MRD interpretation within and between operators. The data further showed that the single-tube 27-color assay easily achieved the minimum required detection sensitivity of 0.1%. When antibodies were combined, however, expression intensity of some antigens deteriorated significantly when stored. Our single-tube 27-color panel is a suitable, high sensitivity flow cytometric approach that can be used for AML MRD testing, which improves the correlation of aberrant antigens and detection of asynchronous differentiation patterns. Based on the stability study, we recommend the full panel be made prior to staining.

**KEYWORDS**

acute myeloid leukemia, full Spectrum flow cytometry, high sensitivity, measurable residual disease

 

## 1 | INTRODUCTION

Acute myeloid leukemia (AML) is a heterogeneous group of diseases characterized by more than 20% abnormal immature myeloblasts in the bone marrow [1]. It is diagnosed based on a combination of morphology assessment, genetic aberrancies, and its immunophenotypic profile. Even though AML patients can be stratified into favorable, intermediate, and adverse-risk groups based on their cytogenetic profiles, their responses to therapy within each group varies widely [2, 3]. The 5-year survival rate has significantly improved since the 1970s, but only 26% of patients diagnosed with AML will survive more than 5 years, and as many as 70% of patients older than 65 years will succumb to the disease within 1 year of diagnosis [4, 5]. A myriad of factors presenting at initial diagnosis such as age, cytogenetics, mutational profile, and remission status following treatment have been associated with prognosis, but they have all failed to accurately predict outcomes [2, 6–8].

The identification of residual leukemic cells following therapy, termed measurable residual disease (MRD; formerly known as minimal residual disease), has emerged as an important independent prognostic indicator for many hematological malignancies including AML [9–12]. When used in conjunction with other available clinical information such as cytogenetics and molecular data, monitoring of MRD levels can serve as a surrogate to establish a deeper remission status for risk stratification [13]. Together, these parameters can help predict patient outcomes, inform post-remission treatment, and enable early intervention when necessary. Furthermore, MRD status has the potential to replace traditional endpoints used in clinical practice to accelerate drug testing and regulatory approval.

The detection of MRD, however, can be challenging due to the rarity and heterogeneity of neoplastic cells. High sensitivity methods that can detect the presence of leukemic cells down to levels of $10^{-4}$–$10^{-6}$ white blood cells are required. Multiparametric flow cytometry (MFC) is a suitable technique for monitoring MRD due to its high degree of detection sensitivity and specificity. This technique is also accessible to many laboratories, applicable to more than 90% of AML patients, and can be used to distinguish normal vs. abnormal blasts [14]. Many studies have independently demonstrated MFC to highly correlate with event-free survival and can be more predictive than traditional approaches such as morphology and cytogenetics [9, 15–17].

Distinguishing abnormal blasts from normal maturing myeloid progenitors by MFC based on their antigen expression profiles is challenging. This is because the endogenous bone marrow microenvironment is dynamic and heterogeneous, and there is no single typical 'AML immunophenotype' that can be used to distinguish abnormal blasts from normal maturing myeloid progenitors. Identification of abnormal myeloblasts is further complicated by the acquisition of atypical antigens post-treatment by normal recovering myeloblasts. Two different approaches are used for the evaluation of residual AML by MFC; the Leukemia Associated ImmunoPhenotype (LAIP) approach and Different from Normal (DfN) approach, as summarized by the European LeukemiaNet Working Party (ELN) [18]. In the LAIP-based approach, the phenotype of immature blasts is assessed at diagnosis and followed post-therapy. The aberrancies detected are mainly characterized by cross lineage expression of non-myeloid antigens on myeloid blasts (e.g., CD5, CD7, CD56), asynchronous expression of maturation-associated antigens on immature cells (e.g., CD11b), and lack of expression (e.g., CD13, CD33) or overexpression (e.g., CD33, CD34, CD117) of myeloid-related antigens. Unlike bulk testing methods such as molecular assays, MFC allows for the interrogation of many markers at the single cell level, allowing the precise delineation of many cellular subsets within a patient's sample. The DfN strategy compares the antigen differentiation expression patterns on suspected residual leukemic cells with those of normal myeloblasts. Although similar, this is not an approach strictly reliant on a fixed LAIP, which can alter following therapy or clonal evolution and does not require a diagnostic sample.

The successful implementation of a flow-based AML MRD assay requires excellent technical expertise, careful consideration of the antibody fluorochrome combinations, standardized flow data analysis, and extensive knowledge about normal and abnormal bone marrow expression patterns of the selected CD markers [19]. Due to the limited capability of contemporary flow cytometers approved for clinical use to detect more than 12 markers simultaneously, a typical MFC panel recommended for monitoring AML MRD usually consists of a more than one tube, each with distinct functions [20]. One tube is often designed to observe the early maturation of hematopoietic stem cells into each of the major cell lineages and typically consist of antibodies targeting CD13, CD15, CD19, CD33, CD34, CD38, CD45, CD71, and CD117. A second tube may be used to observe the maturation of early myelomonocytic precursors to later-stage mature forms and typically consists of CD4, CD13, CD14, CD16, CD34, CD38, CD45, CD64, CD123, and HLADR. Markers in this tube can also be used to identify plasmacytoid dendritic cells and basophil lineages. A third tube may be used to identify the abnormal expression of T and NK cells-associated lymphoid antigens on progenitor populations and would typically consist of antibodies targeting CD2, CD5, CD7, CD33, CD34, CD38, CD45, CD56, and HLADR.

Technological advances in recent years have enabled the simultaneous assessment of a higher number of parameters in a correlated fashion, improving the ability to detect aberrant antigens and asynchronous differentiation patterns. Until recently, most clinical laboratories were combining no more than 10 antibodies per tube. The introduction of full spectrum flow cytometry (FSFC) by Cytek Biosciences and cytometry by time of flight (CyTOF) by Fluidigm represent revolutionary platforms that allow for a high-dimensional acquisition of data generated from 40 or more antibodies. While both technology platforms have advantages and disadvantages in terms of characterizing low frequency populations, studies reported better cell recovery and faster acquisition times with the FSFC approach [21, 22]. By measuring the full spectrum of light emissions from each interrogated fluorochrome, FSFC can distinguish between emissions from combinations of fluorochromes that conventional MFC systems cannot; for example, the concurrent detection of APC and Ax647 fluorochrome-generated spectra, which share near identical emission peaks. This

provides a new avenue to combine all routinely used AML MRD markers into one single tube, for a comprehensive immunophenotypic analysis by FSFC. Due to the increased flexibility of FSFC, antibody panels can be expanded to include a viability dye and additional antigens of interest [23, 24]. This eliminates the redundancy of markers used in multi-tubes system, lowering the reagent cost associated with the assay.

In this manuscript, we developed a single-tube 27-color flow cytometric assay for the evaluation of AML MRD. The panel was created using commercially available fluorochrome-conjugated monoclonal antibodies and optimized after several rounds of trial and error. We evaluated whether the high number of antibodies incorporated in the final panel would decrease staining resolution between positive and negative signals, partly due to fluorochrome spread, steric hindrance, and/or the unmixing algorithm [22, 25]. To verify this, we compared the performance of antibodies when they were used alone vs. when they were used conjointly with all other antibodies in the panel. To test the analytical accuracy of this novel 27-color method, a concordance study was performed to evaluate the numbers and percentages of various cell populations as detected by FSFC with results obtained from our established 8-color MFC panel as the predicate. The limit of blank (LOB), limit of detection (LOD), and lower limit of quantification (LLOQ) were empirically established to determine if the assay met the established minimum required detection sensitivity of 0.1% for assessing AML MRD [18]. To investigate if consistent results could be repeatedly attained for meaningful interpretation, intra- and inter-operator variation was studied.

Even though antibody cocktails are considered indispensable in the clinical flow laboratory for assuring assay consistency, storage of the 27-color panel for more than 24 h resulted in interactions between fluorochromes and tandem breakdown, causing loss of fluorochrome brightness and/or changes in antigen expression profiles [26, 27]. Overall, our results demonstrated this single-tube 27-color assay could serve as a template for the future development and validation of a clinical method to process and analyze bone marrow samples for AML MRD testing, allowing for the simultaneous correlation of aberrant antigens and detection of asynchronous differentiation patterns.

## 2 | MATERIALS AND METHODS

### 2.1 | Bone marrow aspirates

This study was reviewed and approved by the Institutional Review Board at Roswell Park Comprehensive Cancer Center (STUDY ID 00001640/BDR 145221). A total of 22 sodium heparinized, de-identified bone marrow samples from patients with suspected AML MRD, and three de-identified staging marrows negative for AML received by Roswell Park's Clinical Flow Cytometry Laboratory were used after all requested testing had been performed. All bone marrow aspirates were processed within 24 h of collection, except for testing antibody cocktail stability; in which case leukocytes were separated by ficoll density gradient centrifugation and cryopreserved prior to thawing for surface labeling.

### 2.2 | Panel design

The initial fluorochrome combinations for the 27-color panel were selected based on antigen density, fluorochrome intensity, expression profile, and reagent availability. Using Cytek's Full Spectrum Viewer, an online tool that helps determine the compatibility of fluorochrome combinations, relevant fluorochrome-conjugated antibodies were selected and gradually added to the backbone panel. As a rule of thumb, the addition of a new fluorochrome to the panel should not significantly increase the Complexity™ Index, which is an overall measure of uniqueness of all dyes in a full spectrum cytometry panel; the Complexity™ Index of our final panel was 29.6. The composition and sources of the final panel can be found in Table S1. The full spectrum can be found in Figure S1. For a list of fluorochrome-conjugated antibodies used in our established 8-color panel, see Table S2.

### 2.3 | Cell preparation and staining

The bone marrow cells were processed using our conventional wash-stain-lyse-wash method [28]. Briefly, bone marrow aspirates were collected and filtered using 70 μm cell strainer (Millipore Sigma; Cat #Z742103) to exclude spicules, washed once using flow cytometry buffer (FCM; Leinco Technologies; Cat #S622; containing 0.5% bovine serum albumin, 0.1% sodium azide, and 0.04 g/L tetrasodium EDTA in phosphate-buffered saline), and resuspended to $1 \times 10^7$ cells/ml. Two hundred microliters of the washed bone marrow cells were transferred to a 12 × 75 mm polystyrene round-bottom tube (Corning; Cat #352052) and incubated with mouse IgG (Invitrogen; Cat #10400C) for 10 min to block Fc receptors. The cells were then stained according to the antibody panel outlined in Table S1 for 30 min at room temperature. To preserve the integrity of the fluorochromes, all staining procedures were performed in the dark. To achieve optimal performance, all antibodies were tittered and used at saturating concentrations. The cells were lysed for 5 min using 2 ml of ACK Lysing Buffer (Thermo Fisher Scientific; Cat #A10492-01), washed using 3 ml of FCM buffer, and centrifuged at 540×*g* for 5 min. The supernatant was discarded, and the cell pellet was resuspended in 500 μl of FCM buffer for acquisition on Cytek® Aurora. Flow cytometric data for all samples were acquired immediately after staining and unless otherwise specified, a minimum of 500,000 events were collected for each file.

### 2.4 | Cryopreservation and thawing of marrow cells

For testing antibody cocktail stability over time, bone marrow samples from AML patients with relapsed disease were frozen at −152°C and thawed immediately prior to staining. For cryopreservation, fresh

marrow aspirates were layered on top of Lymphocyte Separation Media (Corning; Cat #25-072-CV) and centrifuged at 400×*g* for 30 min without brake. Mononuclear cells were transferred to a new 15-mL high-clarity polypropylene falcon tube (Corning; Cat #352196), washed with PBS, and resuspended in ice-cold RPMI 1640 with L-glutamine (Corning Cellgro; Cat #10-040-CV) and supplemented with 10% heat inactivated fetal bovine serum (Biotechne; Cat #S11150H). Freezing solution, consisting of 80% heat inactivated fetal bovine serum and 20% DMSO (Corning Cellgro; Cat #25-950-CQC), was added dropwise to the cells at 1:1 ratio while agitating and slowly frozen in an ethanol bath to -80°C before being transferred to the −152°C freezer. At $T = 0$, 24, 48, 72, 96, and 120 h, frozen cells were thawed by incubating in a water bath pre-warmed to 37°C for 2 min, transferred to complete media with DNase (70 U/ml Sigma-Aldrich; Cat #D4513), incubated for 15 min, washed, and resuspended in FCM Buffer.

## 2.5 | Establishing detection sensitivities

The current consensus from European LeukemiaNet recommends a minimum of 500,000 and up to 1 million leukocytes be acquired to achieve a detection sensitivity of 0.1% as the cut-off between MRD positive and MRD negative [18]. It should, however, be noted that MRD quantification below 0.1% may still represent residual leukemic cells. To empirically determine the ability of our 27-color assay to detect rare events, a limiting dilution experiment was performed and the LOB, LOD, and LLOQ were established in accordance with Clinical Laboratory Standards Institute recommendations [29].

For establishing LOB and LOD, staging marrows samples were stained with all the antibodies in Table S1 except CD34 and CD117. A minimum of 1 million events was acquired and the assay was performed in duplicate on three different bone marrow samples. The LOB was calculated as the average percentage of CD34+/CD117+ events falling into the blast region (e.g., CD45dim, SSC-low) plus 1.645 times the standard deviation. The LOD was similarly calculated as the average percentage of events falling into this region plus three times the standard deviation. For the determination of LLOQ, suitable bone marrow aspirates from patients relapsing from AML MRD exhibiting an abnormally high CD34+/CD117+ count were identified. These bone marrow samples were stained with the antibodies listed in Table S1 and diluted in AML negative bone marrow samples stained with all antibodies except CD34 and CD117. Serial 1:10 dilutions were made based on the total leukocyte counts of each sample. A minimum of 1 million events was acquired at each dilution. The LLOQ was considered achieved at the dilution immediately preceding the dilution where the coefficient of variation (CV) of the CD34+/CD117+ percentage exceeded 30%. The experiment was performed three times in duplicate. Note that by excluding CD34 and CD117 antibodies from the samples used to determine LOB and LOD and from the sample AML negative bone marrow sample used to dilute the sample for the LLOQ measurement will create an artificially clean background that will lead to an overestimation of the LOB, LOD, and LLOQ.

## 2.6 | Intra- and inter-operator variability

To examine intra-operator precision and variability, a marrow aspirate from a patient with relapsed AML was repeatedly processed and analyzed by the same individual five times. Fifty thousand events were collected for each repeat and the coefficients of variation of the frequency of blast, T, B, and NK cells were assessed. For examining inter-operator variability, two operators independently stained, acquired, and analyzed in triplicate identical samples. A minimum of 950,000 events was acquired for each sample determination. This experiment was repeated on four different samples and the coefficient of variations was computed.

## 2.7 | Antibody cocktail stability

An antibody cocktail was prepared by adding all fluorochrome-conjugated antibodies into a 15-mL falcon tube containing Brilliant Stain Buffer (BD Biosciences; Cat #563794) and stored at 4°C in the dark. Frozen mononuclear cells were thawed, and surface stained with the prepared antibody cocktail at $T = 0$, 24, 48, 72, 96, and 120 h. The median fluorescence intensity of each marker on positive populations was monitored, graphed, and tabulated.

## 2.8 | Acquisition and data analysis

All cells processed using the 27-color panel were acquired on the Cytek® Aurora (Cytek Biosciences, CA, USA) equipped with 355 nm (20 mW, 16 channels), 405 nm (100 mW, 16 channels), 488 nm (50 mW, 14 channels), and 638 nm (80 mW, eight channels) as the excitation sources. The instrument was warmed up on for at least 30 min prior to use, and quality-controlled using SpectraFlo® QC Beads (Cytek; Cat #N7-97355) to adjust laser performance based on baseline settings, laser delay, and to align height and area scaling factors for optimal signal resolution. This ensured consistent performance was achieved daily. To maximize signal resolution of measured fluorescent probes, 'autofluorescence extraction' was enabled by default during sample acquisitions. Prior to analysis, the quality of the acquired and unmixed data was examined using FCS Express v7 (De Novo Software). Minor post-acquisition unmixing issues were manually corrected when the biology of the markers was known and exported in FCS format. All cells processed using the 8-color panel were acquired on a BD Canto II flow cytometer equipped with 405 nm (30 mW), 488 nm (20 mW), and 633 nm (20 mW) lasers. BV421 and BV510 were excited by the 405 nm laser and detected using 450/50 and 510/50 nm bandpass filters; FITC, PE, and PECy7 were excited by 488 nm laser and detected using 530/30, 585/42, and 780/60 nm bandpass filters; PerCP Cy5.5 was excited by 488 nm laser and detected using 670 nm long pass filter; APC and APCH7 were excited by 633 nm laser and detected using 660/14 and 780/60 nm bandpass filters. All results and flow cytometric plots shown in this study were generated using WinList v10 (Verity Software House).

ISAC CYTOMETRY Journal of Quantitative Cell Science PART A

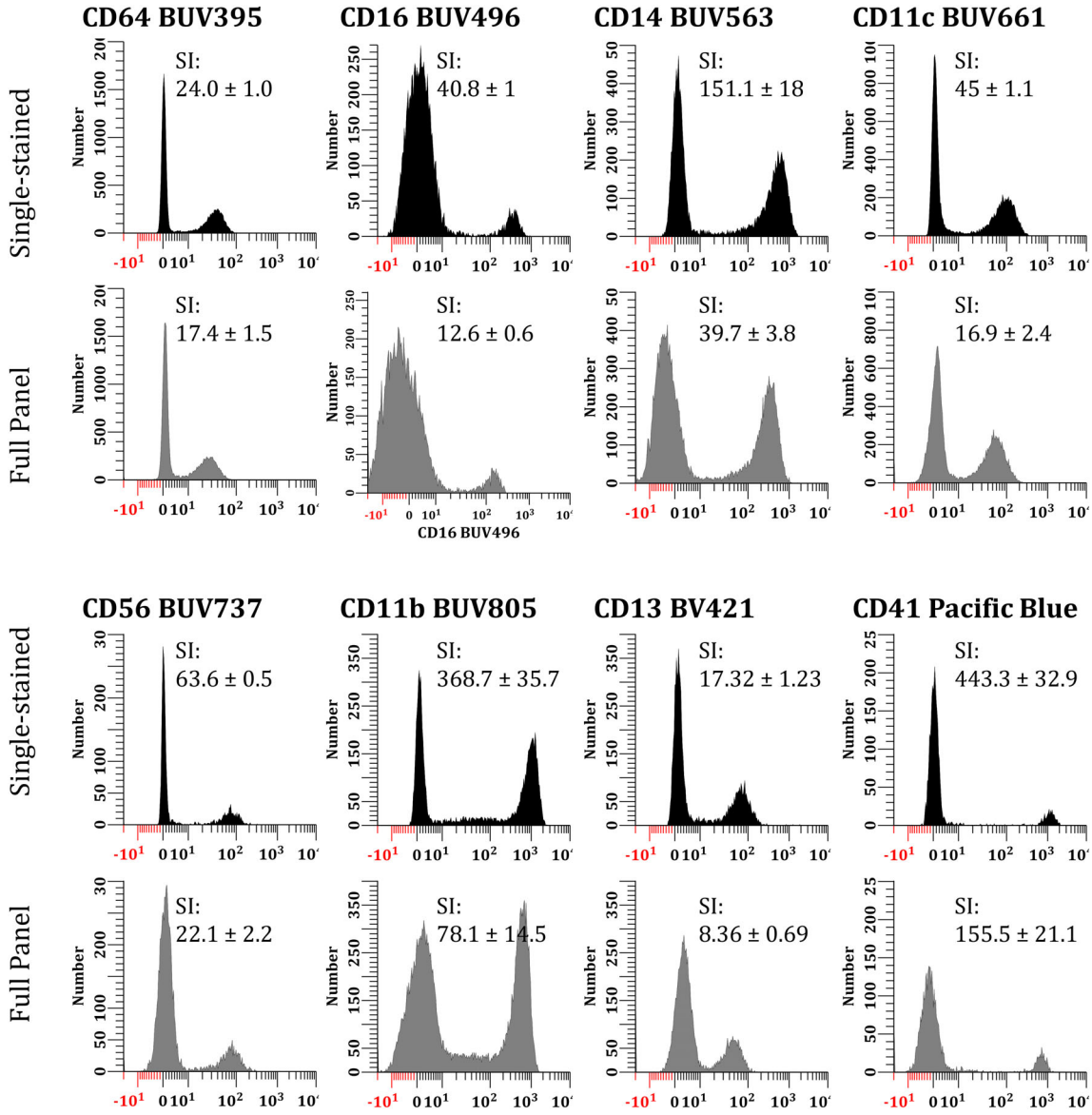


**FIGURE 1** Antibody resolution in 27-color acute myeloid leukemia (AML) measurable residual disease (MRD) assay: single stained vs. fully stained. Similar to conventional flow cytometry, the detection of 27 antibodies by full spectrum flow cytometry (FSFC) can be compromised by the complexity of unmixing, signal resolution, and steric hinderance. To evaluate this, the performance of each antibody to resolve cell populations was tested using the antibody alone (black histograms) vs. staining with all antibodies in the full panel (gray histograms). Stain index (SI) was used as the primary measure to assess the separation between positive and negative signals. The evaluation of all markers, except for CD41 Pacific blue, CD15 BV605, CD117 BV785, and CD34 APC, was performed using a 'mononuclear gate' gate based on FSC-A versus SSC-A. CD41 was gated on platelets using SSC-A low vs FSC-A low, CD15 was gated on neutrophils using SSC-A hi vs. FSC-A hi), and both CD34 and CD117 were gated on the blast region using CD45 dim versus SSC-A low. This study was repeated using bone marrow from AML MRD negative ($n = 2$) and positive ($n = 1$) samples each performed in triplicate. A minimum of 100,000 events was acquired for each sample (average: 160,365 events)

## 3 | RESULTS

### 3.1 | Signal resolution

While the high number of markers used in a single tube enabled us to perform high-dimensional analysis, the resolution between positive and negative populations can be compromised due to increased fluorochrome spillover and steric hindrance. Stain indices were computed to assess the performance of antibodies when used alone vs. when used in the full panel. Our experimental results showed that the stain indices for all antibodies were lower in the fully stained panel when compared to cells stained with just one antibody (Figure 1).

The stain index is calculated by dividing the difference between median fluorescence intensity (MFI) of the positive and negative populations by two times the robust standard deviation of the negative population. The MFI of positive signals were lower and the robust

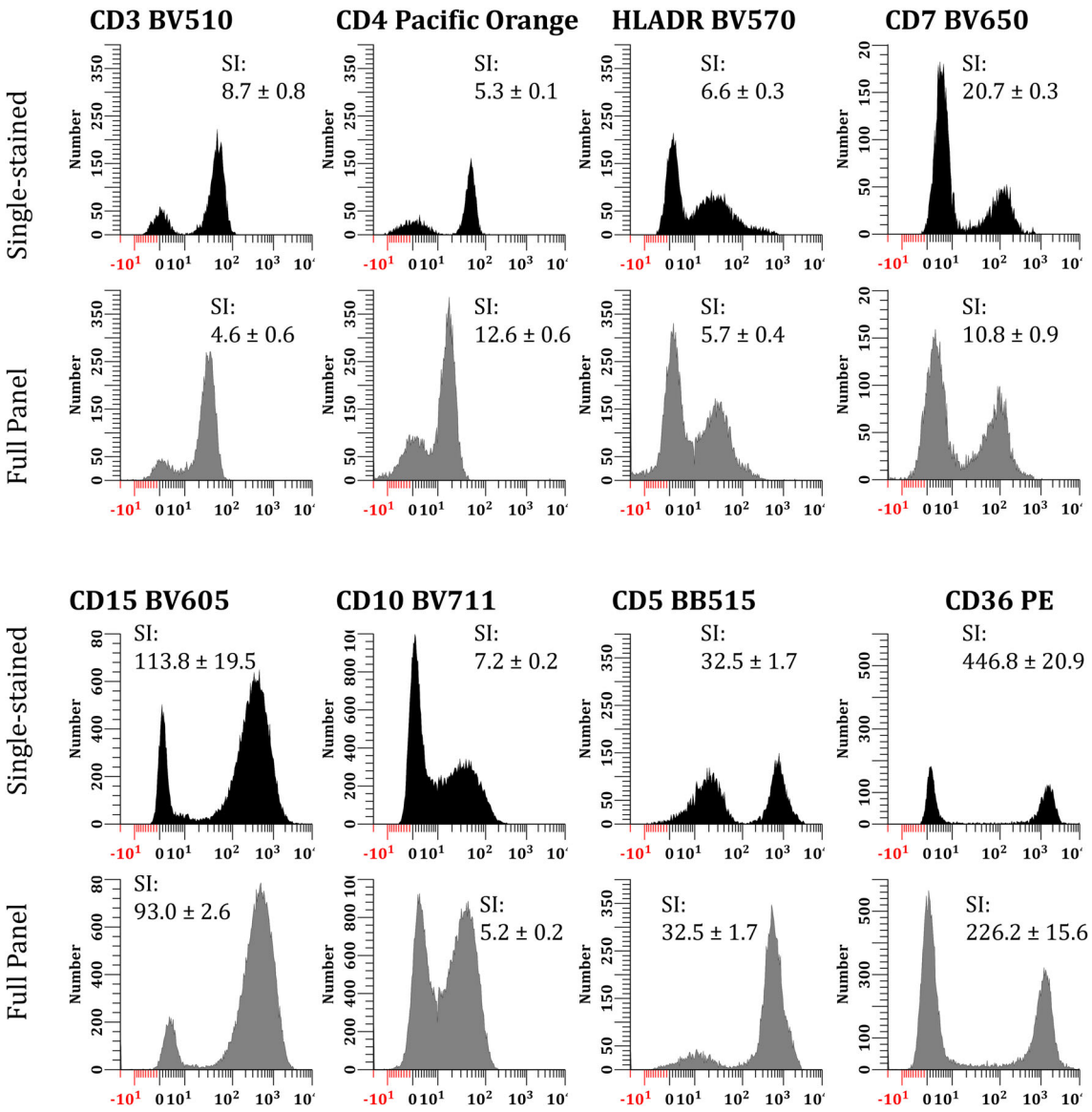


**FIGURE 1** (Continued)

standard deviations of negative signals were higher in fully stained samples (Table S3). In all instance, however, clear separation was achieved between the negative and positive signals for each antibody included in this panel (Figures 1 and S3).

## 3.2 | Identification and characterization of immature blasts using the 27-color assay

A sequential gating strategy, as described in Figure S2, was developed to define, the lymphocyte subsets, monocytes, granulocytes, and blast cells. Briefly, viable, singlet, aggregate free cells were identified using a combination of forward scatter (FSC), side scatter (SSC), and a fixable live dead viability dye. Normal maturing B cell precursors (i.e., hematogones) which fall in the blast cell region and can be CD34+ were excluded based on their CD19+ expression.

We evaluated 22 bone marrow samples. Seventeen samples were confirmed to have residual AML using the combined DfN and LAIP methods and five were found to be negative for residual disease based on the flow cytometric interpretation. An example of selected bivariate flow cytometric data plots used for discriminating normal versus abnormal blasts is shown in Figure 2. The maturation patterns of normal bone marrow blasts (blue events) overlaid with those from a patient with relapsed AML (red events) demonstrates some of the subtle differences between normal and abnormal. All 22 samples assayed using the 27-color assay, whether phenotypically negative ($n = 5$) or positive ($n = 17$) for AML, were found to correlate with the 8-color assay interpretations. While all parameters were helpful for discriminating normal from abnormal, the expression patterns of CD45, CD34, CD117, HLADR, CD13, CD33, CD7, CD11b, and CD56 were often most useful. In the one case of myelomonocytic leukemia, evaluation of

ISAC CYTOMETRY Journal of Quantitative Cell Science PART A

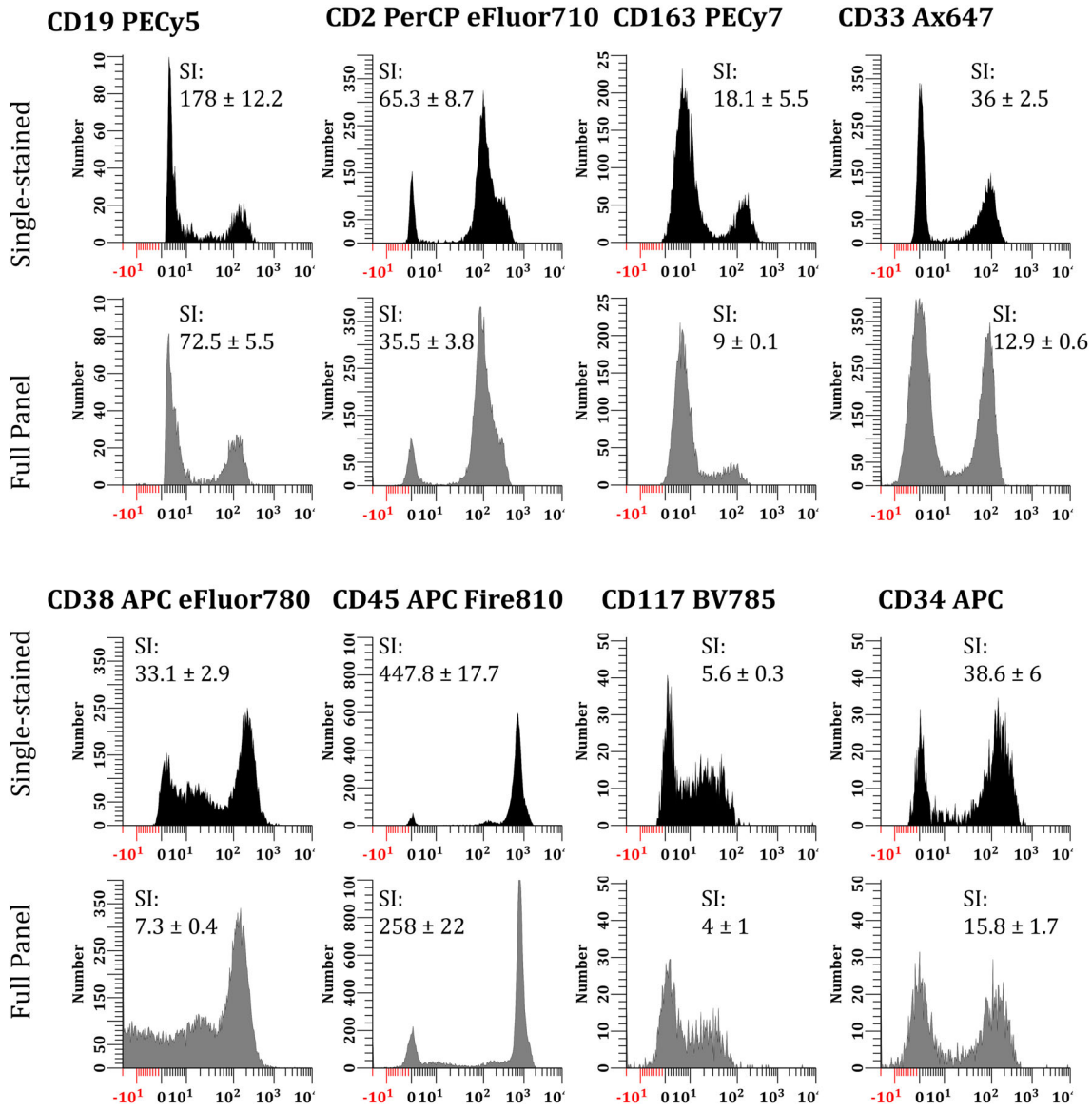


**FIGURE 1** (Continued)

CD4, CD14, CD64, and CD163 also facilitated the identification of residual disease.

### 3.3 | Analytic accuracy of the 27-color spectral assay

To assess the performance of our 27-color assay, a parallel study was performed using this new method and the established 8-color approach employed by the Clinical Flow Laboratory at Roswell Park. The percentages of B cells, NK Cells, CD34+ blasts, CD117+ blasts, CD34+/CD117+ blasts, and HLADR+/CD34+/CD117+ blasts were calculated and compared between methods. An analysis based upon the 95% confidence interval was performed using fold change, mathematically derived by dividing the percentage of cells detected using the 27-color by the 8-color methods. As shown in Table 1, our experimental results indicated there was no evidence to suggest that the 27-color method detected different percentages of B cells, NK Cells, CD34+ blasts, CD117+ blasts, CD34+/CD117+ blasts, and HLADR+/CD34+/CD117+ blasts from the established 8-color assay. Using regression analysis, a strong correlation between the numbers of B cells ($r^2 = 0.957$), NK Cells ($r^2 = 0.938$), CD34+ blasts ($r^2 = 0.921$), CD117+ blasts ($r^2 = 0.986$), CD34+/CD117+ blasts ($r^2 = 0.991$), and HLADR+/CD34+/CD117+ blasts ($r^2 = 0.881$) was seen between both assays (data not shown).

### 3.4 | Detection sensitivity

The LOB and LOD, calculated as described in the Materials and Methods, were 7.33 events (0.001%) and 9.24 events (0.0013%), respectively. Using a limiting dilution assay, our results demonstrated

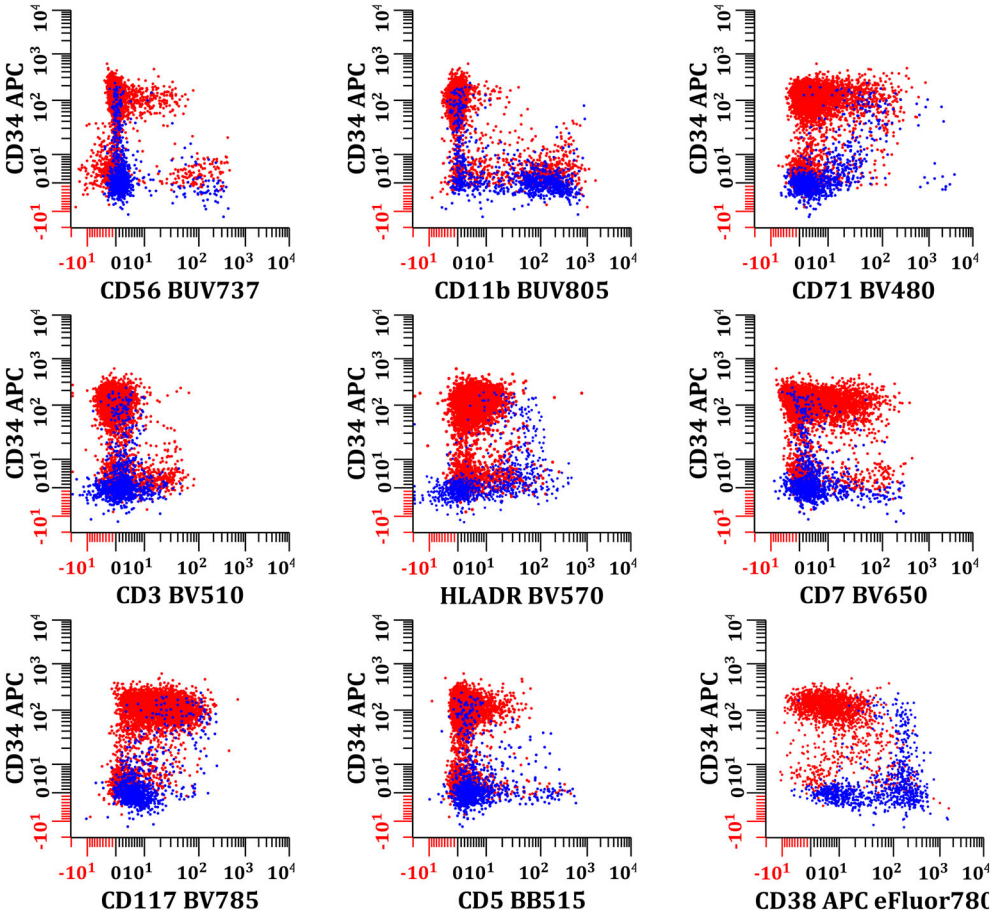


**FIGURE 2** Discrimination of normal vs. abnormal myeloblasts using the 27-color multiparametric flow cytometry (MFC) panel. Representative data from two bone marrow samples received for acute myeloid leukemia (AML) measurable residual disease (MRD) assessment one negative for MRD (blue dots) and the other positive (red dots). All events shown fell within the blast cell region defined as CD45 dim versus SSC-A low and negative for CD19. These abnormal myeloblasts atypically express CD5, CD7, CD11b, and are negative to dim for HLADR. They also demonstrate maturation arrest based on CD38 dim expression and have a higher frequency. 1,502,392 and 1,157,280 cells were acquired for the normal and abnormal samples, respectively.

that the single-tube 27-color method easily achieved the minimum required detection sensitivity of 0.1% for an AML MRD evaluation (Figure 3). As shown in Table 2, our assay was able to accurately quantify blast cells at a frequency of 0.0045% with a coefficient of variation of 25.79%, which was less than our pre-defined and the generally accepted 30% cut-off. This is an order of magnitude more sensitive than our predicate 8-color assay, which achieved a LOD of 0.07% in a similar series of dilution experiments.

### 3.5 | Intra- and inter-operator reproducibility

Three different operators who possess significant experience in handling specimens for flow cytometric processing were included in this study. For intra-operator variability, the staining was repeated five times by a single operator. Our results demonstrated CVs of approximately 1%–4% consistently for the recovery and enumeration of all populations studied except for monocytes, for which a slightly higher but acceptable, CV of 14% was observed (Table 3).

For inter-operator variability, two different operators consistently achieved low CVs for all populations measured in different samples (Table 4). The only exception was Sample #3, where the CVs for enumerating total T cells, B Cells, monocytes, and NK cells were slightly higher than for the other samples. Taken together, consistent and reproducible enumeration was achieved for all cell populations with CVs less than 20% with the 27-color assay. We also examined the staining reproducibility of each population's MFI and found all of them had a CV of less than 20% (Figure S4).

### 3.6 | Stability of antibody cocktail

As shown in Figure S5 and Table S4, significant changes in the MFI for some fluorochrome antibody combinations were seen as early as 24 h after cocktail preparation. This experiment was repeated twice with similar conclusions. Therefore, we concluded the 27-color cocktail needed to be prepared immediately before staining of samples.

## 4 | DISCUSSION

Acute myeloid leukemia is a biological and clinically heterogeneous disease. Although advances in supportive care and prognostic risk stratification have optimized established therapies, overall long-term survival remains poor. The monitoring of AML MRD by MFC is a prognostically important modality that has proven to be useful when assessing remission status [9–12]. In practice, two approaches have been utilized to evaluate AML MRD by flow cytometry: (i) the LAIP-

**TABLE 1** Assay concordance between 27-color versus 8-color Acute myeloid leukemia measurable residual disease multiparametric flow cytometry panel.

| Cellular subset | Cell percentages (%)[a] | | | | | 95% confidence interval |
|---|---|---|---|---|---|---|
| | #1 | #2 | #3 | #4 | #5 | |
| B cells | | | | | | |
| 27-color[b] | 2.715 | 3.602 | 0.654 | 1.5 | 0.012 | |
| 8-color[c] | 1.346 | 3.202 | 0.419 | 1.265 | 0.047 | |
| Fold change[d] | 2.02 | 1.12 | 1.56 | 1.19 | 0.26 | 0.66–1.8 |
| NK cells | | | | | | |
| 27-color | 6.987 | 4.612 | 4.479 | 3.116 | 0.381 | |
| 8-color | 5.464 | 2.316 | 3.264 | 3.317 | 0.385 | |
| Fold change | 1.28 | 1.99 | 1.37 | 0.94 | 0.99 | 0.95–1.68 |
| CD34+ blasts | | | | | | |
| 27-color | 0.091 | 15.81 | 0.13 | 0.289 | 0.308 | |
| 8-color | 0.196 | 9.598 | 0.203 | 1.195 | 0.522 | |
| Fold change | 0.46 | 1.65 | 0.64 | 0.24 | 0.59 | 0.24–1.19 |
| CD117+ blasts | | | | | | |
| 27-color | 0.08 | 13.774 | 0.162 | 0.105 | 0.295 | |
| 8-color | 0.191 | 9.594 | 0.216 | 0.146 | 0.469 | |
| Fold change | 0.42 | 1.44 | 0.75 | 0.72 | 0.63 | 0.45–1.13 |
| CD34+/CD117+ | | | | | | |
| 27-color | 0.063 | 13.343 | 0.084 | 0.032 | 0.196 | |
| 8-color | 0.070 | 8.976 | 0.076 | 0.023 | 0.227 | |
| Fold change | 0.90 | 1.49 | 1.11 | 1.39 | 0.86 | 0.9–1.4 |
| HLADR+/CD34+/CD117+ | | | | | | |
| 27-color | 0.036 | 0.406 | 0.063 | 0.02 | 0.139 | |
| 8-color | 0.062 | 0.232 | 0.071 | 0.019 | 0.191 | |
| Fold change | 0.58 | 1.75 | 0.89 | 1.05 | 0.73 | 0.6–1.4 |

[a]Total number of enumerated CD45+ cells were used as the denominator for these calculations; five bone marrow samples were evaluated; an average of $1.30 \times 10^6 \pm 0.41 \times 10^6$ cells was acquired for each sample repeat (range: $0.72 \times 10^6$–$2.00 \times 10^6$ cells).
[b]See Table S1 for a description of the antibodies used in the panel.
[c]See Table S2 for a description of antibodies and combination used.
[d]Fold change: calculated by dividing the percentage of cells enumerated using the 27-color panel by the percentage of cells enumerated using the 8-color panel.

based approach where the phenotype of immature blasts is assessed at diagnosis and followed post-therapy and (ii) the DfN approach for which the expression of aberrant antigens on cell surfaces are compared between normal and suspected residual leukemic cells. The ELN MRD Working Party recommends both methods be combined to best detect AML MRD by MFC and for the identification of new aberrancies emerging at follow-up; in this study we used this approach. For this combined method to be clinically useful, however, a sufficiently large panel of antibodies is needed, and ideally an identical panel should be used at diagnosis and follow up. To date, clinical panels measuring AML MRD are typically split into multiple tubes consisting of 8–10 colors, resulting in substantial loss in depth and parametricity, and requiring inferential reasoning for multi-tube interpretation.

Over the last five decades, flow cytometry has evolved from a research technique to a routinely used laboratory tool for the diagnosis, prognosis, and follow-up of hematopoietic neoplasms, immunodeficiency, and a variety of other disorders [30]. The emergence of FSFC and CyTOF have led to a rapid paradigm shift by increasing the number of parameters that can be multiplexed into one single tube, exponentially increasing the depth of information acquired by MFC. In this study, we developed a single-tube 27-color MFC assay for the evaluation of AML MRD by FSFC, incorporating all recommended markers, and compared to our established 8-color panel [18, 31]. The advantages and disadvantages of both methods are illustrated in Table 5. By careful panel design, which required several iterations to best match fluorochromes and antibodies, we were able to achieve a clear separation between negative and positive signals for all antibodies measured. While clear separations between positive and negative populations were achieved, it should be noted the staining intensities of positive signals were lowered and robust standard deviation of negative signals were higher in the fully-stained

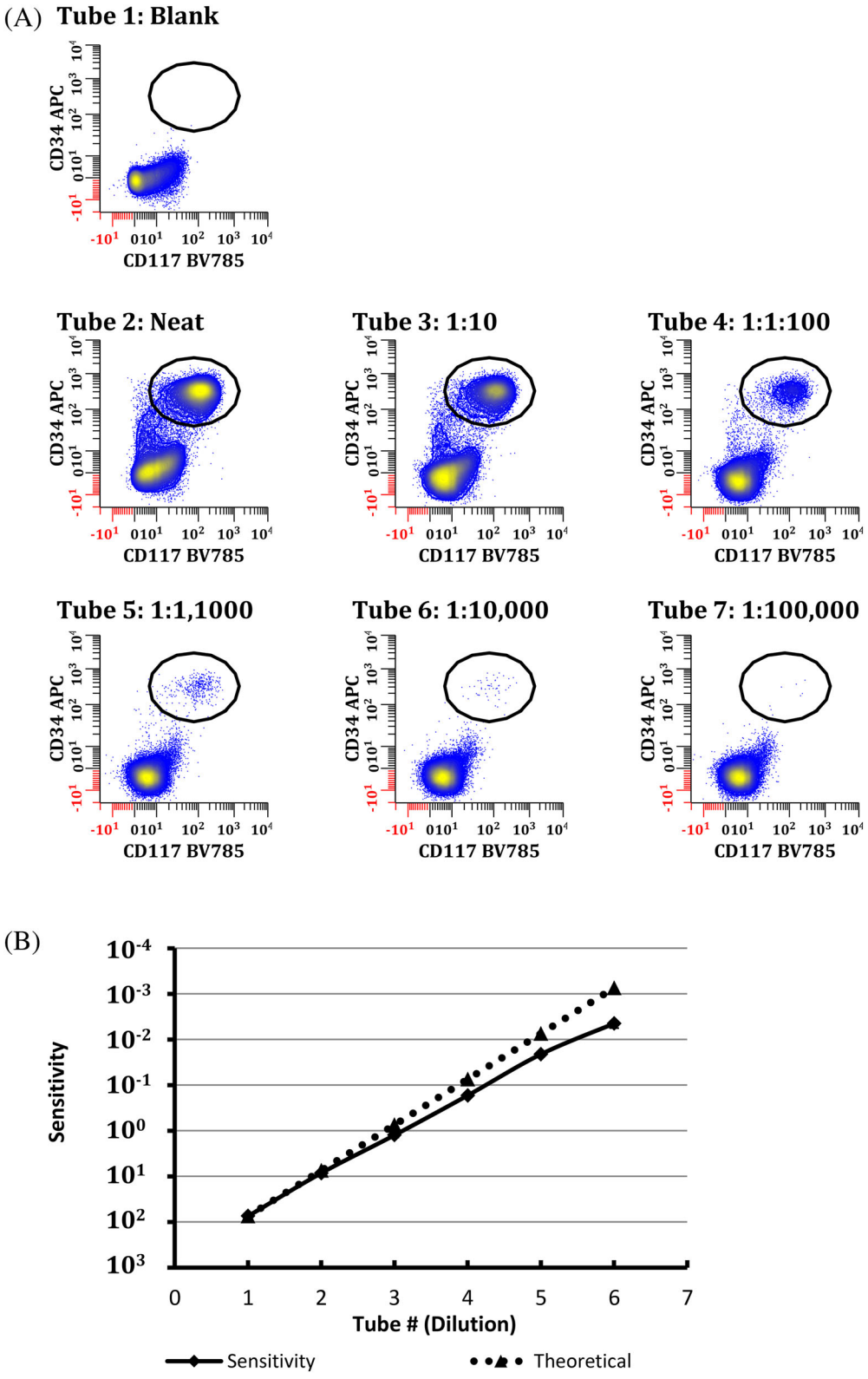


**FIGURE 3** Empirical lower limit of quantification (LLOQ) determination of the 27-color FSFC method for acute myeloid leukemia (AML) measurable residual disease (MRD) evaluation. A bone marrow aspirate from an AML patient was surface stained with the antibodies described in Table S1. This fully stained sample was serially diluted 10-fold in replicate with cells stained with all surface antibodies except CD34 and CD117. The LLOQ was defined as the highest dilution to achieve a CV of less than 30%. A minimum of 1,232,424 events was acquired for each sample (average: 1,595,059 events). The sensitivity of the assay was calculated by dividing the number of events falling into the region used to define CD34, CD117 dual positive myeloblasts by the total CD45 positive leukocytes. (A) Representative sequential dilution dotplots. (B) Plot of dilution sensitivity; results from this study (solid line), theoretical sensitivity (dotted line). Error bars represent the standard deviation of the repeated measurements; the experiment was performed in duplicate using three different patient samples.

samples, corroborating the finding published by Park et al. that the utilization of high number of parameters can indeed compromise signal resolution and thus careful panel design and validation are required [32].

We compared the performance of this novel assay against our established 8-color AML panel using clinical samples from patients with suspected AML MRD. We found high quantitative agreement between both methods. More information could be retrieved using

**TABLE 2** Detection sensitivity of single-tube 27 color assay for the evaluation of Acute myeloid leukemia measurable residual disease.

| | | Number of CD34+/CD117+ blast | | | Percentage of CD34+/CD117+ blast, % | |
|---|---|---|---|---|---|---|
| Tube # | Dilution | Events | Estimated CV (%)[a] | Calculated CV (%) | Percentage (%) | Calculated CV (%) |
| Blank | Blank | 5 | 44.72 | 28.28 | 0.0006 | – |
| 1 | Neat | 601,332 | 0.13 | 4.45 | 74.4709 | 4.97 |
| 2 | $1:10^1$ | 46,731 | 0.46 | 28.23 | 8.4832 | 11.85 |
| 3 | $1:10^2$ | 6034 | 1.29 | 22.59 | 1.2495 | 13.15 |
| 4 | $1:10^3$ | 706 | 3.76 | 29.05 | 0.1685 | 3.28 |
| 5 | $1:10^4$ | 94 | 10.34 | 5.56 | 0.0210 | 3.39 |
| 6 | $1:10^5$ | 24 | 20.63 | 22.11 | 0.0045 | 25.79 |

*Note*: Experiment performed in duplicate using three different patient samples; an average of $1.59 \times 10^6 \pm 0.31 \times 10^6$ cells was acquired for each sample repeat (range: $1.23 \times 10^6$–$2.00 \times 10^6$ cells).

[a]Estimated %CV = square root of the number of CD34+/CD117+ blasts collected divided by the number of blasts.

**TABLE 3** Intra-operator variability.

| | Repeat # | | | | | | | |
|---|---|---|---|---|---|---|---|---|
| Percentage of cell (%) | 1 | 2 | 3 | 4 | 5 | Mean | SD | CV (%) |
| CD3 T cells | 43.98 | 40.71 | 41.42 | 41.03 | 43.07 | 42.04 | 1.41 | 3.35 |
| B cells | 6.91 | 7.01 | 6.68 | 6.82 | 6.71 | 6.83 | 0.14 | 2.05 |
| Hematogones | 2.80 | 3.04 | 2.87 | 3.03 | 2.89 | 2.93 | 0.11 | 3.76 |
| Monocytes | 2.69 | 3.47 | 3.56 | 3.33 | 2.65 | 3.14 | 0.44 | 14.01 |
| CD34+/CD117+ blasts | 25.97 | 25.95 | 25.69 | 25.92 | 25.28 | 25.76 | 0.29 | 1.13 |
| NK cells | 9.63 | 9.52 | 9.62 | 9.77 | 10.29 | 9.77 | 0.31 | 3.17 |

*Note*: Experiment was repeated five times using one patient sample; 50,000 events were collected for each repeat.

our method as opposed to the traditional approach, increasing our confidence in the final interpretation. Presently, most laboratories performing AML MRD by MFC utilize panels recommended by the Bethesda Consensus Group and the ELN [18, 31]. The redundancy of antibodies such as CD34 and CD45 required for multiple tubes results in higher reagents cost. From the perspective of a clinical laboratory, the acquisition of multiple tubes also increases the time needed to stain and acquire the cells, directly increasing assay costs and reducing instrument availability. These issues can be addressed by merging multiple tubes into one.

A disadvantage of the single-tube 27 antibody approach is that the analysis can be more difficult than the traditional 8-color panel. In addition, if a critical antibody such CD34 or CD45 is mistakenly omitted in the 27-color single-tube approach, the analysis and outcome can be severely compromised. Whereas in the multi-tube approach, useful information can often still be retrieved using inferential reasoning. A degree of redundancy across panels can also provide additional certainty and serve as an internal quality check. Furthermore, as the number of analytes required per tube increases, pipetting inaccuracy can also greatly affect the quality of the results. We tested the intra- and inter-operator variability by having technicians independently process and analyze identical clinical samples. We found that a low percent CV was consistently achieved, indicating the assay is highly reproducible within and among technicians. To further improve the assay consistency, we examined the possibility of using a refrigerated antibody cocktail. Unfortunately, we found significant fluctuations over time with the staining performance of the cocktail and thus recommend that it be made just prior to staining until improvements in fluorochrome stability and their interactions are developed.

In this study bone marrow aspirates from patients relapsing from AML MRD were diluted with bone marrow samples from patients with no detectable disease that had been stained using all the antibodies in this panel except CD34 and CD117. The experimentally determined LOD of our assay using this approach was 0.0013%. Not all samples, especially those from patients with myelomonocytic leukemia, would be as easy to identify as in this model system. Nevertheless, this is well below the ELN MRD Working Party threshold recommendation of 0.1% (after excluding debris and CD45 negative cells) that should be achieved for a MFC assessment of AML MRD. The group, however, did acknowledge that levels below 0.1% may still be consistent with residual leukemia, and several studies have shown prognostic significance of MRD levels below 0.1% [33]. About 25% of individuals who achieve an MRD-negative status relapse [34]. One of the reasons can be attributed to the poor quality of interrogated bone marrow samples, for which excessive contamination of peripheral blood can hamper the sensitivity of the flow-based technique to track MRD. Our single-tube 27-color approach provides a solution in two ways. First, the elimination of multiple tubes allows all of the sample

**TABLE 4** Inter-operator variability.

| Cellular subsets[a] | Replicate[b] | | | | Average (%) | SD (%) | CV (%) |
|---|---|---|---|---|---|---|---|
| | Operator 1 | | Operator 2 | | | | |
| | 1 | 2 | 1 | 2 | | | |
| CD3 T cells | | | | | | | |
| Sample #1 | 53.05 | 52.97 | 53.39 | 53.65 | 53.27 | 0.31 | 0.58 |
| Sample #2 | 81.48 | 81.76 | 79.70 | 80.71 | 80.91 | 0.92 | 1.14 |
| Sample #3 | 4.69 | 5.03 | 5.69 | 5.86 | 5.32 | 0.55 | 10.34 |
| Sample #4 | 46.57 | 48.54 | 45.80 | 43.80 | 46.18 | 1.96 | 4.24 |
| B cells | | | | | | | |
| Sample #1 | 0.82 | 0.93 | 0.87 | 0.88 | 0.88 | 0.04 | 4.57 |
| Sample #2 | 1.67 | 1.67 | 1.65 | 1.58 | 1.64 | 0.04 | 2.44 |
| Sample #3 | 0.47 | 0.47 | 0.37 | 0.37 | 0.42 | 0.06 | 14.25 |
| Sample #4 | 1.14 | 1.15 | 1.18 | 1.27 | 1.19 | 0.06 | 5.05 |
| Monocytes | | | | | | | |
| Sample #1 | 2.52 | 2.75 | 2.20 | 2.47 | 2.49 | 0.22 | 8.85 |
| Sample #2 | 3.98 | 3.94 | 4.25 | 4.41 | 4.15 | 0.23 | 5.55 |
| Sample #3 | 3.36 | 2.57 | 2.12 | 2.05 | 2.53 | 0.60 | 23.75 |
| Sample #4 | 32.25 | 31.31 | 33.86 | 34.38 | 32.95 | 1.42 | 4.31 |
| CD34+/CD117+ blasts (MRD level) | | | | | | | |
| Sample #1 | 1.81 | 1.96 | 2.17 | 2.01 | 1.99 | 0.15 | 7.53 |
| Sample #2 | 1.44 | 1.45 | 1.49 | 1.44 | 1.46 | 0.03 | 2.06 |
| Sample #3 | 41.90 | 41.86 | 41.87 | 42.02 | 41.91 | 0.07 | 0.17 |
| Sample #4 | 1.89 | 1.90 | 1.86 | 2.10 | 1.94 | 0.11 | 5.67 |
| NK cells | | | | | | | |
| Sample #1 | 5.54 | 5.42 | 5.21 | 5.24 | 5.35 | 0.15 | 2.80 |
| Sample #2 | 4.81 | 4.87 | 4.84 | 4.58 | 4.78 | 0.13 | 2.72 |
| Sample #3 | 7.86 | 6.93 | 6.55 | 6.61 | 6.99 | 0.60 | 8.59 |
| Sample #4 | 5.01 | 5.15 | 5.09 | 5.12 | 5.09 | 0.06 | 1.18 |

[a]Four acute myeloid leukemia samples were used; one with overt disease and three with measurable residual disease.
[b]An average of $1.33 \times 10^6 \pm 0.38 \times 10^6$ cells was acquired for each sample repeat (range: $0.97 \times 10^6$–$2.00 \times 10^6$ cells).

be dedicated to a single tube, increasing the likelihood that enough events can be collected to achieve at least a 0.1% LOD, and if desired, a higher number of cells can be collected to improve detection sensitivity. Secondly, the degree of hemodilution can be assessed by incorporating markers used for defining immune cells that should only be found in bone marrow. In this regard, the presence of mast cells (bright for CD117) and hematogones (dim for CD45, CD38, CD10 and positive for CD19), and the ratio of immature/mature neutrophils based on CD16 intensity can be used [35, 36]. This is not easily achievable in traditional 8–10 color methods without adding additional tubes. Regardless, we recommend a separate study be conducted to standardize cut-off values for indicators of hemodilution used to assess sample adequacy.

Taken together, we propose that our single-tube 27 color assay is a suitable alternative to traditional multi-tube approaches for assessing AML MRD by MFC. This method is reproducible, sensitive, and will theoretically permit the direct identification and appreciation of the immunophenotypic drift often seen in relapsed AML MRD. The developmental works described in this manuscript should serve as a template for future validation efforts required for implementation in a clinical setting. To completely validate the assay, a higher number of AML MRD positive and negative samples need to be tested and correlated with the predicate assay. This will help generate a reference library defining normal antigen expression patterns and those seen in patients receiving treatment. For establishing detection sensitivity, investigators should consider using normal or staging bone marrow as the dilution matrix for generating LOB. Furthermore, the longevity of antibody cocktails should be tested as stable fluorochromes are developed and dried-down technologies become more mature in the future. This will greatly improve turnaround times by enabling faster sample processing and reduce overhead costs.

**TABLE 5** Comparison between new 27-color and traditional 8-color acute myeloid leukemia measurable residual disease assays.

| | 27-Color assay | 8-Color assay |
|---|---|---|
| Number of tubes required for staining, acquisition, and analysis | One tube | Three or more tubes |
| Duplication of reagents (i.e., CD45, CD34, etc.) | Unnecessary | Typically required for gating and correlation among tubes |
| Simultaneous assessment of antigens | All antigens are correlated | Inferential reasoning is required to correlate information generated from multiple tubes |
| Reproducibility across tubes | Not possible | Possible with duplicated antigens |
| Cell requirements | $1 \times 10^6$ cells | $\geq 3 \times 10^6$ cells |
| Incorporation and evaluation of new target antigens | Possible, assuming detection channel is available | Difficult, a new tube needs to be developed and added to the others |
| Cocktailing of reagents | Not currently practical | Cocktails stable for hours to weeks depending on fluorochrome choices |

Traditionally, an analyst must refer to bivariate data plots generated from multiple 8–12 color tubes and assumptions, or inferential reasoning must be applied to decide the final phenotype of the abnormal blast population. Our 27-color panel circumvents this issue by simultaneously assessing all markers, potentially increasing analyst's confidence in recognizing abnormal blasts. It also provides the flexibility to incorporate newer markers including those that are currently targeted by therapy. With the development of supervised and automated analysis programs that offer superior visualization options for high parameter flow cytometric data, such as Flow Self Organizing Maps (FlowSOM), Gemstones, and Uniform Manifold Approximation and Projection (UMAP) for dimension reduction, we anticipate this panel will provide useful information to facilitate clinical interpretation of the flow cytometry data and help identify new, targetable antigens.

## AUTHOR CONTRIBUTIONS

**Kah Teong Soh:** Conceptualization (equal); data curation (lead); formal analysis (lead); investigation (lead); methodology (lead); project administration (lead); visualization (lead); writing – original draft (lead); writing – review and editing (lead). **Alexis Conway:** Conceptualization (equal); investigation (equal); validation (equal). **Xiao Jun Liu:** Investigation (equal); validation (equal). **Paul K. Wallace:** Conceptualization (lead); funding acquisition (lead); project administration (supporting); resources (lead); software (lead); supervision (supporting); validation (supporting); visualization (supporting); writing – original draft (supporting); writing – review and editing (lead).

## ACKNOWLEDGMENTS

Flow cytometry services were provided by the Flow and Image Cytometry Resource Facility at the Roswell Park Comprehensive Cancer Center, which is supported in part by the NCI Cancer Center Support Grant 5P30 CA016056. The authors wish to gratefully acknowledge the time and efforts of Edward Podniesinski who first introduced us to spectral flow cytometry nearly 18 years ago and maintained this and all our equipment to the highest standards.

## CONFLICT OF INTEREST

The authors declare no conflict of interest.

## PEER REVIEW

The peer review history for this article is available at https://publons.com/publon/10.1002/cyto.a.24667.

## ORCID

*Kah Teong Soh* https://orcid.org/0000-0002-0146-0485

## REFERENCES

1. Swerdlow SH, Campo E, Harris NL, Jaffe ES, Pileri SA, Stein H, Thiele J, Vardiman JW, editors. WHO Classification of Tumours of Haematopoietic and Lymphoid Tissues. Geneva, Switzerland: WHO Press; 2008. p. 885-7.
2. Papaemmanuil E, Gerstung M, Bullinger L, Gaidzik VI, Paschka P, Roberts ND, et al. Genomic classification and prognosis in acute myeloid leukemia. N Engl J Med. 2016;374:2209–21.
3. Ley TJ, Miller C, Ding L, Raphael BJ, Mungall AJ, Robertson A, et al. Genomic and epigenomic landscapes of adult de novo acute myeloid leukemia. N Engl J Med. 2013;368:2059–74.
4. Rajwa B, Wallace PK, Griffiths EA, Dundar M. Automated assessment of disease progression in acute myeloid leukemia by probabilistic analysis of flow cytometry data. IEEE Trans Biomed Eng. 2017;64:1089–98.
5. Meyers J, Yu Y, Kaye JA, Davis KL. Medicare fee-for-service enrollees with primary acute myeloid leukemia: an analysis of treatment patterns, survival, and healthcare resource utilization and costs. Appl Health Econ Health Policy. 2013;11:275–86.
6. Terwijn M, van Putten WL, Kelder A, van der Velden VH, Brooimans RA, Pabst T, et al. High prognostic impact of flow cytometric minimal residual disease detection in acute myeloid leukemia: data from the HOVON/SAKK AML 42A study. J Clin Oncol. 2013;31:3889–97.
7. Walter RB, Othus M, Burnett AK, Löwenberg B, Kantarjian HM, Ossenkoppele GJ, et al. Resistance prediction in AML: analysis of 4601 patients from MRC/NCRI, HOVON/SAKK, SWOG and MD Anderson Cancer Center. Leukemia. 2015;29:312–20.
8. Döhner H, Weisdorf DJ, Bloomfield CD. Acute myeloid leukemia. N Engl J Med. 2015;373:1136–52.
9. Paiva B, Vidriales MB, Sempere A, Tarín F, Colado E, Benavente C, et al. Impact of measurable residual disease by decentralized flow cytometry: a PETHEMA real-world study in 1076 patients with acute myeloid leukemia. Leukemia. 2021;35:2358–70.
10. Cherian S, Soma LA. How I diagnose minimal/measurable residual disease in B lymphoblastic leukemia/lymphoma by flow cytometry. Am J Clin Pathol. 2021;155:38–54.
11. Vega-García N, Perez-Jaume S, Esperanza-Cebollada E, Vicente-Garcés C, Torrebadell M, Jiménez-Velasco A, et al. Measurable residual disease assessed by flow-cytometry is a stable prognostic factor for pediatric T-cell acute lymphoblastic leukemia in consecutive

SEHOP protocols whereas the impact of oncogenetics depends on treatment. Front Pediatr. 2021;8:614521.
12. Dix C, Lo T-H, Clark G, Abadir E. Measurable residual disease in acute myeloid leukemia using flow cytometry: a review of where we are and where we are going. J Clin Med. 2020;9:1714.
13. Inaba H, Coustan-Smith E, Cao X, Pounds SB, Shurtleff SA, Wang KY, et al. Comparative analysis of different approaches to measure treatment response in acute myeloid leukemia. J Clin Oncol. 2012;30: 3625–32.
14. Al-Mawali A, Gillis D, Hissaria P, Lewis I. Incidence, sensitivity, and specificity of leukemia-associated phenotypes in acute myeloid leukemia using specific five-color multiparameter flow cytometry. Am J Clin Pathol. 2008;129:934–45.
15. Chen X, Cherian S. Role of minimal residual disease testing in acute myeloid leukemia. Clin Lab Med. 2021;41:467–83.
16. Short NJ, Zhou S, Fu C, Berry DA, Walter RB, Freeman SD, et al. Association of Measurable Residual Disease with Survival Outcomes in patients with acute myeloid leukemia: a systematic review and meta-analysis. JAMA Oncol. 2020;6:1890–9.
17. Maiti A, DiNardo CD, Wang SA, Jorgensen J, Kadia TM, Daver NG, et al. Prognostic value of measurable residual disease after venetoclax and decitabine in acute myeloid leukemia. Blood Adv. 2021;5: 1876–83.
18. Schuurhuis GJ, Heuser M, Freeman S, Béné M-C, Buccisano F, Cloos J, et al. Minimal/measurable residual disease in AML: a consensus document from the European LeukemiaNet MRD working party. Blood. 2018;131:1275–91.
19. Hanekamp D, Bachas C, van de Loosdrecht A, Ossenkoppele G, Cloos J. Re: Myeloblasts in normal bone marrows expressing leukaemia-associated immunophenotypes. Pathology. 2020;52: 289–91.
20. Wood BL. Acute myeloid leukemia minimal residual disease detection: the difference from normal approach. Curr Protoc Cytom. 2020; 93:e73.
21. Barone SM, Paul AGA, Muehling LM, Lannigan JA, Kwok WW, Turner RB, et al. Unsupervised machine learning reveals key immune cell subsets in COVID-19, rhinovirus infection, and cancer therapy. bioRxiv. 2020.
22. Ferrer-Font L, Pellefigues C, Mayer JU, Small SJ, Jaimes MC, Price KM. Panel design and optimization for high-dimensional Immunophenotyping assays using spectral flow cytometry. Curr Protoc Cytom. 2020;92:e70.
23. He SZ, Busfield S, Ritchie DS, Hertzberg MS, Durrant S, Lewis ID, et al. A phase 1 study of the safety, pharmacokinetics and antileukemic activity of the anti-CD123 monoclonal antibody CSL360 in relapsed, refractory or high-risk acute myeloid leukemia. Leuk Lymphoma. 2015;56:1406–15.
24. van Loo PF, Hangalapura BN, Thordardottir S, Gibbins JD, Veninga H, Hendriks LJA, et al. MCLA-117, a CLEC12AxCD3 bispecific antibody targeting a leukaemic stem cell antigen, induces T cell-mediated AML blast lysis. Expert Opin Biol Ther. 2019;19:721–33.
25. Matos DM. Steric hindrance: a practical (and frequently forgotten) problem in flow cytometry. Cytometry B: Clin Cytom. 2021;100: 397–401.
26. Johansson U, Macey M. Tandem dyes: stability in cocktails and compensation considerations. Cytometry B: Clin Cytom. 2014;86: 164–74.
27. Hulspas R, Dombkowski D, Preffer F, Douglas D, Kildew-Shah B, Gilbert J. Flow cytometry and the stability of phycoerythrin-tandem dye conjugates. Cytometry A. 2009;75:966–72.
28. Tario JD, Wallace PK. Reagents and cell staining for immunophenotyping by flow cytometry. In: McManus LM, Mitchell RN, editors. Pathobiology of human disease. San Diego: Elsevier; 2014. p. 3678–701.
29. Litwin V, Oldaker T, Afonina E, Bakke AC, Barnett D, Cleary JM, et al. Validation assays performed by flow cytometry. CLSI Guidelines. 1st ed. Malvern, Pennsylvania: Clinical Laboratory Standard Institute; 2021.
30. Jaye DL, Bray RA, Gebel HM, Harris WA, Waller EK. Translational applications of flow cytometry in clinical practice. J Immunol. 2012; 188:4715–9.
31. Wood BL, Arroz M, Barnett D, DiGiuseppe J, Greig B, Kussick SJ, et al. 2006 Bethesda international consensus recommendations on the immunophenotypic analysis of hematolymphoid neoplasia by flow cytometry: optimal reagents and reporting for the flow cytometric diagnosis of hematopoietic neoplasia. Cytometry B: Clin Cytom. 2007;72(Suppl 1):S14–22.
32. Park LM, Lannigan J, Jaimes MC. OMIP-069: forty-color full Spectrum flow cytometry panel for deep Immunophenotyping of major cell subsets in human peripheral blood. Cytometry A. 2020;97:1044–51.
33. Maclachlan KH, Came N, Diamond B, Roshal M, Ho C, Thoren K, et al. Minimal residual disease in multiple myeloma: defining the role of next generation sequencing and flow cytometry in routine diagnostic use. Pathology. 2021;53:385–99.
34. Paietta E. Consensus on MRD in AML? Blood. 2018;131:1265–6.
35. Mendonça de Pontes R, Flores-Montero J, Sanoja-Flores L, Puig N, Pessoa de Magalhães RJ, Corral-Mateos A, et al. B-cell regeneration profile and minimal residual disease status in bone marrow of treated multiple myeloma patients. Cancer. 2021;13:1704.
36. Loken MR, Chu S-C, Fritschle W, Kalnoski M, Wells DA. Normalization of bone marrow aspirates for hemodilution in flow cytometric analyses. Cytometry B: Clin Cytom. 2009;76B:27–36.

## SUPPORTING INFORMATION

Additional supporting information can be found online in the Supporting Information section at the end of this article.

Received: 29 September 2021 | Revised: 11 January 2022 | Accepted: 7 February 2022

DOI: 10.1002/cyto.a.24543

ORIGINAL ARTICLE

MIFlowCyt

ISAC INTERNATIONAL SOCIETY FOR ADVANCEMENT OF CYTOMETRY

CYTOMETRY Journal of Quantitative Cell Science PART A

# Barcoding of live peripheral blood mononuclear cells to assess immune cell phenotypes using full spectrum flow cytometry

**Fabian Junker** | **Priscila Camillo Teixeira**

Roche Pharma Research and Early Development, Pharmaceutical Sciences, Roche Innovation Center Basel, F. Hoffmann-La Roche Ltd., Basel, Switzerland

**Correspondence**
Fabian Junker, Roche Pharma Research and Early Development, Pharmaceutical Sciences, Roche Innovation Center Basel, F. Hoffmann-La Roche Ltd.,Grenzacherstrasse 124, 4070 Basel, Switzerland.
Email: fabian.junker@roche.com; fabian.r.junker@gmail.com

## Abstract

Barcoded flow cytometry is a multiplexing technique allowing for the simultaneous acquisition of cells from different donors or experimental conditions in a high-throughput manner. This approach allows to synchronize acquisition of samples and reduce variance introduced through the operator or technical platform. However, to date, only very few flow cytometry barcoding protocols have been developed, which often suffer from technical limitations. Here, we developed a novel barcoding protocol for a full-spectrum flow cytometry platform. We developed a 21-color immunophenotyping assay for up to 20 different samples analyzed simultaneously with comparable variance between repeated single-tube acquisition and postde-multiplexing. Barcoding offers great potential in parallelizing the analysis of complex cell populations such as peripheral blood mononuclear cells (PBMCs). Consequently, we assessed the performance of our method in situations where PBMCs were challenged with phytohaemagglutinin (PHA), a strong mitogen and broad activator of B cells and T cells, and superantigen *Staphylococcus* enterotoxin B (SEB) that has been reported to induce polyclonal T cell activation. PBMCs were either barcoded before pooled challenge or challenged individually pre-barcoding. Our final workflow included pooled immunophenotyping followed by machine learning aided single-cell data analysis and enabled us to identify robust PHA and SEB mode of action related phenotypic changes in PBMC immune cell lineages. Conclusively, we present a novel technique allowing the barcoded acquisition and analysis of PBMCs from up to 20 different donors and present a valid basis for the future development of complex immunophenotyping protocols.

## 1 | INTRODUCTION

With the increasingly routine use of high-parameter flow cytometry, complex immunophenotyping protocols have been designed which allow for hitherto unparalleled complexity in immune cell characterization of both lymphoid and myeloid lineages [1–5]. With the introduction of full spectrum flow cytometry, panels encompassing 40 and more parameters have been described for the in-depth characterization of peripheral blood mononuclear cell (PBMC) lineages [6–8]. Previously, such granularity could only be achieved by cytometry by time of flight (CyTOF) protocols which employ heavy metals and mass detectors for cell analysis [9]. As a consequence, the reporting of potentially well over several hundred results per experiment becomes possible. This means that flow cytometry data analysis is becoming more and more difficult and dependent on machine learning algorithms to make sense of the vast amount of single-cell information retrieved [10–12]. Importantly, high-parameter immunophenotyping protocols with the assessment of highly complex cell lineages with different abundances make best practice staining and sample preparation procedures critically important to minimize operator- and platform-induced analysis bias [13]. This is critical in longitudinal sample analysis, for instance in bioanalytical [14] or pharmacodynamics

 

(PD) biomarker development in clinical trials [15]. Here, the same patient's immune cells need to be monitored repeatedly over a long period. Even in a batch analysis situation, for instance with frozen PBMC samples, optimal staining efficiency through the use of identical flow cytometry master mixes and well aligned controls (such as fluorescence-minus one, FMO, or fluorescence-minus many controls, FMx) are essential.

Some of these challenges can be mitigated by employing multiplexing strategies, which allow for the simultaneous acquisition of samples, for instance from several donors or several analysis time points. This has the potential to greatly reduce operator- and platform-induced bias, maximize assay efficacy through the use of identical staining mixes and may also lead to reduced overall antibody consumption. The CyTOF community has been a pioneer in the field by developing routine and reliable barcoding protocols. A frequently used approach relies on barcoding individual (live or fixed) PBMC samples with a unique combination of anti-CD45 antibodies [16–19] or other constitutively expressed cell surface markers such as CD298 and beta-2-microglobulin [20]. Through combinatorial mathematics, many samples can thus be acquired at the same time [21]. For example, if seven anti-CD45 antibodies are available for barcoding, three of which are used to co-label PBMCs of one specific donor/condition, this allows for up to 35 unique barcoding combinations ("7-choose-3"). De-barcoding then happens either manually through Boolean gating or through the use of specialized cytometry analysis scripts or software [22–24]. However, CyTOF is far less routinely accessible to the immunology community than flow cytometry due to higher cost, challenging reagent preparation protocols and potential unavailability of experienced operators especially in the clinical PD biomarker setting. In addition, fluorescence-based flow cytometry allows for the analysis of live PBMCs with potential subsequent cell sorting.

In the past, several multiplexing protocols for use in conventional flow cytometry have been proposed. A frequently used strategy relies on the serial dilution of label retaining intracellular dyes [25–27]. Conceptually, this may have several limitations since only few serial dilutions are feasible per dye, some dyes may spill into other cells and finally, cells with different autofluorescent properties or highly differential cytoplasmic complexity may not resolve correctly [28]. Some of these limitations have been addressed using succininidyl ester-based dyes, which covalently label intracellular proteins. This allows for multiplexed analysis of up to n = 96 PBMC- or cell-line-derived specimens [24, 25, 29, 30] in parallel using up to three intracellular dyes. Typical applications include, for instance, combined low-parameter immunophenotyping [29] or timed phosphor-protein signaling studies [24]. Critically, these protocols require prior cell fixation and / or magnetic cell sorting and so far have not been combined with high-parameter immunophenotyping. A further conceptual limitation may be that intracellular proteins are covalently labeled with fluorescent dyes, which may in theory impact the staining efficiency of certain detection antibodies. Antibody-tagged barcoding protocols have also been introduced for polychromatic flow cytometers. They combine cell lineage antibodies (such as anti-CD4 or anti-CD8) tagged to different fluorochromes [31]. However, these strategies only allow for the discrimination of select cell lineages in a multiplexed manner thus potentially missing other sample specific information [31]. In addition, complex barcoding protocols using conventional polychromatic flow cytometers with a limited number of detectors might suffer from spreading error (SE) affecting de-barcoding [8, 32].

A possible technological improvement is full spectrum flow cytometry, where many fluorochromes can be analyzed simultaneously due to enhanced spectral fluorochrome unmixing thus potentially reducing SE [33]. We were intrigued by the potential of live-PBMC barcoding on a full spectrum flow cytometer using anti-CD45 tagging based barcoding protocols as pioneered by CyTOF. In the present study, we sought to develop a novel barcoding protocol employing CD45-mediated fluorochrome tagging, followed by a subsequent immunophenotyping protocol. We assessed different CD45 barcoding combinations eventually resulting in a 6-choose-3 approach for the simultaneous analysis of up to 20 individual PBMC samples. During its establishment, we assessed assay parameters such as barcode-induced artifacts and individual sample debarcoding efficiency as well as potential batch effects and compared the precision of multiplexed samples to sequentially acquired samples on the same cytometer. An application of our protocol could be the assessment of complex immunophenotypes at the population level in PD biomarker development or mode of action (MoA) studies in the development of immunomodulators. Examples include phytohaemagglutinin (PHA) [34] and *Staphylococcus* enterotoxin B (SEB) mediated PBMC activation. While PHA, a lectin, is a broader PBMC activator with strong effects on T cells that has also occasionally been reported to affect B cell activation [35–37], SEB is a more selective T cell activator [38]. PHA is often used as a mitogen, while SEB has been studied with regards to $CD4^+$ T cell activation and the release of pro-inflammatory cytokines. However, both in vitro stimuli lack exhaustive characterization of activation-induced phenotypic changes. Consequently, we assessed the performance of our barcoding and immunophenotyping protocol in combination with dimensionality reduction (optSNE; t-stochastic neighbor embedding) [39] and automated clustering (FlowSOM) approaches. We first designed an experiment where previously barcoded PBMCs from n = 10 donors were pooled and simultaneously challenged with PHA revealing broad changes to the abundance of immune cell subsets. Finally, by challenging PBMCs from n = 20 donors separately with SEB, we assessed T cell activation in detail identifying MoA related changes in the abundance of specific T cell subsets [40].

## 2 | MATERIALS AND METHODS

### 2.1 | Ethics statement

Human blood samples from healthy volunteers were collected under the Blood Donation for Research Purposes program at F. Hoffmann-La Roche, Basel, Switzerland.

ISAC CYTOMETRY Journal of Quantitative Cell Science PART A

## 2.2 | Preparation of PBMCs from healthy donor blood

As described previously [41], healthy donor blood was collected in sodium heparin (NaHep) tubes (BD), diluted with PBS (Gibco, 1:1) and transferred to Leucosep tubes (Greiner Bio-One) pre-filled with Ficoll-Paque Plus (GE Healthcare). Tubes were centrifuged without brake (1000 g, 10 min, RT). Nonsedimented leukocytes were transferred to a fresh 50 ml tube (Falcon) and washed twice with PBS. PBMCs were routinely cultured at 37°C in R-10 medium (RPMI 1640, ATCC modification (Gibco), + 1% (v/V) penicillin/streptomycin (Thermo Fisher) and 10% (v/V) FBS (Life Technologies)).

## 2.3 | Flow cytometry equipment and routine analysis

Unless stated otherwise, the following cytometer was used for multiplexing experiments: Cytek Aurora, 4 L (355 nm, 405 nm, 488 nm and 640 nm), 16UV, 16 V, 14B, 8R. Single-stain control samples for unmixing were obtained by pooling PBMCs from several donors where applicable including CD3-CD28 spiked controls (48 h incubation) for activation markers. Postacquisition, per tube, individual samples were de-multiplexed through Boolean gating. The following gating strategy was applied (here: sample labeled with CD45-FITC and CD45-PE, 5-choose-2 approach): Sample = CD45-FITC$^+$ AND CD45-PE$^+$ NOT CD45-BUV395$^+$ NOT CD45-BV570$^+$ NOT CD45-AF532$^+$ etc. PBMC centrifugation was always done at 400 g at room temperature for 4 min.

## 2.4 | Multiplexing live PBMCs

### 2.4.1 | Comparing single acquisition of PBMCs with barcoded acquisition of n = 10 replicates (5-choose-2)

The 2.5 × 10$^6$ PBMCs from n = 3 healthy donors were prepared of which 10× 250,000 PBMCs were transferred to individual 5 ml round-bottom tubes (Falcon) and washed 1× with 1 ml of PBS for CD45 barcoding. We used a 5-choose-2 approach to label 10 individual PBMC replicates per donor (see supplementary methods). In addition, all PBMCs were labeled with a common CD45 antibody (CD45-AF532). PBMCs were incubated in 50 μL of barcoding mix (PBS + 10% (v/V) Brilliant Stain Buffer (BD Biosciences), see supplementary methods) for 25 min at 4°C. Alternatively, n = 3 tubes of PBMCs /donor were prepared for individual analysis (no multiplexing); these cells were exclusively labeled with CD45-AF532. All cells were then washed 2× with 1 ml of PBS. Barcoded cells were resuspended in 100 μL of PBS. All cells (barcoded or nonbarcoded) were then incubated with the immunophenotyping mix (100 μL for single-sample tubes, 500 μL for barcoded and pooled samples): CD3-BV711, CD4-BUV805, CD8-BUV737, CD19-PECy5, CD56-APC-R700, CD14-PEDazzle594, CD25-APC, CD127-PE, CD197-PE-Cy7, CD45RA-BV510, PD-1-BV421. The master mix contained PBS + 10% (v/V) Brilliant Stain Buffer +10% (v/V) FcR Blocking Reagent, human (Miltenyi). Cells were incubated at 4°C for 30 min, then washed 2× with 2 ml of PBS, resuspended in 500 μL of PBS and analyzed at the cytometer. Replicate stains were then compared to n = 3 individually stained samples for variance and overall resolution.

### 2.4.2 | Assessing CD45 barcoding mediated batch effects

The 250,000 PBMCs from n = 3 healthy donors (A, B, and C) were transferred to individual 5 ml round-bottom tubes and washed 1× with 1 ml of PBS for CD45 barcoding using a 5-choose-2 approach to label 9 PBMC replicates per donor. In addition, all PBMCs were labeled with a common CD45 antibody (CD45-AF532). PBMCs were incubated in 50 μL of barcoding mix (PBS + 10% (v/V) Brilliant Stain Buffer, see supplementary methods) for 25 min at 4°C. Cells were then washed 2× with 1 ml of PBS and resuspended in 100 μL of PBS and split in two tubes per replicate. Subsequently, n = 9 samples from donors A, B and C were then pooled as follows: Tube 1, samples A1 B2 C3 A4 B5 C6 A7 B8 C9; tube 2, samples B1 C2 A3 B4 C5 A6 B7 C8 A9; tube 3, samples C1 A2 B3 C4 A5 B6 C7 A8 B9. This resulted in n = 3 tubes (per FM control vs. full immunophenotyping stain) with barcoded cells, which were sedimented and incubated with 500 μL immunophenotyping master mix containing either the lineage cocktail only (for FM controls: CD3-Bv711, CD4-BUV805, CD8-BUV737, CD19-PECy5, CD56-APC-R700, CD14-PE-Dazzle594, CD25-APC, CD127-PE, CD197-PE-Cy7, CD45RA-BV510, HLA-DR-BUV496) or the lineage cocktail plus activation markers (PD-1-BV421, LAG3-BV785, CD103-BV650). The master mix contained PBS + 10% (v/V) Brilliant Stain Buffer +10%(v/V) FcR Blocking Reagent. Cells were incubated at 4°C for 30 min, then washed 2× with 2 ml of PBS, resuspended in 500 μL of PBS and analyzed at the cytometer. Both the tube effect as well as the donor effect on resolution and variance were assessed.

### 2.4.3 | Challenging barcoded PBMCs from n = 10 different donors with PHA

For the comparison of pooled naïve and activated barcoded PBMCs, 2 × 10$^6$ PBMCs from n = 10 healthy donors were barcoded in a donor-specific way in a 5 ml tube on ice for 25 min with a 5-choose-2 approach in 100 μL of barcoding mix (PBS + 10%(v/V) Brilliant Stain Buffer, see supplementary methods). Barcoded cells were then washed twice with 2 ml of PBS, resuspended in 1 ml of R-10 per donor, pooled and split in 2 x 5 ml batches which were subsequently seeded in a 6-well cell culture plate (Falcon). One fraction was subsequently challenged with phytohaemagglutinin (PHA, 2 μg/ml; ThermoFisher, #R30852801). After 48 h in culture, pooled PBMCs (naïve or challenged) were washed 2× with 10 ml of PBS in a 50 ml tube and again transferred in two fractions per initial treatment condition (FMx

vs. full stain) to 5 ml tubes. For flow cytometric analysis, the previously barcoded cells were incubated with 500 μL immunophenotyping master mix containing either the lineage cocktail only (for fluorescence-minus many [FMx] controls: live-dead UV blue; CD56-APC-R700, CD14-AF647, CD19-FITC, CD3-V450, CD197-PE-Cy7, CD25-APC, CD127-APC-Cy7, CD45RA-BV510, CD8-BUV496, CD4-BUV805, CD28-BUV563) or the lineage cocktail plus activation markers (CD223-PE-CF594, CD103 BV480, CD279-BV650, CD137-BV711, CD39-BV750, CD366-BV786, CD278-BUV661, CD154-BV421). The master mix contained PBS + 10% (v/V) Brilliant Stain Buffer +10% (v/V) FcR Blocking Reagent. Cells were incubated at 4°C for 30 min, washed 2× with 2 ml of PBS, resuspended in 300 μL of PBS and analyzed at the cytometer (here: Cytek Aurora, 5 L, 355 nm, 405 nm, 488 nm, 561 nm and 640 nm).

#### 2.4.4 | Assessing PBMCs from n = 20 different donors post-SEB challenge

Per condition, 250,000 PBMCs from n = 20 healthy donors were prepared and cultured in 24-well plates (Falcon, 1 ml of R-10 medium) in vitro for 48 h either naïve or with SEB (Sigma, 1.0 μg/ml). Subsequently, cells were transferred to individual 5 ml round-bottom tubes and washed 1× with 1 ml of PBS for subsequent CD45 barcoding. We used a 6-choose-3 approach. Individual naïve and activated PBMCs from the same donor received the same barcode in separate tubes (see supplementary methods) and were incubated in 50 μL of barcoding mix (PBS + 10% (v/V) Brilliant Stain Buffer) for 25 min at 4°C. Cells were then washed 2× with 1 ml of PBS, resuspended in 100 μL of PBS and split in two tubes per treatment condition (two tubes/donor activated, two tubes/donor treatment naïve). Samples from all 20 donors were then pooled accordingly resulting in four tubes with barcoded cells, which were sedimented and incubated with 500 μL immunophenotyping master mix as described above containing either the lineage cocktail only (FMx) or the lineage cocktail plus activation markers (full stain). The only exception to the PHA challenge experiment is that we swapped CD19-FITC with CD19-BUV737 and included CD134-BV605 (full master mix only). Cells were incubated at 4°C for 30 min, then washed 2× with 2 ml of PBS, resuspended in 500 μL of PBS and analyzed at the cytometer.

### 2.5 | Flow cytometry gating and analysis of FCS files (manual gating, optSNE and FlowSOM) and statistical considerations

FCS files were exported using Spectro Flow (Cytek) and analyzed in FlowJo (BD) for single-cells (FSC-A vs. FSC-H), where applicable live (live-dead$^-$), CD45$^+$. Single samples were extracted using the Boolean de-unmixing strategy as defined above. For further analysis including manual gating, data clustering and dimensionality analyses, Omiq (Omiq, Inc., Santa Clara, SA; www.omiq.ai) was applied for individual datasets. Corresponding FCS files were de-barcoded as described above. The following parameters were used for optSNE dimensionality reduction on concatenations of 10,000 events/sample: Max iterations = 1000, optSNE end = 5000, perplexity = 30, theta = 0.5, random seed = 123, verbosity = 25. The following parameters were used for FlowSOM clustering: xdim / ydim = 10, rlen = 10, consensus metaclustering on k = 14, 17 and 20; random seed = 123. For analyses of the results obtained in Omiq, a custom R (version 4.1) script was written. Graphs were generated using *ggplot 2*. Where applicable, paired PBMC samples were analyzed using paired t-tests with corrections for multiple testing (BH) using the R *rstatix* package. The coefficient of variation (CV) was calculated as follows: CV = (SD/$\bar{x}$) * 100, whereby $\bar{x}$ = mean result of median fluorescence intensity (MFI) or abundance (%) of a population, SD = standard deviation of the individual result. CVs ≤20% were considered acceptable.

### 2.6 | Flow cytometry data repository

Data are publicly available at the FlowRepository (ID: FR-FCM-Z4KK), URL: https://flowrepository.org/id/FR-FCM-Z4KK.

## 3 | RESULTS

### 3.1 | Anti-CD45 barcoding does not introduce major batch effects and allows for the analysis of complex live PBMCs populations

We reasoned that the multiplexed analysis of human leukocyte subsets would best work in a human PBMC setting, for which this approach is routinely used in mass cytometry (CyTOF) [42]. Given limited number of fluorochromes sufficiently different in their emission and excitation spectra and the number of matching detectors available on current high-end flow cytometers, we reasoned that a 5-choose-2 (max. 10 individual samples) or 6-choose-3 (max. 20 individual samples) barcoding approach would allow for the simultaneous acquisition of a useful amount of individual samples while still facilitating complex immunophenotyping. For an initial experiment, we sought to develop a 10-plex barcoding panel for the Cytek Aurora using a 5-choose-2 approach followed by an 11-color immunophenotyping panel (Figure 1A and Supplementary Figure 1A). In this experiment, we assessed how PBMC lineages as well as T cell subsets from the same donor would compare in repeatedly acquired identical single-stains (*unicates*, serial acquisition of individually stained PBMCs in individual tubes) versus 10 simultaneously acquired barcoded samples (barcoded *replicates* pooled in one tube). Freshly prepared PBMCs where either split into three tubes and labeled with a common single anti-CD45 antibody followed by the immunophenotyping panel, or first labeled with unique barcodes (n = 10), mixed, and then incubated with the common immunophenotyping master mix in one tube postpooling (Figure 1A). After debarcoding, samples were compared to the individually stained samples with regards to cell lineages comparability. Sample debarcoding efficiency was highly comparable (average efficiency

ISAC CYTOMETRY Journal of Quantitative Cell Science PART A

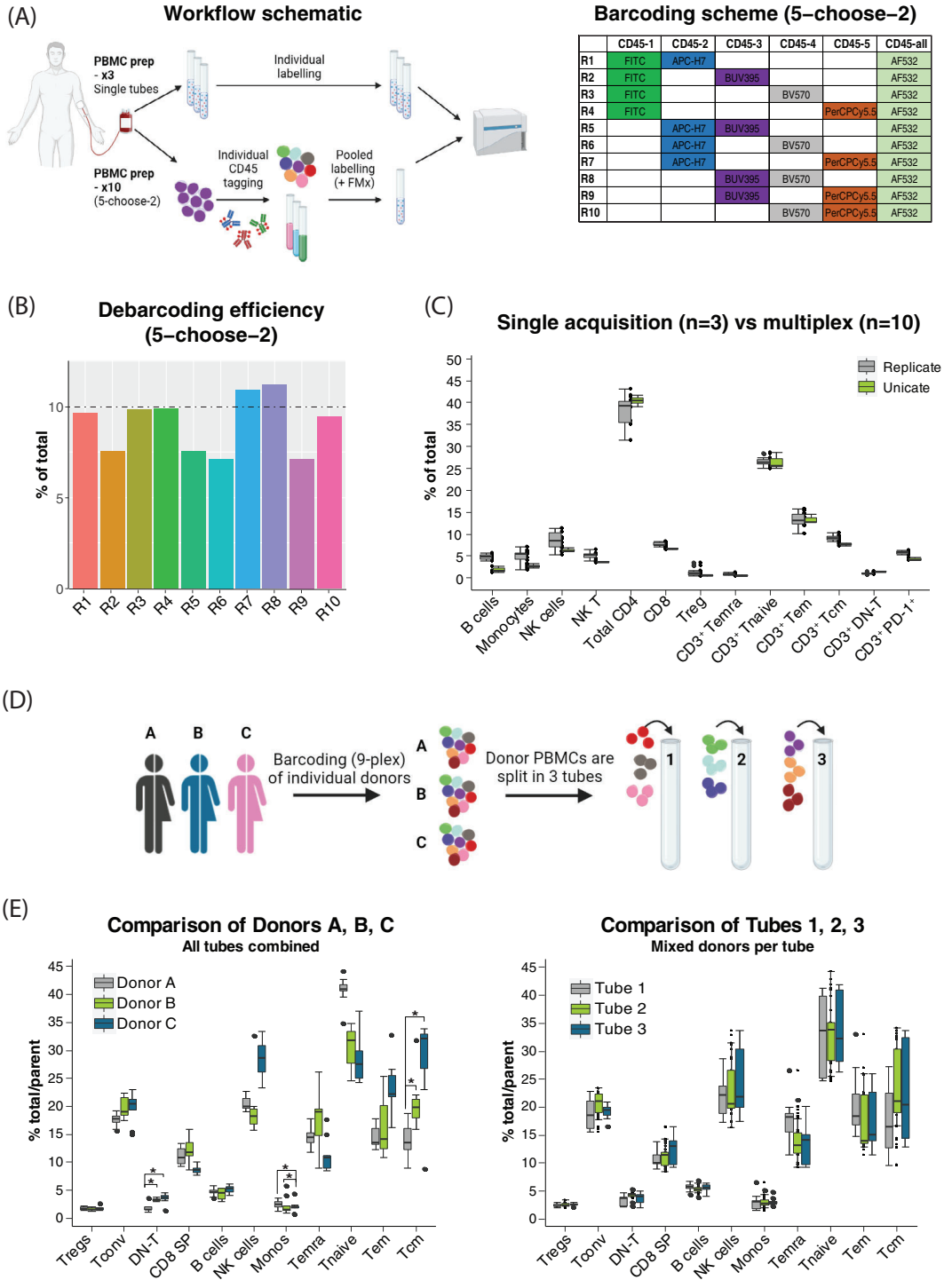


| | CD45-1 | CD45-2 | CD45-3 | CD45-4 | CD45-5 | CD45-all |
|---|---|---|---|---|---|---|
| R1 | FITC | APC-H7 | | | | AF532 |
| R2 | FITC | | BUV395 | | | AF532 |
| R3 | FITC | | | BV570 | | AF532 |
| R4 | FITC | | | | PerCPCy5.5 | AF532 |
| R5 | | APC-H7 | BUV395 | | | AF532 |
| R6 | | APC-H7 | | BV570 | | AF532 |
| R7 | | APC-H7 | | | PerCPCy5.5 | AF532 |
| R8 | | | BUV395 | BV570 | | AF532 |
| R9 | | | BUV395 | | PerCPCy5.5 | AF532 |
| R10 | | | | BV570 | PerCPCy5.5 | AF532 |

**FIGURE 1** CD45 barcoding allows for PBMC lineage resolution comparable to single-tube acquisition and does not introduce artifacts. (A) Barcoding schematic. Left: Illustration of barcoding workflow (CD45 tags; exemplary 5-choose 2 approach) for the analysis of n = 10 individual PBMC samples or n = 3 PBMC samples from the same donor labeled and acquired individually (no barcoding). Post-CD45 labelling, cells were labeled with the identical immunophenotyping antibody mix. Right: Pipetting schematic for the 5-choose-2 barcoding approach. (B) The debarcoding efficiency of $CD45^+$ barcoded unique samples post-Boolean gating was compared for a representative 5-choose-2 experiment. (C) PBMCs from the same donor were barcoded (5-choose-3, n = 10) and postunmixing compared to single-tube acquisition (n = 3). The frequency of main PBMC lineages and PD-$1^+$ T cells was assessed via manual gating. Tem, effector memory T cells; Tcm, central memory T cells; Temra, terminally differentiated T cells. (D) Schematic of the batch effect experiment to compare 3 different PBMC donors (A, B, C) split across 3 tubes [1–3] with unique barcodes each. A, B and C were each uniquely barcoded (n = 9, 5-choose-2) and then split tubes 1, 2 or 3. Each tube contained 9 unique mixes from 3 different donors (1 – ABC, 2 – BCA, 3 – CAB). (E) Postdebarcoding, recovered cells were analyzed by manual gating. Cell populations from A, B and C were compared (donor comparison) as well as overall populations present in each tube 1, 2 or 3 (tube comparison). Tem, effector memory T cells; Tcm, central memory T cells; Temra, terminally differentiated T cells; DN T, $CD4^-CD8^-$ T cells; monos, monocytes [Color figure can be viewed at wileyonlinelibrary.com]

9.0% ± 1.6%). In this protocol, all samples (unicates as well as replicates) were stained with a common, identical anti-CD45 antibody. The comparison of the abundance of $CD45^+$ cell lineages among debarcoded replicates (n = 10) with separately acquired $CD45^+$ unicates (n = 3) revealed that there were no statistically significant differences between major PBMC lineages ($CD19^+$ B cells, $CD14^+$ monocytes, $CD56^+$ NK cells and $CD3^+$ T cells, Figure 1C, Supplementary Figure 1B and Supplementary Table 1). In addition, broad T cell populations ($CD4^+$, $CD8^+$ single-positive and $CD4^-CD8^-$ double-negative [DN] T cells) and subsets thereof were compared. This included regulatory T cells (Treg, $CD3^+$ $CD4^+$ $CD25^{high}$ $CD127^-$), naïve T cells ($CD197^+$ $CD45RA^+$) as well as central memory (Tcm, $CD3^+$ $CD197^+$ $CD45RA^-$), effector memory (Tem, $CD3^+$ $CD197^-$ $CD45RA^-$) and terminally differentiated (Temra, $CD3^+$ $CD197^-$ $CD45RA^+$) T cells. None of these subsets from the multiplexed acquisition was statistically significantly different from individually acquired samples (unicates). Overall, the numbers were comparable.

We next assessed if the method might suffer from poorer population separation if PBMCs from different donors were simultaneously acquired (for instance, due to donor-specific autofluorescence, cell activation status and consequently donor-specific differences in SE). Furthermore, it was unclear if splitting samples from several different donors into different tubes followed by successive acquisition would impact the overall performance of the panel though the introduction of additional batch effects. Consequently, we designed an experiment where PBMCs from three individual donors (termed A, B and C) were individually barcoded with n = 9 different CD45 tags (using the above-described 5-choose-2 approach). Subsequently, these PBMCs were mixed equally in such a way that unique barcodes referenced n = 3 individually labeled PBMC samples from each of the three donors in three individual tubes (tube 1, ABCABCABC vs. tube 2, BCABCABCA vs. tube 3, CABCABCAB). After pooling the donors in three individual tubes, the cell suspensions were labeled with a common lineage staining mix followed by acquisition (Figure 1D). Postdebarcoding, n = 9 samples of each of the n = 3 donors were assessed for main PBMC subset abundance (intra-donor comparison). The pooled PBMC composition of the three tubes (each containing three samples of each donor) was also compared (inter-tube comparison, Figure 1E). This analysis suggested that we detected donor-specific statistically significant differences between $CD14^+$ monocytes, $CD4^-CD8^-$ double-negative (DN) $CD3^+$ T cells and $CD3^+$ $CD197^+$ $CD45RA^-$ Tcm cells, while there was no statistically significant difference between the same subsets in each tube as expected for a repeated analysis of pooled donors split over several tubes (Supplementary Table 2).

Together, these experiments suggested that anti-CD45 fluorescent cell labelling of n = 10 live PBMCs does not significantly impact the identification of PBMC lineages. As a next step, we decided to develop a more comprehensive immunophenotyping protocol for detailed T cell subset analysis and designed a 6-choose-3 anti-CD45 barcoding approach (Supplementary Figure 2A). Pooled PBMCs from the same donor were challenged with an antibody mix allowing to discriminate between main PBMC subsets, specialized T cell subsets and several cell surface activation markers (CD28, CD278, CD279, CD223, CD134, CD137 and CD154). After multiplexed acquisition of n = 20 identical PBMC samples, the individual debarcoding efficiency was again highly efficient (4.78% ± 0.38%) (Figure 2A). We applied manual gating on the debarcoded samples (Supplementary Figure 2B) followed by optSNE dimensionality reduction (Figure 2B). This suggested that there was a very reliable debarcoding efficiency of the major PBMC lineages (B cells, monocytes, NK cells and NK-T cells). T cell subsets such as Treg, T naïve, Tcm and Tem as well as Temra $CD4^+$ and $CD8^+$ T cells were also faithfully identified (Figure 2B-D and Supplementary Table 3). Importantly, the variance (%CV) of each of the populations we assessed was well below 20% including rarer populations such as Treg or memory T cells (Figure 2E-F and Supplementary Table 4). The only exceptions here were monocytes with a variance of 22.7% and $CD8^+$ central memory T cells with a variance of 33.3%. Importantly, both on $CD4^+$ and $CD8^+$ T cells, highly expressed CD28 as well as low-expressed activation marker CD279 (PD-1) were well detectable in all debarcoded samples (Supplementary Figure 2B and Supplementary Table 5). This was also supported by the relatively low variance in the median fluorescence (MFI) of these markers (Supplementary Figure 3A-B and Supplementary Table 6). As expected, non or low-expressed markers (for instance, CD154) did not always meet the 20%CV cut-off criteria (not shown).

### 3.2 | Simultaneous challenge of pooled, barcoded PBMCs reveals drastic PHA-mediated changes to immune cell composition

Multiplexing is often applied in situations where timing of a cellular stimulus is critical to reduce operator-induced variability of results [24, 31]. We thus adapted our barcoding protocol (5-choose-2, n = 10 samples, Supplementary Figure 3C) for use with a slightly modified immunophenotyping protocol described in the previous paragraph to assess barcoded and pooled, simultaneously challenged PBMCs (Figure 3A). Concretely, we pooled barcoded PBMCs from n = 10 donors and challenged them for 48 h with PHA (2.0 μg/ml), a plant-derived lectin with strong mitogenic activity [43]. Postchallenge, the pooled cells were then labeled with identical 20-color immunophenotyping cocktails. In this experiment, we sought to assess (1) if the anti-CD45 barcodes were stable for prolonged periods of time at 37°C in culture conditions, and (2) if the application of unbiased machine-learning approaches for data analysis would help us identify MoA related phenotypic immune cell changes. We applied optSNE for dimensionality reduction and the illustration of PBMC populations followed by FlowSOM clustering of the combined concatenated dataset. Our approach revealed that, while effective de-barcoding was still possible, the labelling efficiency of certain fluorochromes (e.g., CD45-AF532 and CD45-PerCPCy5.5) was reduced (Supplementary Figure 3C). Postdebarcoding, we identified n = 20 metaclustered cell populations through FlowSOM (Figure 3B and Supplementary

ISAC CYTOMETRY Journal of Quantitative Cell Science PART A

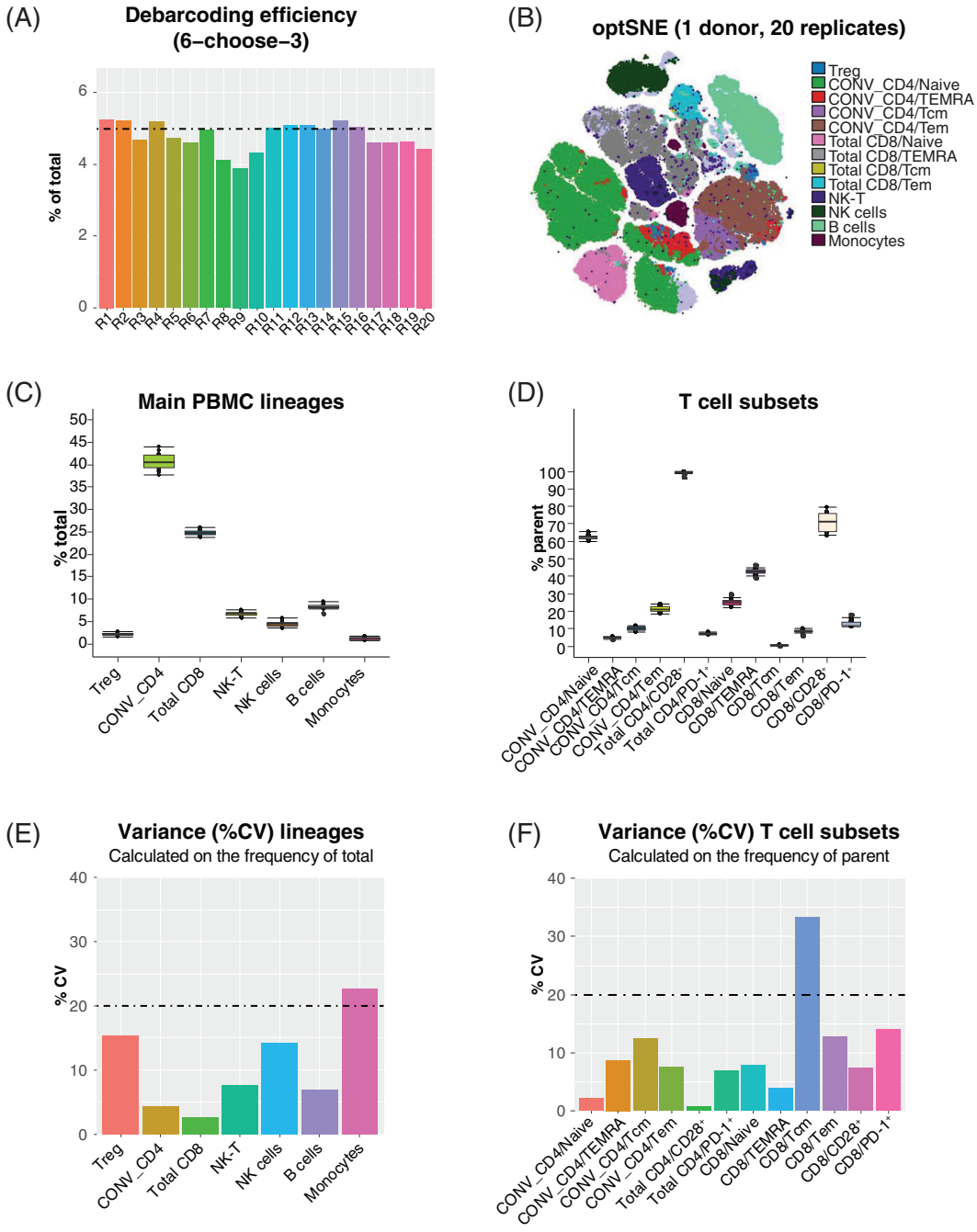


**FIGURE 2** The 6-choose-3 barcoding allows for high resolution of T cell subsets in n = 20 multiplexed PBMC replicates with acceptable variance. (A) Debarcoding efficiency of n = 20 pooled multiplexed samples (n = 20, 6-choose-3). Samples were derived from one donor. (B) Visualization (optSNE) of 14 main PBMC populations on n = 20 concatenated debarcoded samples from (A). Populations were assigned using manual gating. Tem, effector memory T cells; Tcm, central memory T cells; Temra, terminally differentiated T cells; DN T, $CD4^{-}CD8^{-}$ T cells. C. Frequencies (% total) of main PBMC lineages identified in (B). (D) T cell subsets (% of patent $CD3^{+}$) as identified in (B). (E) Variance (%CV) of main PBMC lineages in (C). (F) Variance (%CV) of T cell subsets in (D) [Color figure can be viewed at wileyonlinelibrary.com]

Table 7). Interestingly, some of these were only found in either treatment-naïve or PHA-challenged conditions (Figure 3C), suggesting drastic MoA related effects of PHA. Indeed, we found that a total of n = 14 populations (out of 20 identified) had statistically significant changes in their abundance (Figure 3D and Supplementary Table 8). These mostly reflected changes in the abundance of T cell subsets such as Tregs and activated $CD4^{+}$ and $CD8^{+}$ T cells characterized through differential expression of activation markers such as CD154, CD137, CD223, CD278, CD279 and CD366 (Figure 3D, Supplementary Figure 3D and Supplementary Results). Interestingly, we also found that $CD14^{hi}$ monocytes as well as NK cells and a B cell cluster changed in abundance (possibly due to

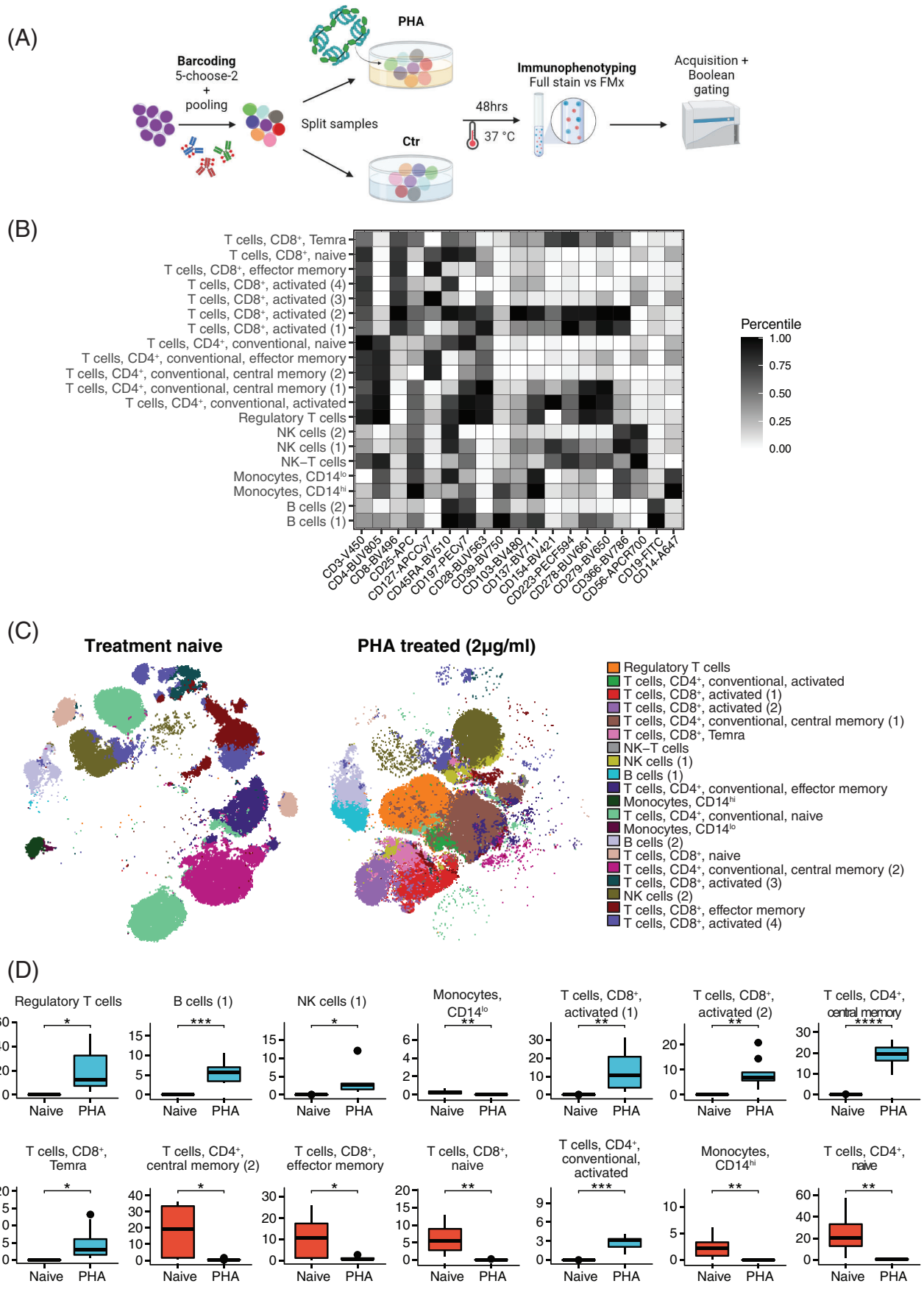


**FIGURE 3** Legend on next page.

bystander effects of T cell activation). In summary, the simultaneous challenge of pooled barcoded PBMCs proved to be a viable application for our assay protocol while at the same time highlighting possible limitations for the live culture of barcoded cells.

### 3.3 | Multiplexed analysis of SEB challenged PBMCs identifies unique CD4$^+$ T cell clusters with distinct activation profiles

Encouraged by these observations, we decided to adapt our 6-choose-3 barcoding approach (Supplementary Figure 2) to another real-life immunophenotyping application. *Staphylococcus* enterotoxin B (SEB) is a highly potent toxin, which activates human CD4$^+$ T cells in a polyclonal fashion followed by cellular activation and release of pro-inflammatory cytokines. Even though SEB-mediated immune responses have been studied using various cytometry techniques [44], unbiased comprehensive immunophenotyping of the T cell compartment with high-cellular resolution in vitro has not yet been carried out.

Consequently, we cultured PBMCs from n = 20 different donors individually followed by challenge with SEB (1.0 μg/ml) for 48 h. After cell culture, the cells were barcoded, pooled and stained with a 21-parameter immunophenotyping master mix which was designed to minimize overall spectral complexity and possible SE effects (Figure 3A and Supplementary Figure 4A). Postacquisition and debarcoding of live cells, we again employed machine-learning approaches for data analysis and PBMC subset identification (Figure 4A). This workflow led to the identification of 17 PBMC metaclusters according to their cell surface marker expression (Figure 4B, Supplementary Figure 4B and Supplementary Table 9). As expected from the purported MoA, we observed significant changes in the abundance of specific immune cell subsets under SEB challenge (Figure 4C, D and Supplementary Table 10). For instance, we identified conventional/highly activated CD4$^+$ T cells as well as CD4$^+$ Tcm and CD4$^+$ Tem cells to be significantly increased under SEB challenge. Both CD4$^+$ as well as CD4$^+$ Tem cells were reduced. CD8$^+$ Tem cells were also less abundant post-SEB challenge, while CD14$^{hi}$ monocytes practically disappeared. In addition, we identified two clusters of CD4$^+$ T cells unique to the SEB challenge. These highly activated cells were unique in their CD279, CD134, CD137 and CD154 expression. Both clusters of activated CD4$^+$ T cells were clearly detectable post-SEB challenge but practically absent under naïve conditions (Figure 4D). Specifics as to the cell surface marker characterization of these cells are summarized in the Supplementary Results. Taken together, these findings highlight the potential of our barcoded flow cytometry workflow to identify unique SEB-induced changes in the abundance of immune cell types in a highly parallelized manner.

## 4 | DISCUSSION

Here, we present a full spectrum flow cytometry based multiplexing panel allowing for the simultaneous acquisition of up to n = 20 different PBMC samples. Using a 5-choose-2 approach (up to n = 10 samples) or applying a more complex 6-choose-3 approach (up to n = 20 samples), we found robust debarcoding efficiency of individual samples using a standard Boolean gating approach. For instance, for the 6-chose-3 approach, the debarcoding efficiency was excellent with an average of 4.8% ± 0.4% (ideal: 5%). These results are in the range of (or even exceed) observed debarcoding efficiencies typical for CyTOF, the current benchmark for this technology [19]. Importantly, the fluorescent tags of the anti-CD45 barcodes did not introduce major variance to the frequency of main PBMC lineages or T cell subsets post debarcoding suggesting limited effects of barcode SE on downstream populations. The %CV of critical (manually gated) populations remained under 20% which we consider an acceptance criterion in most flow cytometry validation protocols [14, 45]. Only monocytes and CD8$^+$ Tcm cells could be resolved with less precision. Given the intrinsic increased autofluorescence of monocytes and the very low abundance of CD8$^+$ Tcm cells in our experimental setting (0.49% ± 0.16%), we find these results acceptable. In addition, barcoding helped minimize intra-sample variance, which is in agreement with CyTOF barcoding results [19]. Finally, comparing the results of manually gated PBMC and T cell subset populations on identical samples, we found that barcoding did not affect the results of optSNE mediated dimensionality reduction and the representation of n = 13 manually defined populations.

Based on these observations, we developed a barcoding and immunophenotyping workflow employing unbiased machine-learning approaches including FlowSOM and optSNE. The aim was to study activation-induced changes to PBMC subset composition in different scenarios. In the first 5-choose-2 protocol, we assessed the effects of

**FIGURE 3** Assessing immunophenotypic changes in pooled barcoded PBMCs simultaneously challenged with PHA. (A) Schematic of the PHA challenge assay. PBMCs from n = 10 donors were individually barcoded using a 5-choose-2 approach. Subsequently, cells were pooled and split into two experimental conditions where they were either simultaneously challenged with PHA (2.0 μg/ml) or left treatment naïve. After 48 h, cells were harvested and jointly labeled with immunophenotyping master mix (FMx or full stain including all activation markers) and acquired at the cytometer. We subsequently applied FlowSOM and optSNE for further analysis. (B) Normalized expression heatmap for n = 20 cell metaclusters identified in either treatment condition. (C) Illustration of the relative abundance of the n = 20 populations identified in (B) in treatment naïve and PHA challenged PBMCs (optSNE on concatenated samples). (D) Statistical analysis (paired t-test, BH corrected) for the populations identified in B. Only populations with statistically significant changes upon PHA challenge are displayed [Color figure can be viewed at wileyonlinelibrary.com]

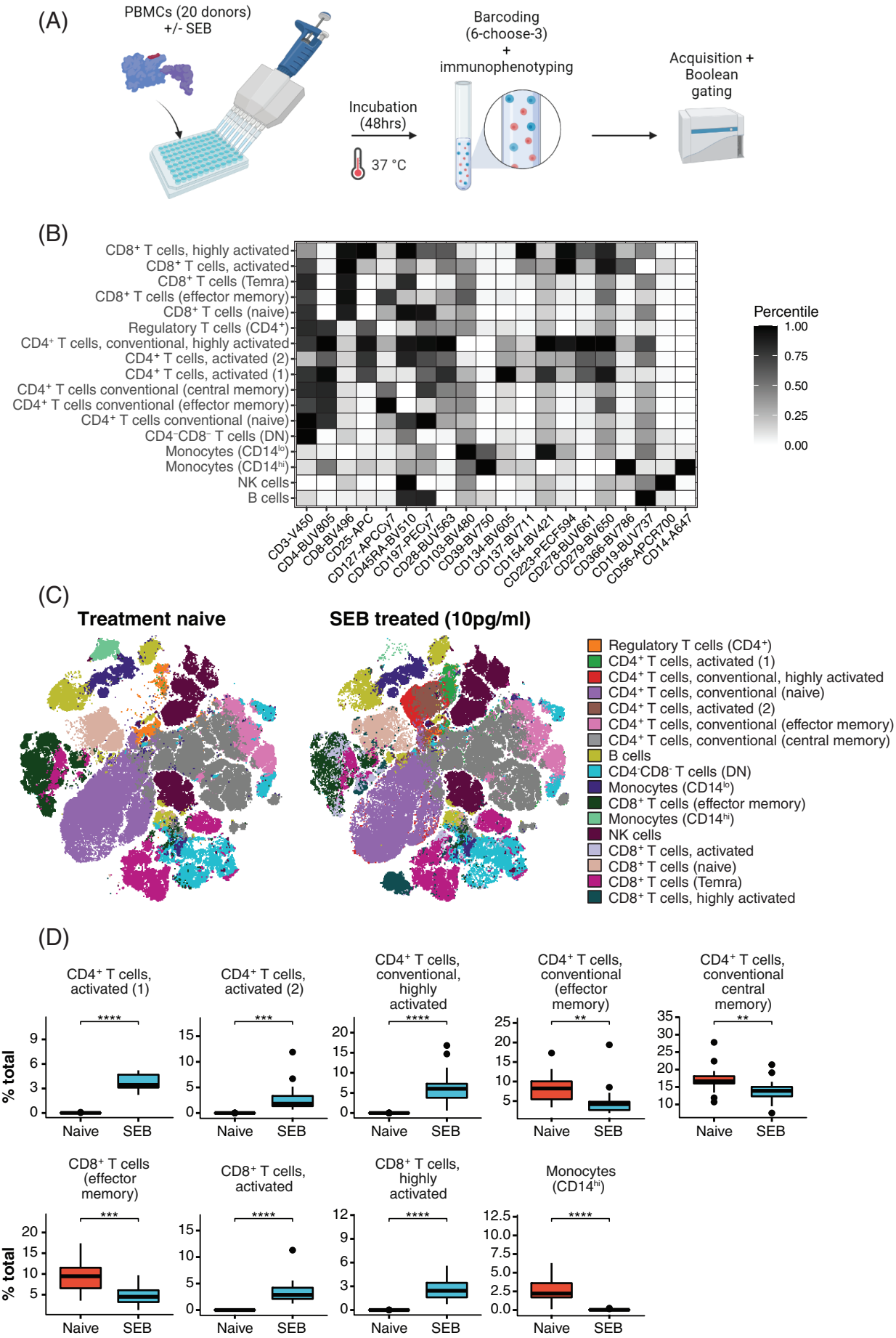


FIGURE 4 Legend on next page.

PHA on the abundance of n = 20 PBMC populations identified in control or challenged conditions. This protocol used cells that were barcoded and pooled prior to simultaneous challenge. We noticed that after the 48 h cell culture period, the staining intensity of the anti-CD45 antibodies (especially CD45-AF532 and CD45-PerCPCy5.5) was somewhat reduced compared to situations with barcoding on ice followed by immediate pooled immunophenotyping and analysis. Nevertheless, we were able to identify changes mostly in the T cell compartment but also in the abundance of an activated NK cell cluster and a B cell cluster. Even though PHA has mostly been studied in the context of T cell activation [35, 46], these observations might be the result of bystander activation (e.g., though the release of cytokines post T cell activation). We next assessed a refined 6-choose-3 barcoded 21-color immunophenotyping panel in a 48 h PBMC stimulation setting. Here, PBMCs were challenged individually with SEB, a known T cell activator [47], which is occasionally used for PD biomarker purposes [47–50]. However, in-depth immunophenotyping by flow cytometry at the PBMC population level has not been performed. A relatively recent CyTOF based analysis of leukemia patient PBMCs challenged with SEB found functional differences in T cell memory subset responses and different cytokine release profiles, but did not unbiasedly characterize changes in the abundance of these subsets [44]. Furthermore, the manual gating approach used might underappreciate rare effector cell subsets or cell clusters not present before or after treatment [51]. Consequently, we tailored our next barcoding workflow to characterize SEB-mediated changes in specific PBMC T cell subsets. As a result, we confirmed previous findings that primarily, $CD4^+$ T cell subsets change in abundance under SEB challenge. We observed the appearance of two unique activation-specific $CD4^+$ T cell clusters at the expense of less activated Tcm and Tem $CD4^+$ populations. This is somewhat similar to APC mediated T cell activation characteristic of functional responses including Interferon-γ release and proliferation [52, 53]. Monocytes and $CD8^+$ Tem cells were reduced, but this could be a relative decrease due to the increase in abundance of the aforementioned expansion of $CD4^+$ populations. Importantly, in both the PHA and SEB challenge experiments, hypothesis-guided manual gating would probably have missed activation status-specific cell clusters thus highlighting the usefulness of our multiplexed immunophenotyping protocol followed by algorithm-guided machine learning.

Compared to other flow cytometry or mass cytometry based barcoding protocols which rely on cellular fixation [25, 29], our assay allows for the multiplexed analysis of live PBMCs, which could be recovered by cell sorting for further functional assessment or additional in vitro culture if desired. In addition, it works on bulk PBMCs and does not require the use of cell lines or magnetically enriched cell populations [31]. Recently, for CyTOF, barcoded analysis of live PBMCs has been introduced [20]. Nevertheless, we believe that our assay protocol entails, as an additional advantage besides the expected lower operational cost of full-spectrum cytometers, less time and potentially higher overall debarcoding efficiency [54, 55]. In addition, the sensitivity (and thus resolution) of CyTOF mass reporters can be lower than that of quantum-efficient fluorochromes [56]. This provides additional incentives for the use of high-parameter flow cytometry panels in situations where samples and target cell populations may be rare.

The barcoding protocol we present here should limit operator- or platform-induced variability and especially help algorithm aided single-cell analysis workflows. Further improvement of the protocol should address the currently observed variability of very rare populations, such as $CD8^+$ Tcm cells and monocytes. In addition, CD45 expression is not equal on all peripheral blood immune cells, which could result in further challenges when multiplexing more complex immune cell populations than PBMCs such as lysed whole-blood including granulocytes. Consequently, additional improvements to the method could include adaptations of other multiplexing strategies as recently described for CyTOF. For instance, co-labelling of ubiquitously expressed molecules such as beta-2-microglobulin and CD298 on immune cells could further lead to increased debarcoding resolution [20]. Finally, further streamlining may be achieved through computational debarcoding methods as presented elsewhere [23, 24]. In addition, if barcoded samples are to be pooled for simultaneous short-term challenge such as phosphorylation studies, the protocol should be adapted for shorter incubation periods and possibly include a fixation step. In summary, our combined barcoding and immunophenotyping panel allows for the precise and automated analysis of phenotypic changes in specific T cell subsets. It could thus represent a valuable resource for various immunophenotyping protocols benefiting from highly parallelized assessment of many donors or treatment conditions.

**FIGURE 4** Multiplexed assessment of individually SEB challenged PBMCs of n = 20 donors facilitates analysis of MoA related changes in T cell subsets. (A) Schematic of the SEB PBMC challenge assay. PBMCs from n = 20 individual healthy donors were individually incubated with SEB for 48 h (or remained treatment naïve). Using a 6-choose-3 approach, they were then barcoded and pooled. Barcoded PBMCs were immediately incubated with an immunophenotyping antibody cocktail comprising n = 21 markers. Finally, using optSNE and FlowSOM, the effect of SEB activation on T cells was assessed. (B) Normalized expression heatmap for n = 20 cell metaclusters identified in either treatment condition. (C) Visualization of n = 17 PBMC metaclusters identified using the approach in B. D. Statistical analysis (multiple paired t-tests) on cell clusters identified in B revealed SEB mode-of-action related changes predominantly in the $CD4^+$ T cell compartment. Only populations with statistically significant changes upon PHA challenge are displayed [Color figure can be viewed at wileyonlinelibrary.com]

## ACKNOWLEDGMENTS

We would like to thank the following people who helped with certain aspects at various stages of this study: Solveig Runge for help with antibody titrations; Bernhard Reis for initial discussions on design and use of multiplexing flow cytometry assays. Assay schematics as well as the graphical overview were created using BioRender (Created with BioRender.com; app.biorender.com; last accessed 25/11/2021).

## AUTHOR CONTRIBUTIONS

**Fabian Junker:** Conceptualization (lead); data curation (lead); formal analysis (lead); investigation (equal); methodology (equal); software (lead); supervision (equal); visualization (lead); writing – original draft (lead); writing – review and editing (equal). **Priscila Camillo Teixeira:** Conceptualization (supporting); project administration (lead); resources (lead); supervision (equal); writing – original draft (supporting); writing – review and editing (equal).

## CONFLICT OF INTEREST

All authors are current or former employees of F. Hoffmann-La Roche Ltd. and may own company stock.

## ORCID

*Fabian Junker* https://orcid.org/0000-0003-4548-9842

## REFERENCES

1. Liechti T, Roederer M. OMIP-060: 30-parameter flow Cytometry panel to assess T cell effector functions and regulatory T cells. Cytometry A. 2019;95:1129–34.
2. Liechti T, Gunthard HF, Trkola A. OMIP-047: high-dimensional phenotypic characterization of B cells. Cytometry A. 2018;93:592–6.
3. Liechti T, Roederer M. OMIP-051 - 28-color flow cytometry panel to characterize B cells and myeloid cells. Cytometry A. 2019;95:150–5.
4. Mair F, Prlic M. OMIP-044: 28-color immunophenotyping of the human dendritic cell compartment. Cytometry A. 2018;93:402–5.
5. Mair F, Liechti T. Comprehensive Phenotyping of human dendritic cells and monocytes. Cytometry A. 2021;99:231–42.
6. Park LM, Lannigan J, Jaimes MC. OMIP-069: forty-color full Spectrum flow Cytometry panel for deep Immunophenotyping of major cell subsets in human peripheral blood. Cytometry A. 2020;97:1044–51.
7. Sahir F, Mateo JM, Steinhoff M, Siveen KS. Development of a 43 color panel for the characterization of conventional and unconventional T-cell subsets, B cells, NK cells, monocytes, dendritic cells, and innate lymphoid cells using spectral flow cytometry. Cytometry A. 2020;1–7. doi:10.1002/cyto.a.24288
8. Ferrer-Font L, Pellefigues C, Mayer JU, Small SJ, Jaimes MC, Price KM. Panel design and optimization for high-dimensional Immunophenotyping assays using spectral flow Cytometry. Curr Protoc Cytom. 2020;92:e70.
9. Sahaf B, Rahman A, Maecker HT, Bendall SC. High-parameter immune profiling with CyTOF. Methods Mol Biol. 2020;2055:351–68.
10. Mair F, Hartmann FJ, Mrdjen D, Tosevski V, Krieg C, Becher B. The end of gating? An introduction to automated analysis of high dimensional cytometry data. Eur J Immunol. 2016;46:34–43.
11. Van Gassen S, Gaudilliere B, Angst MS, Saeys Y, Aghaeepour N. CytoNorm: a normalization algorithm for Cytometry data. Cytometry A. 2020;97:268–78.
12. Liechti T, Weber LM, Ashhurst TM, Stanley N, Prlic M, Van Gassen S, et al. An updated guide for the perplexed: cytometry in the high-dimensional era. Nat Immunol. 2021;22:1190–7.
13. Cossarizza A, Chang HD, Radbruch A, Acs A, Adam D, Adam-Klages S, et al. Guidelines for the use of flow cytometry and cell sorting in immunological studies (second edition). Eur J Immunol. 2019;49:1457–973.
14. Spitz S, Zhang Y, Fischer S, McGuire K, Sommer U, Amaravadi L, et al. White paper on recent issues in bioanalysis: BAV guidance, CLSI H62, biotherapeutics stability, parallelism testing, CyTOF and regulatory feedback (part 2A - recommendations on biotherapeutics stability, PK LBA regulated bioanalysis, biomarkers assays, Cytometry Validation & Innovation Part 2B - regulatory Agencies' inputs on bioanalysis, biomarkers, immunogenicity, Gene & Cell Therapy and vaccine). Bioanalysis. 2020;2021(13):295–361.
15. Cannarile MA, Gomes B, Canamero M, Reis B, Byrd A, Charo J, et al. Biomarker technologies to support early clinical Immuno-oncology development: advances and interpretation. Clin Cancer Res. 2021;27:4147–59.
16. Wagar LE. Live cell barcoding for efficient analysis of Small samples by mass Cytometry. Methods Mol Biol. 2019;1989:125–35.
17. McCarthy RL, Mak DH, Burks JK, Barton MC. Rapid monoisotopic cisplatin based barcoding for multiplexed mass cytometry. Sci Rep. 2017;7:3779.
18. Lai L, Ong R, Li J, Albani S. A CD45-based barcoding approach to multiplex mass-cytometry (CyTOF). Cytometry A. 2015;87:369–74.
19. Mei HE, Leipold MD, Schulz AR, Chester C, Maecker HT. Barcoding of live human peripheral blood mononuclear cells for multiplexed mass cytometry. J Immunol. 2015;194:2022–31.
20. Hartmann FJ, Simonds EF, Bendall SC. A universal live cell barcoding-platform for multiplexed human single cell analysis. Sci Rep. 2018;8:10770.
21. Muftuoglu M, Li L, Liang S, Mak D, Lin AJ, Fang J, et al. Extended live-cell barcoding approach for multiplexed mass cytometry. Sci Rep. 2021;11:12388.
22. Reisman BJ, Barone SM, Bachmann BO, Irish JM. DebarcodeR increases fluorescent cell barcoding capacity and accuracy. Cytometry A. 2021;99:946–53.
23. Zunder ER, Finck R, Behbehani GK, Amir el AD, Krishnaswamy S, Gonzalez VD, et al. Palladium-based mass tag cell barcoding with a doublet-filtering scheme and single-cell deconvolution algorithm. Nat Protoc. 2015;10:316–33.
24. Tsai WL, Vian L, Giudice V, Kieltyka J, Liu C, Fonseca V, et al. High throughput pSTAT signaling profiling by fluorescent cell barcoding and computational analysis. J Immunol Methods. 2020;477:112667.
25. Krutzik PO, Clutter MR, Trejo A, Nolan GP. Fluorescent cell barcoding for multiplex flow cytometry. Curr Protoc Cytom. 2011;55:6.31.1–6.31.15.
26. Kulhanek KR, Myers DR, Ksionda O, Vercoulen Y, Romero-Moya D, Roose JP. Protocol for barcoding T cells combined with timed stimulations. STAR Protoc. 2020;1:100067.
27. Giudice V, Fantoni G, Biancotto A. Fluorescent cell barcoding for Immunophenotyping. Methods Mol Biol. 2019;2032:53–68.
28. Lambert C, Preijers F, Yanikkaya Demirel G, Sack U. Monocytes and macrophages in flow: an ESCCA initiative on advanced analyses of monocyte lineage using flow cytometry. Cytometry B Clin Cytom. 2017;92:180–8.
29. Giudice V, Feng X, Kajigaya S, Young NS, Biancotto A. Optimization and standardization of fluorescent cell barcoding for multiplexed flow cytometric phenotyping. Cytometry A. 2017;91:694–703.
30. Krutzik PO, Nolan GP. Fluorescent cell barcoding in flow cytometry allows high-throughput drug screening and signaling profiling. Nat Methods. 2006;3:361–8.
31. Akkaya B, Miozzo P, Holstein AH, Shevach EM, Pierce SK, Akkaya M. A simple, versatile antibody-based barcoding method for flow Cytometry. J Immunol. 2016;197:2027–38.
32. Robinson JP. Spectral flow Cytometry - quo Vadimus? Cytometry A. 2019;95(95a):823–4.

ISAC CYTOMETRY Journal of Quantitative Cell Science PART A


33. Bonilla DL, Reinin G, Chua E. Full Spectrum flow Cytometry as a powerful Technology for Cancer Immunotherapy Research. Front Mol Biosci. 2021;7.
34. Hamelryck TW, Dao-Thi MH, Poortmans F, Chrispeels MJ, Wyns L, Loris R. The crystallographic structure of phytohemagglutinin-L. J Biol Chem. 1996;271:20479–85.
35. Kuo YC, Weng SC, Chou CJ, Chang TT, Tsai WJ. Activation and proliferation signals in primary human T lymphocytes inhibited by ergosterol peroxide isolated from Cordyceps cicadae. Br J Pharmacol. 2003;140:895–906.
36. Phillips B, Roitt IM. Evidence for transformation of human B lymphocytes by PHA. Nat New Biol. 1973;241:254–6.
37. Maddaly R, Pai G, Balaji S, Sivaramakrishnan P, Srinivasan L, Sunder SS, et al. Receptors and signaling mechanisms for B-lymphocyte activation, proliferation and differentiation - insights from both in vivo and in vitro approaches. FEBS Lett. 2010;584:4883–94.
38. Aguilar JL, Varshney AK, Pechuan X, Dutta K, Nosanchuk JD, Fries BC. Monoclonal antibodies protect from staphylococcal enterotoxin K (SEK) induced toxic shock and sepsis by USA300 Staphylococcus aureus. Virulence. 2017;8:741–50.
39. Belkina AC, Ciccolella CO, Anno R, Halpert R, Spidlen J, Snyder-Cappione JE. Automated optimized parameters for T-distributed stochastic neighbor embedding improve visualization and analysis of large datasets. Nat Commun. 2019;10:5415.
40. Van Gassen S, Callebaut B, Van Helden MJ, Lambrecht BN, Demeester P, Dhaene T, et al. FlowSOM: using self-organizing maps for visualization and interpretation of cytometry data. Cytometry A. 2015;87:636–45.
41. Junker F, Gulati P, Wessels U, Seeber S, Stubenrauch KG, Codarri-Deak L, et al. A human receptor occupancy assay to measure anti-PD-1 binding in patients with prior anti-PD-1. Cytometry A. 2021;99:832–43.
42. Schulz AR, Mei HE. Surface barcoding of live PBMC for multiplexed mass Cytometry. Methods Mol Biol. 2019;1989:93–108.
43. Michalowski A. Phytohaemagglutinin-stimulated division and growth rate of human lymphocytes. Bull Acad Pol Sci Biol. 1967;15:577–81.
44. Rudolph ME, McArthur MA, Barnes RS, Magder LS, Chen WH, Sztein MB. Differences between pediatric and adult T cell responses to in vitro staphylococcal enterotoxin B stimulation. Front Immunol. 2018;9:498.
45. O'Hara DM, Xu Y, Liang Z, Reddy MP, Wu DY, Litwin V. Recommendations for the validation of flow cytometric testing during drug development: II assays. J Immunol Methods. 2011;363:120–34.
46. Movafagh A, Heydary H, Mortazavi-Tabatabaei SA, Azargashb E. The significance application of indigenous Phytohemagglutinin (PHA) mitogen on metaphase and cell culture procedure. Iran J Pharm Res. 2011;10:895–903.
47. McLeod JD, Walker LS, Patel YI, Boulougouris G, Sansom DM. Activation of human T cells with superantigen (staphylococcal enterotoxin B) and CD28 confers resistance to apoptosis via CD95. J Immunol. 1998;160:2072–9.
48. Seprenyi G, Abe J, Kohsaka T. Primary cytotoxicity of SEB-activated human PBMC and separated CD8+ and CD4+ T lymphocytes elicited by two different stimulation protocols. Immunol Cell Biol. 1996;74:483–9.
49. Wang C, Thudium KB, Han M, Wang XT, Huang H, Feingersh D, et al. Srinivasan M and others. In vitro characterization of the anti-PD-1 antibody nivolumab, BMS-936558, and in vivo toxicology in non-human primates. Cancer. Immunol Res. 2014;2:846–56.
50. Deng N, Mosmann TR. Optimization of the cytokine secretion assay for human IL-2 in single and combination assays. Cytometry A. 2015;87:777–83.
51. Mair F. Gate to the future: computational analysis of Immunophenotyping data. Cytometry A. 2019;95:147–9.
52. Lichtenegger FS, Rothe M, Schnorfeil FM, Deiser K, Krupka C, Augsberger C, et al. Targeting LAG-3 and PD-1 to enhance T cell activation by antigen-presenting cells. Front Immunol. 2018;9:385.
53. Mura M, Chaudhury S, Farooq F, Duncan EH, Beck K, Bergmann-Leitner ES. Optimized flow cytometric protocol for the detection of functional subsets of low frequency antigen-specific CD4(+) and CD8(+) T cells. MethodsX. 2020;7:101005.
54. Gadalla R, Noamani B, MacLeod BL, Dickson RJ, Guo M, Xu W, et al. Validation of CyTOF against flow Cytometry for immunological studies and monitoring of human. Cancer Clinical Trials Front Oncol. 2019;9:415.
55. Mistry AM, Greenplate AR, Ihrie RA, Irish JM. Beyond the message: advantages of snapshot proteomics with single-cell mass cytometry in solid tumors. FEBS J. 2019;286:1523–39.
56. Spitzer MH, Nolan GP. Mass cytometry: single cells, many features. Cell. 2016;165:780–91. https://doi.org/10.1016/j.cell.2016.04.019


## SUPPORTING INFORMATION

Additional supporting information may be found in the online version of the article at the publisher's website.

Received: 1 October 2021 | Revised: 21 December 2021 | Accepted: 11 January 2022

DOI: 10.1002/cyto.a.24540

PHENOTYPE REPORTS

MIFlowCyt

ISAC INTERNATIONAL SOCIETY FOR ADVANCEMENT OF CYTOMETRY

CYTOMETRY Journal of Quantitative Cell Science PART A

# Comprehensive phenotyping of hematopoietic stem and progenitor cells in the human fetal liver

Kim Vanuytsel[1,2] | Anthony K. Yeung[2] | Todd W. Dowrey[2] | George J. Murphy[1,2] | Anna C. Belkina[3,4]

[1]Section of Hematology and Medical Oncology, School of Medicine, Boston University, Boston, Massachusetts, USA

[2]Center for Regenerative Medicine (CReM), Boston University and Boston Medical Center, Boston, Massachusetts, USA

[3]Flow Cytometry Core Facility, Boston University School of Medicine, Boston, Massachusetts, USA

[4]Department of Pathology and Laboratory Medicine, Boston University School of Medicine, Boston, Massachusetts, USA

**Correspondence**
Anna C. Belkina, Flow Cytometry Core Facility, Boston University School of Medicine, Boston, MA, USA.
Email: belkina@bu.edu

**Funding information**
Boston University

## Abstract

Hematopoietic stem cells (HSCs) reside at the top of the hematopoietic hierarchy and can give rise to all the mature blood cell types in our body, while at the same time maintaining a pool of HSCs through self-renewing divisions. This potential is reflected in their functional definition as cells that are capable of long-term multi-lineage engraftment upon transplantation. While all HSCs meet these criteria, subtle differences exist between developmentally different populations of these cells. Here we present a comprehensive overview of traditional and more recently described markers for phenotyping HSCs and their downstream progeny. To address the need to assess the growing number of surface molecules expressed in various HSC-enriched fractions at different developmental stages, we have developed an extensive multi-parameter spectral flow cytometry panel to phenotype hematopoietic stem and multipotent progenitor cells (HSC/MPPs) throughout development. In this study we then employ this panel to comprehensively profile the HSC compartment in the human fetal liver (FL), which is endowed with superior engraftment potential compared to postnatal sources. Spectral cytometry lends an improved resolution of marker expression to our comprehensive approach, allowing to extract combinatorial expression signatures of several relevant HSC/MPP markers to precisely characterize the HSC/MPP fraction in a variety of tissues.

**KEYWORDS**
flow cytometry, hematopoiesis, hematopoietic stem cells, immunophenotyping panel, spectral cytometry

## 1 | INTRODUCTION

HSCs have the capacity to reconstitute the entire hematopoietic system of a host. This remarkable regenerative potential has led to their use in existing and emerging therapies for a variety of disorders. In the clinic, HSCs can be isolated from the bone marrow (BM), from peripheral blood upon mobilization or from cord blood (CB). While less accessible for transplantation purposes, prenatal HSCs such as those residing in the fetal liver (FL) hold valuable information for the optimization of this process. During hematopoietic development, newly emerged HSCs travel to the FL where they expand in number before migrating to their final niche in the bone marrow [1, 2]. Despite undergoing active expansion, FL HSCs display superior engraftment potential compared to CB or BM HSCs [3]. Therefore, studying this prenatal HSC source can provide insights into how to retain or even increase the engraftment potential of postnatal HSCs. The panel described in this report was designed to phenotype the FL HSC fraction as part of a multi-modal profiling effort to establish the molecular signature of engraftment capacity [4]. While it is illustrated here in the context of the FL, the selection of markers included in this panel makes it a valuable resource for the characterization of HSC subsets in other tissues and at various developmental time points.

 

**TABLE 1** Multiparameter spectral cytometry panel used in the current study

| Markers | Conjugate | Clone | Reagent notes | Vendor | Cat. # | Reagent dilution | Unmixing control |
|---|---|---|---|---|---|---|---|
| CD45 | BUV395 | HI30 | Pan-hematopoietic marker | BD | 563791 | 100 | Lymphocytes |
| Livedead | Live Dead Blue | n/a | Live dead discrimination | Thermo Fisher | L34961 | 800 | Live+dead cells |
| CD66c | BUV661 | B1.1/CD66 | Granulocyte lineage | BD | 741653 | 50 | Beads |
| CD19 | BUV737 | SJ25C1 | B cells | BD | 612757 | 100 | Beads |
| CD14 | BUV805 | M5E2 | Monocytes | BD | 612902 | 50 | Beads |
| CD90 | BV421 | 5E10 | HSC/MPP | Biolegend | 328121 | 50 | Lymphocytes |
| CD235a | BV480 | 104 | Erythroid cells | BD | 746358 | 400 | Erythrocytes |
| CD10 | BV510 | S7 | Lymphocyte precursors | Biolegend | 312219 | 50 | CD3 BV510 lymphocytes |
| CD33 | BV570 | M17 | Myeloid cells | Biolegend | 303417 | 400 | Beads |
| CD38 | BV605 | HIT2 | Lymphocyte/monocyte marker; alternative clone HB-7 failed in CiTE-seq pilot | Biolegend | 303532 | 50 | Beads |
| CD49f | BV650 | GoH3 | HSC/MPPs | BD | 563706 | 200 | Beads |
| CD45RA | BV711 | HI100 | Naïve lymphocytes | Biolegend | 304137 | 100 | Lymphocytes |
| CD56 | BV786 | NCAM16.2 | Natural killers; alternative clone HCD56 fails to resolve high and medium positive populations in PBMCs | BD | 564058 | 100 | Lymphocytes |
| CD164 | FITC | 67D2 | HSC/MPPs | Biolegend | 324805 | 50 | Beads |
| CD3 | Spark Blue 550 | SK7 | T cells | Biolegend | 344851 | 100 | Beads |
| CD41 | PerCP-Cy55 | HIP8 | Megakaryocytes/platelets | Biolegend | 303719 | 100 | Lymphocytes |
| GPI-80 | PE | 3H9 | HSC/MPPs | MBL | D087-5 | 50 | Beads |
| CD133 | PE-Dazzle 594 | clone 7 | HSC/MPPs | Biolegend | 372811 | 100 | Beads |
| CD69 | PE-Cy5 | FN50 | HSC/MPPs or lymphocyte activation | Biolegend | 310907 | 25 | Beads |
| CD34 | PE-Cy7 | 581 | HSC/MPPs; this clone is compatible with magnetic isolation of the CD34+ enriched fraction | Biolegend | 343515 | 100 | Fetal liver |
| CD201 (EPCR) | APC | RCR-401 | HSC/MPPs | Biolegend | 351906 | 25 | CD8 APC lymphocytes |
| CD42b | Alexa 700 | HIP1 | Megakaryocytes/platelets | Biolegend | 303927 | 25 | Lymphocytes |

**TABLE 2** Surface expression profiles for markers used to identify HSC and PBMC cells in the current study

| | CD45 | CD66c | CD19 | CD14 | CD90 | CD235a | CD10 | CD33 | CD38 | CD49f | CD45RA | CD56 | CD164 | CD3 | CD41 | GPI-80 | CD133 | CD69 | CD34 | CD201 | CD42b |
|---|---|---|---|---|---|---|---|---|---|---|---|---|---|---|---|---|---|---|---|---|---|
| T cells | + | − | − | − | +/− | − | | − | +/− | +/− | +/− | +/− | − | + | − | − | − | +/− | − | − | − |
| B cells | + | − | + | − | − | − | | − | +/− | − | + | − | − | − | − | − | +/− | − | − | − | − |
| Monocytes | + | − | − | + | − | − | | + | +/− | +/− | +/− | − | + | − | +/− | +/− | − | − | − | − | − |
| Natural killers | + | − | − | − | − | − | | − | +/− | − | + | +/++ | − | − | − | − | − | +/− | − | − | − |
| Erythroid cells | − | − | − | − | − | + | | − | − | − | − | − | − | − | − | − | − | − | − | − | − |
| Granulocytes | + | + | − | − | +/− | − | | − | − | − | − | − | − | − | − | + | − | − | − | − | − |
| Lymphocyte precursors | + | − | − | − | − | − | + | − | +/− | − | +/− | − | − | − | − | − | − | +/− | − | − | − |
| Megakaryocytes | − | − | − | − | − | − | | − | − | + | − | − | +/− | − | + | − | − | +/− | + | + | + |
| Platelets | − | − | − | − | − | − | | − | − | + | − | − | +/− | − | + | − | − | +/− | − | +/− | + |
| HSC/MPPs | − | +/− | − | − | +/− | − | − | +/− | +/− | +/− | +/− | − | +/− | − | − | +/− | +/− | +/− | +/− | +/− | − |

## 2 | COMPREHENSIVE MARKER PALETTE FOR BROAD HSC CHARACTERIZATION

CD34 is traditionally used as a positive marker to denote the HSC population and is central to most HSC phenotyping and enrichment strategies as its expression marks the vast majority of HSC/MPPs. The CD34+ hematopoietic fraction, however, is heterogeneous and represents a broad collection of hematopoietic stem and progenitor cells including cells that are not imbued with engraftment potential. Further distinction between HSC/MPPs and more committed hematopoietic progenitors is guided by the expression of markers such as CD38, CD45RA and markers specific to the different mature blood cell lineages (lin). In general, there exists a consensus that the most primitive hematopoietic progenitors can be found in the CD34+ [5], lin-[6, 7], CD38− [8], CD45RA− [9], CD90+ [7] fraction [10]. However, this combination of markers is not absolute as long-term repopulating activity has also been reported in the CD90− HSC/MPP fraction, albeit at a lesser frequency [11]. Moreover, CD38 expression is variable between donors and gating can be arbitrary as there is no consensus on a cut-off for CD38− primitive cells [12, 13]. Sialomucin or CD164, has been suggested as an alternative to CD38-based gating strategies in HSC transplantation settings [13] and we have included this marker in our panel. CD69, while typically referred to as a lymphocyte activation marker [14], recently has been described as marking a transient population of mid-gestation HSC/MPPs [15] and thus might provide some insight into the developmental staging.

In addition to these relatively broad positive and negative selection markers, we also propose the use of more specific HSC enrichment markers to expand our phenotyping panel. CD49f has been reported as a highly specific marker for HSCs, with the capacity to enrich HSCs to a purity of ∼10% (1 in 10.5 cells) when added to the aforementioned selection scheme [11]. Originally described in CB, this marker is also expressed on BM HSCs [16] and FL HSCs [4] and is a common addition to HSC enrichment panels. Another powerful HSC enrichment scheme that has recently been described is driven by CD133 and GPI-80 expression [17]. CD133 surface expression is known to mark uncommitted HSCs from FL to BM [18–20] and GPI-80 expression specifically marks self-renewing HSCs in the FL [21]. The combination of these (18lin-CD34+CD38-CD133+GPI-80+) resulted in the purification of CB HSCs to the level of ∼1/5 cells [17]. CD201, also known as endothelial protein C receptor (EPCR), presents another marker with potent HSC enrichment potential. First described to mark mouse HSCs [22], CD201 was later reported to also mark human HSCs in both CB [23] and FL [24]. Assessment of CD201 expression at different developmental time points revealed that unlike in mice where its expression remains stable throughout development, the percentage of cells that are CD201+ declines over time and few CD201− expressing cells can be found in adult BM [24]. Integration of transcriptomic and cell surface level data obtained from the multimodal profiling of FL HSCs revealed that CD201 marks a subset of cells with the highest engraftment potential in the FL and transplantation experiments in the context of this work suggested that the

engraftable HSC enrichment capacity of CD201 parallels or even exceeds that of GPI-80 [4].

In our panel design, we have assigned the HSC/MPP markers to fluorochromes with as little spillover among each other as possible since we expected unpredictable patterns of co-expression of these molecules as well as a variety of expression levels (Table 1). The panel design has been optimized in several iterations to eliminate artifacts that were observed due to spillover. Clone selection was informed by the consensus in the field as well as data generated previously [4].

We have included an extensive list of lineage-specific markers in our phenotyping panel. HSC phenotyping usually assumes the use of "lineage exclusion," and a routine approach is to combine multiple antibody specificities within one "dump" fluorescence channel by using same fluorochrome conjugates or conjugates with similar emission spectra. This technique accommodates larger marker sets when the parameter capacity is limited. However, many of those markers are not exclusively expressed on committed lineages and this solution carries a risk of excluding HSC/MPPs with ectopic expression of traditional 'lineage' markers. For instance, CD45 is used as a marker for immune populations in general, but its expression can also be found, to a lower extent, on progenitors. Also, the varying ranges of expression, when combined in one channel of detection, often presents a difficulty in "gating"/subsetting the lineage negative fraction. Since we employed a five laser spectral cytometry system, we were not limited by parameter capacity and assigned all lineage markers to individual fluorochromes. To map the lineages of committed hematopoietic cells, we used CD45 (pan-hematopoetic marker), CD3 (T cells), CD56 (NK cells), CD19 (B cells), CD33 (monocytes), CD14 (monocytes), CD66c (granulocytes), CD10 (ProB progenitors), CD42b (platelets), CD41 (platelets), and CD235a (erythroid cells), summarized in Table 2 [25–27].

To illustrate the performance of our proposed phenotyping setup, we have stained CD34+ enriched human fetal liver cells as well as human adult PBMCs with our 22-color spectral panel and acquired the data on a 5 L Cytek Aurora analyzer (Cytek Biosciences). Cell isolation, staining and data acquisition were performed as reported previously [4, 25] (see Supplemental Material for details) and data were analyzed in OMIQ cloud platform. Both samples were concatenated, all immunophenotyping fluorescence parameters were dimensionally reduced into a UMAP space and clustered using Phenograph algorithm. The PBMC datapoints served as landmarks that helped to visualize commitment trajectories of FL cells in the same UMAP space (Figure 1A). Phenograph clustering identified 39 clusters in the concatenated samples (Figure 2A), most of which were exclusive to

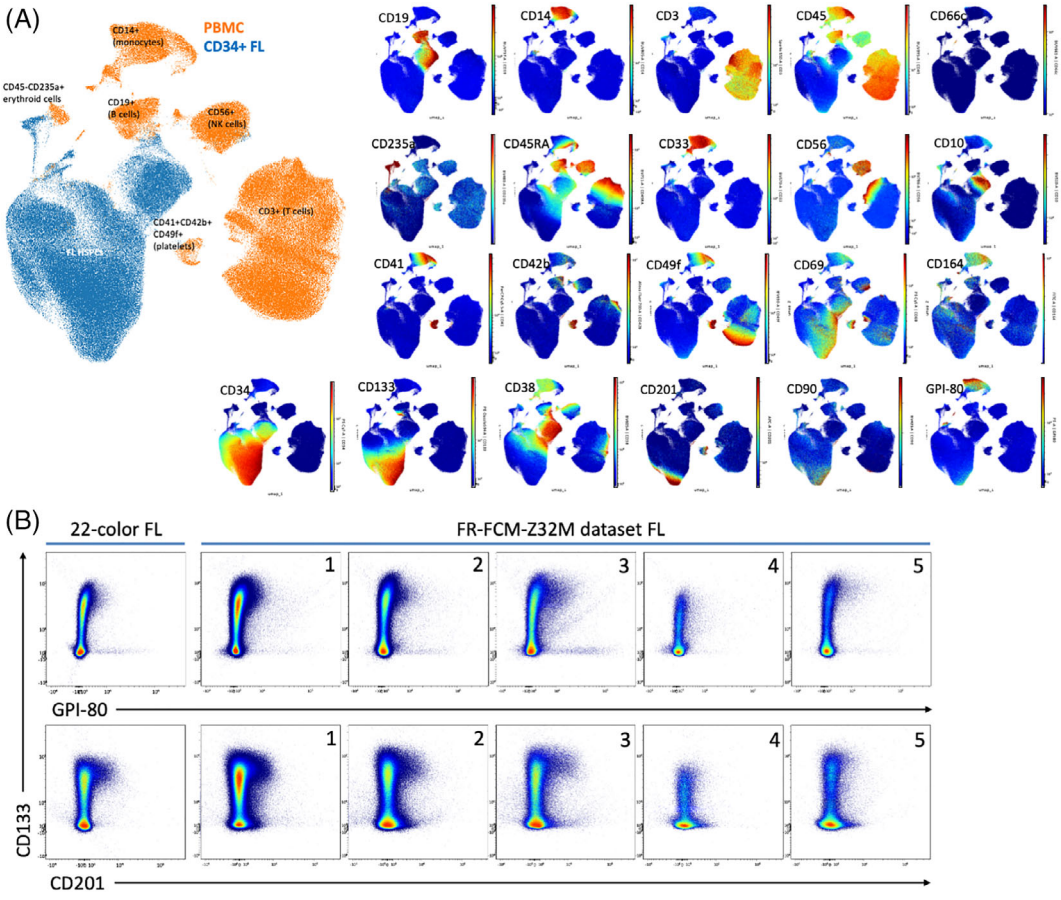


**FIGURE 1** Twenty-two-color spectral cytometry immunophenotyping of human fetal liver HSC/MPP cells. (A) UMAP projections of PBMC and FL samples labeled with 22 color spectral cytometry panel. Expression levels of tested surface markers is shown as heatmaps overlaid on the UMAP plot depicting live, single cells or platelets. (B) Bivariate plots showing expression of CD133, GPI-80 and CD201 in FL sample stained with 22-color panel (left panel) or previously reported [4] FL phenotypes (same reagents used for the depicted markers)

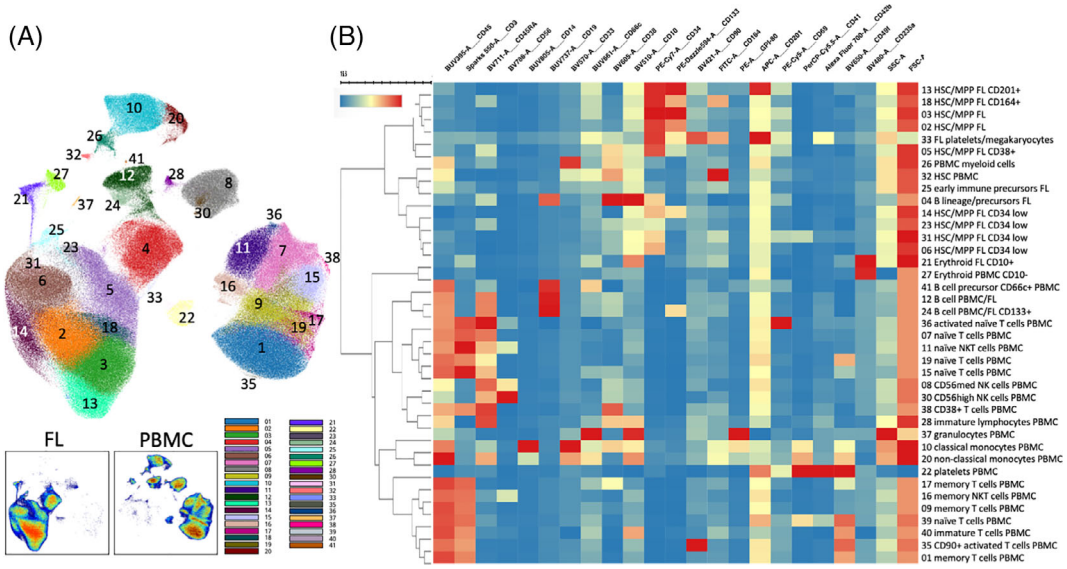


**FIGURE 2** Human fetal liver HSC/MPP population landscape. (A) Marker expression Phenograph clustering overlaid on UMAP plot depicting live, single cells or platelets. Insets at the bottom illustrate the distinction between FL cells and PBMCs. The latter were included to visualize commitment trajectories of FL cells in the same UMAP space. (B) Heatmap visualization of normalized expression levels of tested markers on Phenograph clusters defined from live, single cells or platelets. Unsupervised hierarchical clustering of the cell clusters in the heatmap is depicted by the dendrogram on the *left*. All expression level intensities are normalized per column

one of the sample types, but others contained cells from both sources. In Figure 2B, representing a clustered heatmap of the median marker expression across clusters, we have marked the predominant, but not exclusive, source of cells for each cluster. It is important to note that there may exist sample-to-sample variability of marker expression across FL specimens, and our 22-color dataset only represents a single FL sample. When compared with the dataset collected with the early version of our panel (available as FR-FCM-Z32M Flow Repository public dataset) that contains 5 FL specimens, the ratios of certain populations may vary across samples; for instance, the GPI-80+ CD133+ and CD201+ CD133+ cell subsets proportions differ across the specimens (Figure 1B and [4]). However, qualitatively the identified combinatorial phenotypes of HSC/MPP subsets exist in most samples.

Overall, we observed the expected patterns of expression of previously described markers in the HSC/MPP compartment as well as the combinatorial signatures of multiple HSC markers that have not been yet assessed in a single panel.

## 3 | CONCLUSIONS

In this report, we present a summary of current trends in phenotyping human HSC/MPPs. We provide a detailed list of surface markers to assist the study design, as well as share our 22-color spectral cytometry panel that has been designed to encompass expression of all proposed markers in a single tube assay. The HSC/MPP marker selection spans historically used HSC markers as well as more recently described alternatives for HSC enrichment. All HSC markers included in our panel are well-defined markers that have been extensively characterized in terms of enrichment capacity for cells with self-renewal and multi-lineage reconstitution potential, obviating the need to repeat functional characterization in the context of this work.

We illustrate the performance of our multi-parameter phenotyping panel on CD34+ enriched human fetal liver cells, creating a dataset that serves as an example of marker distribution across the human HSC/MPP continuum at this developmental stage.

Importantly, the spectral cytometry panel described here allows for the characterization of HSCs in different tissues, ranging in location and developmental time, and can easily be expanded to accommodate alternative/newly discovered HSC/MPP markers, or incorporate additional markers to profile non-conventional HSC sources.

### ACKNOWLEDGMENTS

This work has been supported by the BUSM Flow Cytometry Core Facility. The CD34+ enriched fetal liver cells were kindly provided by Dr. Alejandro B. Balazs. We thank Dr. Vladimir Vrbanac for assistance with fetal liver cell preparation.

This project has been funded from CReM internal sources (Boston University).

### AUTHOR CONTRIBUTIONS

**Kim Vanuytsel:** Conceptualization (equal); investigation (lead); methodology (equal); resources (equal); writing – original draft (lead); writing – review and editing (equal). **Anthony K Yeung:** Investigation (supporting); writing – review and editing (supporting). **Todd W Dowrey:** Investigation (supporting); writing – review and editing (supporting). **George J Murphy:** Conceptualization (supporting); resources (lead); writing – review and editing (supporting). **Anna C**

**Belkina:** Conceptualization (supporting); investigation (equal); methodology (lead); resources (supporting); software (lead); visualization (lead); writing – original draft (equal); writing – review and editing (lead).

## CONFLICT OF INTEREST

The authors declare no competing interests.

## PEER REVIEW

The peer review history for this article is available at https://publons.com/publon/10.1002/cyto.a.24540.

## ORCID

*Kim Vanuytsel* https://orcid.org/0000-0002-8872-0736
*Anthony K. Yeung* https://orcid.org/0000-0002-9373-7479
*Todd W. Dowrey* https://orcid.org/0000-0001-6086-6306
*George J. Murphy* https://orcid.org/0000-0003-3464-793X
*Anna C. Belkina* https://orcid.org/0000-0001-7967-6254

## REFERENCES

1. Mikkola HK, Orkin SH. The journey of developing hematopoietic stem cells. Development. 2006;133(19):3733–44.
2. Palis J, Yoder MC. Yolk-sac hematopoiesis: the first blood cells of mouse and man. Exp Hematol. 2001;29(8):927–36.
3. Holyoake TL, Nicolini FE, Eaves CJ. Functional differences between transplantable human hematopoietic stem cells from fetal liver, cord blood, and adult marrow. Exp Hematol. 1999;27(9):1418–27.
4. Vanuytsel K, Villacorta-Martin C, Lindstrom-Vautrin J, Wang Z, Garcia-Beltran WF, Vrbanac V, et al. Multi-modal profiling of human fetal liver-derived hematopoietic stem cells reveals the molecular signature of engraftment potential. Nat Commun. 2022;13:1103. https://doi.org/10.1038/s41467-022-28616-x
5. Civin CI, Strauss LC, Brovall C, Fackler MJ, Schwartz JF, Shaper JH. Antigenic analysis of hematopoiesis. III. A hematopoietic progenitor cell surface antigen defined by a monoclonal antibody raised against KG-1a cells. J Immunol. 1984;133(1):157–65.
6. Bhatia M, Wang JCY, Kapp U, Bonnet D, Dick JE. Purification of primitive human hematopoietic cells capable of repopulating immune-deficient mice. Proc Natl Acad Sci U S A. 1997;94(10):5320–5.
7. Baum CM, Weissman IL, Tsukamoto AS, Buckle AM, Peault B. Isolation of a candidate human hematopoietic stem-cell population. Proc Natl Acad Sci USA. 1992;89(7):2804–8.
8. Terstappen LW, Huang S, Safford M, Lansdorp PM, Loken MR. Sequential generations of hematopoietic colonies derived from single nonlineage-committed CD34+CD38- progenitor cells. Blood. 1991;77(6):1218–27.
9. Lansdorp PM, Sutherland HJ, Eaves CJ. Selective expression of CD45 isoforms on functional subpopulations of CD34+ hemopoietic cells from human bone marrow. J Exp Med. 1990;172(1):363–6.
10. Majeti R, Park CY, Weissman IL. Identification of a hierarchy of multipotent hematopoietic progenitors in human cord blood. Cell Stem Cell. 2007;1(6):635–45.
11. Notta F, Doulatov S, Laurenti E, Poeppl A, Jurisica I, Dick JE. Isolation of single human hematopoietic stem cells capable of long-term multilineage engraftment. Science. 2011;333(6039):218–21.
12. Masiuk KE, Brown D, Laborada J, Hollis RP, Urbinati F, Kohn DB. Improving gene therapy efficiency through the enrichment of human hematopoietic stem cells. Mol Ther. 2017;25(9):2163–75.
13. Pellin D, Loperfido M, Baricordi C, Wolock SL, Montepeloso A, Weinberg OK, et al. A comprehensive single cell transcriptional landscape of human hematopoietic progenitors. Nat Commun. 2019;10(1):2395.
14. Ziegler SF, Ramsdell F, Alderson MR. The activation antigen CD69. Stem Cells. 1994;12(5):456–65.
15. Li H, Ezike J, Afanassiev A, Greenstreet L, Zhang S, Whangbo J, et al. Hematopoiesis at single cell resolution spanning human development and maturation. bioRxiv. 2021;457678.
16. Velten L, Haas SF, Raffel S, Blaszkiewicz S, Islam S, Hennig BP, et al. Human haematopoietic stem cell lineage commitment is a continuous process. Nat Cell Biol. 2017;19(4):271–81.
17. Sumide K, Matsuoka Y, Kawamura H, Nakatsuka R, Fujioka T, Asano H, et al. A revised road map for the commitment of human cord blood CD34-negative hematopoietic stem cells. Nat Commun. 2018;9(1):2202.
18. Yin AH, Miraglia S, Zanjani ED, Almeida-Porada G, Ogawa M, Leary AG, et al. AC133, a novel marker for human hematopoietic stem and progenitor cells. Blood. 1997;90(12):5002–12.
19. Takahashi M, Matsuoka Y, Sumide K, Nakatsuka R, Fujioka T, Kohno H, et al. CD133 is a positive marker for a distinct class of primitive human cord blood-derived CD34-negative hematopoietic stem cells. Leukemia. 2014;28(6):1308–15.
20. Bhatia S, Reister S, Mahotka C, Meisel R, Borkhardt A, Grinstein E. Control of AC133/CD133 and impact on human hematopoietic progenitor cells through nucleolin. Leukemia. 2015;29(11):2208–20.
21. Prashad SL, Calvanese V, Yao CY, Kaiser J, Wang Y, Sasidharan R, et al. GPI-80 defines self-renewal ability in hematopoietic stem cells during human development. Cell Stem Cell. 2015;16(1):80–7.
22. Balazs AB, Fabian AJ, Esmon CT, Mulligan RC. Endothelial protein C receptor (CD201) explicitly identifies hematopoietic stem cells in murine bone marrow. Blood. 2006;107(6):2317–21.
23. Fares I, Chagraoui J, Lehnertz B, MacRae T, Mayotte N, Tomellini E, et al. EPCR expression marks UM171-expanded CD34(+) cord blood stem cells. Blood. 2017;129(25):3344–51.
24. Subramaniam A, Talkhoncheh MS, Magnusson M, Larsson J. Endothelial protein C receptor (EPCR) expression marks human fetal liver hematopoietic stem cells. Haematologica. 2019;104(2):e47–50.
25. Park LM, Lannigan J, Jaimes MC. OMIP-069: forty-color full Spectrum flow cytometry panel for deep Immunophenotyping of major cell subsets in human peripheral blood. Cytometry A. 2020;97(10):1044–51.
26. O'Byrne S, Elliott N, Rice S, Buck G, Fordham N, Garnett C, et al. Discovery of a CD10-negative B-progenitor in human fetal life identifies unique ontogeny-related developmental programs. Blood. 2019;134(13):1059–71.
27. Bianca Bennstein S, Riccarda Manser A, Weinhold S, Scherenschlich N, Uhrberg M. OMIP-055: characterization of human innate lymphoid cells from neonatal and peripheral blood. Cytometry A. 2019;95(4):427–30.

## SUPPORTING INFORMATION

Additional supporting information may be found in the online version of the article at the publisher's website.

Received: 21 December 2020 | Revised: 31 May 2021 | Accepted: 7 June 2021

DOI: 10.1002/cyto.a.24472

ORIGINAL ARTICLE

MIFlowCyt

ISAC INTERNATIONAL SOCIETY FOR ADVANCEMENT OF CYTOMETRY

CYTOMETRY Journal of Quantitative Cell Science PART A

# Detecting Förster resonance energy transfer in living cells by conventional and spectral flow cytometry

Jared Henderson[1] | Ondrej Havranek[1,2,3] | Man Chun John Ma[1] | Vaclav Herman[2,3] | Kristyna Kupcova[2] | Tereza Chrbolkova[2] | Mariana Pacheco-Blanco[2] | Zhiqiang Wang[1] | Justin M. Comer[1] | Tomasz Zal[4] | Richard Eric Davis[1,5]

[1]Department of Lymphoma and Myeloma, The University of Texas-MD Anderson Cancer Center, Houston, Texas, USA

[2]BIOCEV, First Faculty of Medicine, Charles University, Vestec, Czech Republic

[3]Department of Hematology, Charles University and General University Hospital, Prague, Czech Republic

[4]Department of Leukemia, The University of Texas-MD Anderson Cancer Center, Houston, Texas, USA

[5]Department of Translational Molecular Pathology, The University of Texas-MD Anderson Cancer Center, Houston, Texas, USA

**Correspondence**
Ondrej Havranek, BIOCEV and Department of Hematology, First Faculty of Medicine, Charles University, Czech Republic, Prumyslova 595, 25250 Vestec, Czech Republic.
Email: ondrej.havranek@lf1.cuni.cz

Richard Eric Davis, Department of Lymphoma and Myeloma, The University of Texas-MD Anderson Cancer Center, Box 903, SCR1.2015, 7455 Fannin Street, Houston, TX 77054, USA.
Email: redavis1@mdanderson.org

**Funding information**
University of Texas-MD Anderson Cancer Center, Grant/Award Number: Moon Shots Program in B-cell Lymphoma; National Cancer Institute, Grant/Award Numbers: RR029552, S10; MD Anderson Cancer Center, Grant/Award Numbers: CA16672, P30; Czech Health Research Council: NV18-03-00117; Charles University, Grant/Award Numbers: SVV 260374, UNCE/MED/016, Progres Q26, SVV 260374

## Abstract

Assays based on Förster resonance energy transfer (FRET) can be used to study many processes in cell biology. Although this is most often done with microscopy for fluorescence detection, we report two ways to measure FRET in living cells by flow cytometry. Using a conventional flow cytometer and the "3-cube method" for intensity-based calculation of FRET efficiency, we measured the enzymatic activity of specific kinases in cells expressing a genetically-encoded reporter. For both AKT and protein kinase A, the method measured kinase activity in time-course, dose–response, and kinetic assays. Using the Cytek Aurora spectral flow cytometer, which applies linear unmixing to emission measured in multiple wavelength ranges, FRET from the same reporters was measured with greater single-cell precision, in real time and in the presence of other fluorophores. Results from gene-knockout studies suggested that spectral flow cytometry might enable the sorting of cells on the basis of FRET. The methods we present provide convenient and flexible options for using FRET with flow cytometry in studies of cell biology.

**KEYWORDS**
cell-based reporter assay, flow cytometry, FRET, kinase assay, protein kinase A, protein kinase B/AKT, spectral flow cytometry

## 1 | INTRODUCTION

Förster resonance energy transfer (FRET) between fluorophores depends on several factors, the most dynamic of which is their

Jared Henderson and Ondrej Havranek contributed equally to this study.

 

proximity and geometrical orientation. This property is the basis for the many assays in which FRET provides the readout for a molecular or biological phenomenon (1, 2). FRET-based assays have many attractive features, but their utility in practice depends on the ease and sensitivity of FRET detection and the accuracy with which FRET can be measured. FRET is most commonly measured by its effect on donor and acceptor fluorescence intensities, since this approach is compatible with commonly-available instrumentation. FRET can also be detected by fluorescence lifetime and polarization-based methods, which offer certain advantages but require more specialized instrumentation. Fluorescence microscopy has been used most extensively to measure FRET in cells, with the advantages of providing subcellular localization and enabling the use of photobleaching for FRET validation, measurement, or calibration. However, microscopy has relatively low throughput regarding the number of cells or samples that can be assessed, and its requirement for cells to be immobilized (or nearly so) prevents certain potential applications of FRET assays in cells.

Conventional flow cytometry (FCM) provides a higher-throughput alternative approach for detecting FRET in cells. FCM measures per-cell fluorescence emission from thousands of cells per second, in a certain number of channels optimized for commonly used fluorophores and defined by laser excitation and filter-set optical detection wavelength ranges. With a laser that largely excites the donor fluorophore but not the acceptor, FRET causes a relative reduction of fluorescence intensity in the donor's characteristic fluorescence emission range (donor quenching), accompanied by increased emission in the range of wavelengths attributable to the acceptor (sensitized acceptor emission). The user can compare the intensity of acceptor-range emission ($I_{DA}$) to donor-range emission ($I_{DD}$) per cell in real time after donor excitation, graphically using a $I_{DA}/I_{DD}$ "dot plot" or a "FRET ratio" ($I_{DA}/I_{DD}$) histogram. However, this manner of FRET detection in FCM suffers from non-linearity (3), is affected by the abundance of the acceptor, and varies with other factors that make it "instrument-dependent".

FRET efficiency ($E$) is an absolute measure of FRET that is instrument-independent, corresponding to the proportion of donor excitation events that were quenched by energy transfer to the acceptor. As first reported by Zal et al. (4) for microscopy, the "3-cube method" calculates $E$ from $I_{DD}$, $I_{DA}$, and the intensity of acceptor-range emission after acceptor excitation ($I_{AA}$), after correcting for the spectral cross-talk, or bleedthrough, and calibrating the instrument in terms of a $G$ parameter. Essentially the same approach has been reported to provide reliable determinations of $E$ from FCM measurements (5, 6); more elaborate channel bleedthrough correction procedures have recently been reported (7, 8). However, calculation of $E$ is only done after data have been acquired, limiting real-time assessment of FRET by FCM to use of the FRET ratio.

"Spectral" techniques measure fluorescence emission in far more channels (wavelength ranges) than the number of fluorophores under detection, and a characteristic "spectral fingerprint" is defined for each fluorophore. When multiple fluorophores are present simultaneously, spectral "unmixing" algorithms use these fingerprints to determine the contribution of each fluorophore to the total fluorescence, and thus their abundance. Spectral microscopy has been used for intensity-based determination of FRET (9–12), but through post-acquisition data analysis. Spectral flow cytometry (SFCM) has become popular in recent years for the advantages that it provides in sensitivity and the simultaneous use of multiple fluorophores (13, 14), but the detection of FRET by SFCM has not previously been reported.

Among genetically-encoded biosensors based on FRET (15), those that report on the enzymatic activity of protein kinases are widely used and offer several advantages (16, 17). We previously reported our use of FCM with a FRET-based reporter to measure AKT kinase activity (18). We report here further optimization of the AKT activity reporter, and demonstration of its use with FCM for time-course, dose–response, and kinetic studies. We also show the flexibility of the assay, by changing the reporter's target peptide to be specific for protein kinase A. Finally, we show that SFCM can detect changes in the reporter's FRET, by unmixing based on the spectral fingerprints of low-FRET and high-FRET controls.

## 2 | MATERIALS AND METHODS

### 2.1 | Three-channel detection of FRET by FCM

For FRET determination by FCM on an LSRFortessa flow cytometer (BD Biosciences), filters were chosen with respect to Cerulean3, the donor fluorophore used in all studies (C3; peak excitation and emission wavelengths, 433 and 475 nm), and the acceptor circularly-permuted cpVenus[E172] (cpV; peak excitation and emission wavelengths, 515 and 528 nm). Donor fluorescence with donor excitation ($I_{DD}$, donor channel) was measured with a 405 nm laser and 480/40 filter; acceptor emission with donor excitation ($I_{DA}$, FRET channel) was measured with a 405 nm laser and 550/49 filter; and acceptor emission with acceptor excitation ($I_{AA}$, acceptor channel) was measured with a 488 nm laser and 530/30 filter. FRET was also determined on a different LSRFortessa flow cytometer using more typical filter sets: a 405 nm laser and 450/50 filter for $I_{DD}$ measurement, a 405 nm laser and 525/50 filter for $I_{DA}$ measurement, and a 488 nm laser and 530/30 filter for $I_{AA}$ measurement.

For the fluorophores and flow cytometer used (including its filters and settings), calibration was based on methods developed by Zal et al. (4) with subsequent modification by Chen et al. (5). For each experiment, four channel cross-talk coefficients were determined from FCM measurements made on cells of a single cell line (OCI-Ly7) expressing control constructs: $a$ ($I_{DA}/I_{AA}$) and $b$ ($I_{DD}/I_{AA}$) were determined from cells expressing only cpV, while $c$ ($I_{AA}/I_{DD}$) and $d$ ($I_{DA}/I_{DD}$) were determined from cells expressing only C3. Each coefficient was determined as the slope of the regression line of event fluorescence for the appropriate combination of channels, using data from single fluorophore-expressing control cells mixed with non-fluorescent OCI-Ly7 cells (to establish the graphical origin), after first subtracting the average intensity of autofluorescence of unmodified cells in each channel. The $b$ coefficient, which was relatively small on average and variable, was empirically found to be best set by default to zero.

The *G* coefficient, which relates sensitized acceptor emission to donor quenching (4, 19), was determined by using a pair of FRET controls in which C3 was fused to cpV, but with very different intramolecular proximities between the fluorophores and therefore high differences in *E*. A rigid 230-amino acid linker from TRAF2 was used between C3 and cpV to create a low-FRET control, C3-TRAF2-cpV (20), while a linker-free C3-cpV fusion protein served as a high-FRET control. For each FRET control, per-cell fluorescence intensity values ($I_{DD}$, $I_{DA}$, and $I_{AA}$) were subtracted by the corresponding autofluorescence averages for unmodified cells of the same cell line, and then used to calculate the following parameters: the corrected $I_{AA}$ value, $I_{aa} = (dI_{AA} - cI_{DA})/(d - ca)$;

$I_{dd} = (aI_{DD} - bI_{DA})/(a - bd)$, simplified in practice as $I_{DD}$, given $b = 0$; and sensitized acceptor emission, $F_c = I_{DA} - aI_{aa} - dI_{dd}$.

From a plot of $F_C$ versus $I_{dd}$ for each control, events in the middle range of $I_{dd}$ (displaying linearity) were selected for calculation of average values of $F_C$, $I_{dd}$, and $I_{aa}$. These were then used to calculate the *G* coefficient, by the following equation: (5)

$G = [(F_{c2}/I_{aa2}) - (F_{c1}/I_{aa1})]/[(I_{dd1}/I_{aa1}) - (I_{dd2}/I_{aa2})]$ in which 1 and 2 are respectively the high-FRET and low-FRET controls.

For determination of FRET efficiency (*E*) in samples, FlowJo software was used to select events with $I_{AA}$ fluorescence levels above that of unmodified autofluorescent control cells of the parental cell line, then auto-gating in FlowJo software was used to eliminate outlier events with fluorescence values <1.5 *SD* from the mean in an orthogonal $I_{DD}$ versus $I_{AA}$ plot. Then, for all samples expressing reporter constructs for kinase activity, average autofluorescence values were subtracted from per-cell fluorescence intensity values ($I_{DD}$, $I_{DA}$, and $I_{AA}$) as above, which were then used for calculation of $F_C$ and $I_{dd}$, followed by calculation of a per-cell *E* value using *G* in the following equation: $E = F_c/(GI_{dd} + F_c)$ (5).

Single-cell *E* values for each sample were plotted as a moving median of *E* versus $I_{AA}$. A single average overall *E* value for each sample was calculated, using cells in the same range of reporter emission intensities for all comparable samples. For kinetic measurements of *E*, the average of single cell *E* values in a selected $I_{AA}$ range was plotted versus time.

## 2.2 | Software for FRET data processing

A software package "fRet" was written in the R language to optimize the processing of FCM data. A detailed user's manual, provided as Data S2, illustrates primary FCM data and provides guidance for selecting events for calculations in *E* determination. The software package itself is available on request from the authors, along with sample data for user practice. In brief, the process of analysis starts by applying light scatter gates with standard analysis software (e.g., FlowJo) to FCM data in .fcs files to identify live single cells expressing the reporter or control construct. Raw event values for each measured sample are then exported into a .csv file, one for each sample, which can be directly used for calculations with the software. Individual coefficients necessary for *E* determination are calculated using control samples described above, including plotting of individual graphs ($I_{DA}$ vs. $I_{AA}$ for acceptor single control, $I_{AA}$ vs. $I_{DD}$ and $I_{DA}$ vs. $I_{DD}$ for donor single control, and $F_C$ vs. $I_{dd}$ for FRET high and low controls) for quality control. The actual *E* values for FRET high and low controls are also calculated, for comparison to expected values or values from previous experiments. For experimental samples, the moving median of *E* versus $I_{AA}$ is calculated for each analyzed sample based on defined values for window step and width; results are plotted and written as a .csv file, providing a single average value of *E* within the selected $I_{AA}$ range. For kinetic mode analysis, the average *E* values within the defined $I_{AA}$ range are plotted versus time and results also written as .csv files.

## 2.3 | FRET detection by SFCM

We used an Aurora spectral flow cytometer (Cytek Biosciences; configuration 4 L 16 V-14B-10YG-8R) with standard technical features (https://f.hubspotusercontent00.net/hubfs/6765000/Website%20Downloadable%20Content/Guides%20and%20Manuals/N9_20006_B_Aurora_UG.pdf, pp. 123–4), and detection of fluorescence in 8–16 channels for each laser (Data S3, Table S1). For determination of *E* values by the three-channel method on the Aurora (also known as "3-cube" in microscopy), raw fluorescence intensity values were taken from three of its channels, most similar to the optical settings employed on the LSRFortessa: $I_{DD}$ was based on excitation with a 405 nm laser and one of its detection channels (V4, 466–481 nm), $I_{DA}$ came from the 405 nm laser channel V7 (533–550 nm), and $I_{AA}$ came from channel B3 (533–550 nm) for the 488 laser.

For assessment of FRET by spectral unmixing (SU-FRET) on the Aurora, we utilized built-in algorithms provided in SpectroFlo software, which use least-squares linear regression to calculate an intensity matrix that minimizes the difference between the experimental data and the reference spectra (spectral fingerprints) multiplied by the intensity matrix (21). Custom "FRET-Low" and "FRET-High" spectral fingerprints were created in SpectroFlo by collecting data from OCI-Ly7 cells expressing the low-FRET or high-FRET controls, respectively, and used with the spectral fingerprint of unmodified cells (autofluorescence) in unmixing of the fluorescence of cells expressing kinase activity reporter constructs. Unmixed intensities were displayed real-time in an orthogonal FRET-high versus FRET-low two-parameter plot. For experiments using additional fluorophores, reference data were added to the unmixing panel according to the SpectroFlo user guide and unmixed alongside FRET parameters as they would be for any other fluor. SpectroFlo software allows for retention of spectral signatures in a long-term spectral library, and real-time FRET unmixing gives equivalent results using same-day or stored FRET-Low and FRET-High spectra, thereby avoiding the need to collect FRET reference spectra on a per-experiment basis; in contrast, we found that achieving precise three-channel determination of *E* requires the acquisition of data from control-bearing cells on a same-day basis (data not shown).

## 3 | RESULTS

### 3.1 | Features of the AKT activity reporter construct

Protein kinases are critical mediators of many biological processes, and are therefore the subject of extensive research efforts in cell signaling and drug development. Many genetically-encoded reporters of protein kinase activity rely on FRET to reflect the phosphorylation state of a kinase target peptide domain in the reporter (16, 17). Reporter FRET is generated by two fluorescent domains in the reporter, one serving as donor and the other as acceptor; its magnitude depends on the relative proximity and orientation of these fluorophores, which in turn are affected by phosphorylation of a target peptide and its recognition by a phosphoamino acid binding domain.

AKT, also known as protein kinase B, refers to three highly homologous serine/threonine kinases that are conserved in mammalian genomes and affect many aspects of cell biology, especially in cancer (22). AktAR2 (23, 24) (Data S1, Figure S1A) is a cell-based reporter of AKT kinase activity, originally applied in fluorescence microscopy (25). The reporter's donor and acceptor fluorophores are respectively Cerulean3 (C3), a cyan variant of green fluorescent protein (GFP), and cpVenus E172 (cpV), a circularly-permuted yellow GFP variant. These are connected by a linker containing a target peptide (residues flanking Thr24 in the AKT substrate FOXO1) and the FHA1 phospho-amino acid binding domain (from yeast RAD53) (26). When the target Thr is phosphorylated by AKT, binding by FHA1 alters reporter conformation and brings the fluorophores closer together and/or into more FRET-favorable orientation. Since FRET efficiency (*E*) is increased by proximity, *E* of AktAR2 is an indicator of the degree of reporter phosphorylation, which reflects the level of AKT kinase activity.

In classical AKT activation, phosphatidylinositol (3,4,5)-trisphosphate (PIP3) generated by phosphatidylinositol 3-kinase (PI3K) isoforms binds to AKT proteins and causes their translocation to the plasma membrane, where they undergo activating phosphorylations at Ser473 (by the mTORC2 complex) and Thr308 (by PDPK1) (22). Since PIP3 has additional positive allosteric effects on AKT and is predominantly membrane-localized, AKT is principally active at membranes (27). Therefore, we modified AktAR2 by adding the 10 N-terminal amino acids from mouse Lyn kinase ("Lyn") to the N-terminus of AktAR2 (Data S1, Figure S1B), as done previously (23) to localize AktAR2 to lipid rafts. In multiple cell lines representing the germinal center subtype of diffuse large B-cell lymphoma (GCB-DLBCL), expression of Akt-AR2 and Lyn-AktAR2 produced fluorescence attributable to C3 and cpV, exclusively in either the cytoplasm or plasma membrane respectively, as expected (18). In GCB-DLBCL lines, "tonic" (antigen-independent) signaling by the B-cell receptor (BCR) contributes to activation of AKT, through PI3K and the tyrosine kinase SYK. By confocal microscopy-based measurement, *E* in two GCB-DLBCL lines was higher with membrane-targeted Lyn-AktAR2, and was lowered more in response to knockout (KO) of the BCR (Data S1, Figure S2A). Therefore, Lyn-tagged forms of AktAR2 were used for all subsequent experiments.

### 3.2 | Measuring reporter FRET by FCM

Assessed by fluorescence microscopy, *E* from the Lyn-AktAR2 reporter in GCB-DLBCL lines was decreased by BCR KO, roughly matching the degree to which BCR KO reduced their proliferation (18). However, measurement of *E* by microscopy was laborious, such that it was practical to evaluate only a limited number of cells. Especially since subcellular mapping of *E* was not needed, we used FCM to measure *E* in thousands of reporter-expressing cells. Specifically, FCM was used to measure the fluorescence intensities of each passing cell in channels spectrally optimized to detect donor or acceptor-range emissions during either donor or acceptor excitation: $I_{DD}$, $I_{AA}$, and $I_{DA}$ according to Zal et al. (4). FCM measurements from cells expressing Lyn-AktAR2 or control constructs (Data S1, Figure S1B) were processed with software (see Section 2), according to the spectral correction method of Chen et al. (5), to yield a single average value per sample. As expected, *E* values for low- and high-FRET control constructs were highly constant, regardless of the cell line in which they were expressed or the day of a particular assay (Data S1, Figure S2B and Data S3, Tables S2 and S3), even across different cytometers and PMT settings, and despite substantial variation in raw values for autofluorescence and fluorescence from controls and reporters (data not shown). Values of individual coefficients required for *E* calculation were also stable for a particular cytometer and settings (Data S3, Table S2).

### 3.3 | Further-optimized and control forms of the AKT activity reporter

To assist interpretation of *E* values from the Lyn-AktAR2 reporter, we also made a version (Lyn-AktAR2-D) with mutation of the target Thr residue (Data S1, Figure S1B) (23). *E* of this "dead", inactive (unphosphorylatable) reporter approximates what would be the *E* value of the "live" (active) Lyn-AktAR2 reporter without AKT kinase activity, providing a lower bound by which to estimate how much AKT kinase activity is reduced by BCR KO or other manipulation, and a control for non-specific effects (e.g., in drug studies; see below).

We previously found only a small positive difference between *E* values ($\Delta E$) for Lyn-AktAR2 versus Lyn-AktAR2-D in unstimulated cells of GCB-DLBCL lines (18), indicating substantial intramolecular proximity between fluorophores when the AktAR2 reporter is unphosphorylated. To increase the dynamic range of Lyn-AktAR2, we inserted a flexible "EV" linker (28) between the FHA1 and FOXO1 domains to create Lyn-AktAR2-EV, and a corresponding inactive version (Lyn-AktAR2-EV-D; Data S1, Figure S1B). EV increased the $\Delta E$ between active and inactive reporters in several GCB-DLBCL lines (Data S1, Figure S2C), and between BCR-unmodified and BCR-KO cells of SUDHL-6 with active reporters (Data S1, Figure S2D).

Several other observations regarding AktAR2-based reporters were made. Expression of the active reporter did not affect the growth of SUDHL-4 cells (Data S1, Figure S2E), suggesting that the reporters do not interfere with AKT function. *E* values for unmanipulated cells of each cell line, assayed on different days, were relatively constant for active and inactive Lyn-AktAR2-EV reporters, further showing assay precision (Data S1, Figure S3A). Reporter abundance varied greatly between cells of each reporter-expressing line, likely due to expression via a transposon vector; furthermore, for cells at any particular level of reporter abundance, FCM yielded considerable variation in per-cell *E* values. We addressed these variations by calculating *E* as a moving median ($\tilde{E}$) over the range of reporter abundance, and found that $\tilde{E}$ values of each reporter or control were relatively stable, at characteristic levels, over a wide range of $I_{AA}$ (Data S1, Figure S3B). This is consistent with theory; other than a potential increase in inter-molecular FRET with increasing reporter concentration, which appears to be negligible, and unless the underlying AKT activity is limiting, *E* should be unaffected by the reporter's cellular abundance.

To calculate a single *E* value for a particular sample, an intermediate but wide range of $I_{AA}$ with stable $\tilde{E}$ was selected, avoiding cells with reporter levels that were either very high, which might overwhelm AKT capacity, or very low, which might cause problems in background subtraction. A consistent range of $I_{AA}$ was chosen for all samples in a particular experiment, and the final single *E* value of each sample was calculated as a mean of moving median $\tilde{E}$ values in the selected $I_{AA}$ range. Applied to cells of GCB-DLBCL lines in their baseline state, this approach showed a slight increase in $\tilde{E}$ values of the Lyn-AktAR2-EV reporters with increasing $I_{AA}$ (Data S1, Figure S3B), but the active reporter's $\tilde{E}$ value was consistently higher than that of the inactive reporter across the range of $I_{AA}$.

### 3.4 | Validation of the AKT activity reporter

To verify that *E* determined by FCM with the active Lyn-AktAR2-EV reporter reflects AKT kinase activity, we performed a variety of experimental manipulations with expected effects on AKT kinase activity. Using a transposon vector with a doxycycline (Dox)-inducible promoter (29), found previously to be very non-leaky and Dox-titratable (18), we expressed a constitutively-active (myristoylated) form of murine AKT1 (MyrAKT) (18, 30). In two GCB-DLBCL lines with the active Lyn-AktAR2-EV reporter, AKT activity in cells with inducible MyrAKT was markedly increased at 48 h after Dox addition (also at 24 h; data not shown), but largely unchanged with induction of luciferase (Luc) as a control protein (Figure 1(A)).

Other manipulations involved the lipid phosphatase PTEN, which negatively regulates AKT kinase activity by hydrolyzing PIP3 to phosphatidylinositol (4,5)-bisphosphate. Stable PTEN KO increased *E* values of Lyn-AktAR2-EV in GCB-DLBCL lines (Figure 1(B)), consistent with our previous findings that it increased AKT pS473 and rescued from the effects of BCR KO (18). After additionally introducing a transposon vector for Dox-inducible PTEN re-expression in PTEN-KO cells, we found that *E* from Lyn-AktAR2-EV declined with increasing Dox concentration (Figure 1(C)), as expected.

### 3.5 | Feasibility of the AKT activity reporter assay for dose–response, time-course, and kinetic studies

Ease of use, the low numbers of cells required, and precision from averaging measurements from many cells make this assay suitable for testing dose-dependent effects on AKT kinase activity in living cells. We previously showed that clinical-grade, small-molecule inhibitors of kinases involved in AKT activation by tonic BCR signaling (P505-15 for SYK, and idelalisib for the PI3K p110δ isoform) caused dose-dependent inhibition of AKT kinase activity in GCB-DLBCL lines (18). We now performed dose–response studies of additional inhibitors of AKT and its activation, in which the inactive Lyn-AktAR2-EV reporter was useful: the baseline $\Delta E$ between active and inactive reporters (e.g., Data S1, Figure S4A) can be set as 100% AKT activity for each line (Data S1, Figures S4A and S4B), thereby facilitating the interpretation of inhibitor studies across different lines. The inactive reporter can also identify inhibitor concentrations above which *E* of both reporters is non-specifically affected (Data S1, Figure S4D).

After 1-h incubations, similar dose–response curves of two GCB-DLBCL lines were observed for two allosteric inhibitors of AKT, MK2206 (31) and AKT-VIII (SC66) (32), as well as the ATP-competitive AKT inhibitor ipatasertib (GDC-0068) (33) (Figure 1(D)). We also evaluated inhibitors of kinases respectively responsible for activating phosphorylation of AKT at residues Ser473 and Thr308: the pan-mTORC complex inhibitor MLN0128 (TAK-228) and the PDPK1 inhibitor GSK-2334470 (Data S1, Figure S4D) (34, 35). All inhibitors achieved nearly-complete inhibition of AKT activity at sub-micromolar concentrations, indicating their potency. Specificity of these results was shown by the lack of response to the BTK inhibitor acalabrutinib (Data S1, Figure S5A) at concentrations at which it inhibits calcium flux induced by BCR crosslinking in GCB-DLBCL lines (Data S1, Figure S5B). However, in DLBCL cell lines of the activated B-cell (ABC) subtype, some of which constitutively utilize antigen-driven BCR signaling to activate BTK (36), acalabrutinib showed dose-dependent inhibition of AKT activity (Data S1, Figure S5C).

The assay was able to perform kinetic monitoring of AKT activity, similar to an assay for calcium flux, by data acquisition immediately after the addition of reagents. After the addition of ipatasertib, maximal inhibition of baseline AKT kinase activity was reached in minutes (Figure 1(E)), implying that the reporter is dephosphorylated by an active process in the absence of AKT activity, despite the high affinity of the FHA1 domain for phosphorylated threonine (estimated at KD = 61–73 nM (37)). The reporter also detected rapid increases in AKT kinase activity in GCB-DLBCL lines after BCR crosslinking by antibodies, mimicking antigen-induced BCR signaling, above their baseline *E* dependent on tonic BCR signaling. Kinetic monitoring showed that the maximum increase in AKT activity, by ~3 times the baseline $\Delta E$ between active and inactive reporters, is reached in minutes (Figure 1(F)); a time course showed that this maximal level

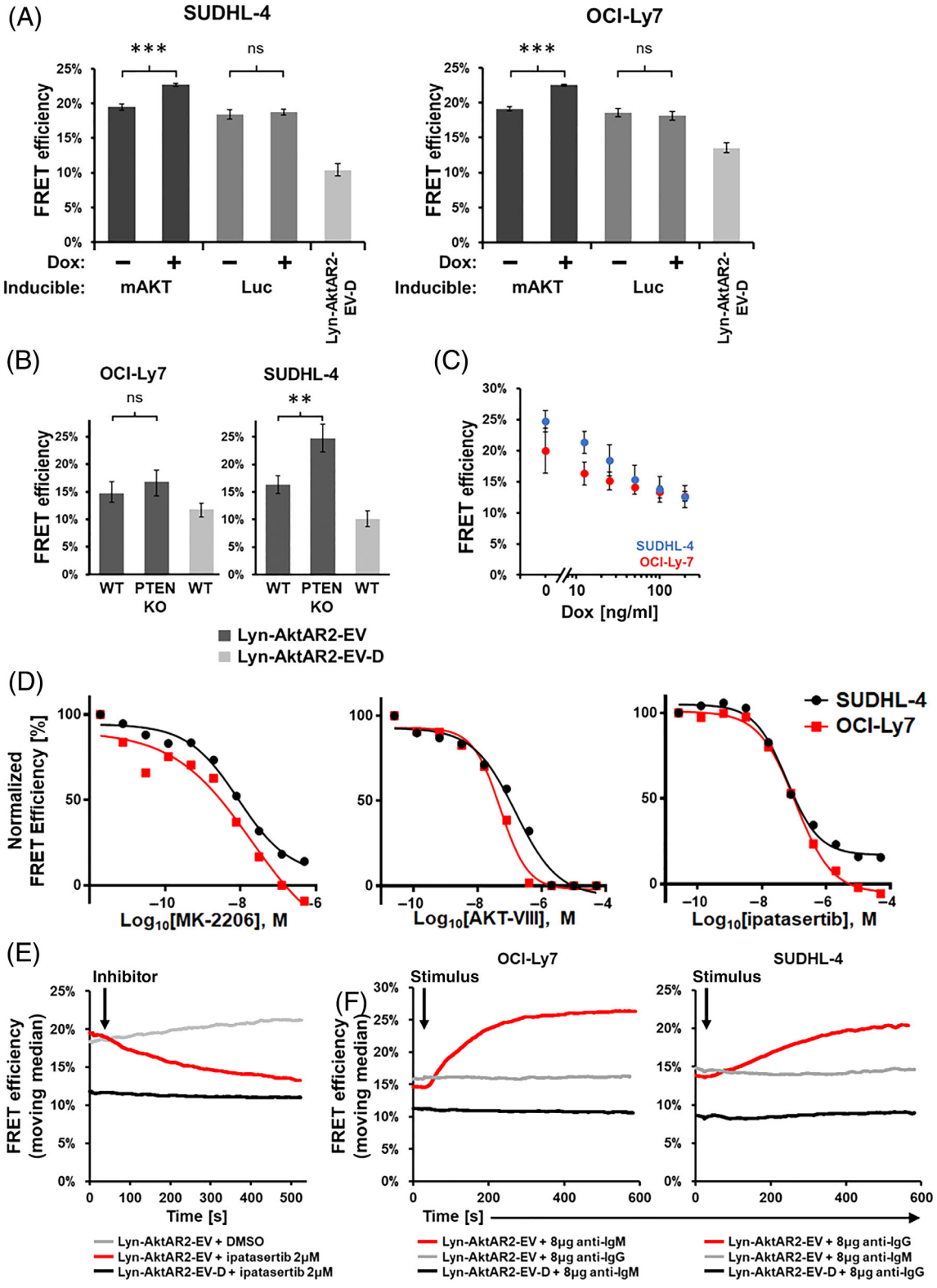


**FIGURE 1** Legend on next page.

was sustained for ~2 h, declining to baseline after 8–24 h (Data S1, Figure S5D).

The studies above suggested that this reporter assay might also be able to assess the effect of inhibitors of kinases mediating AKT activation by BCR crosslinking. As an example, we used kinetic monitoring to determine the effect of pre-incubation with the SYK inhibitor P505-15 on the AKT activity response to anti-BCR. Although pre-incubation lowered the AKT activity somewhat, due to the fact that such inhibitors also inhibit the baseline activation of AKT by tonic BCR signaling in GCB-DLBCL lines, this provided a new baseline against which dose-dependent inhibition of the BCR crosslinking-induced rise in AKT activity could be measured (Data S1, Figures S5E and S5F).

### 3.6 | Changing the target peptide creates a reporter of PKA activity

To demonstrate that a FRET-based reporter and FCM can be used to measure the activity of a kinase other than AKT, we first created a transposon-based vector (LPAR) for expression of a Lyn-tagged reporter, identical to the Lyn-AktAR2-EV reporters except that the AKT substrate FOXO1 peptide has been replaced by an AarI cassette for seamless cloning. Into the LPAR vector, we then cloned target peptides for protein kinase A (PKA), a serine/threonine kinase, based on the AKAR2 reporter of PKA kinase activity (26), with either a central Thr residue (active reporter, LPAR-AKAR-WT) or Val (inactive reporter, LPAR-AKAR-mt) (Figure 2(A)).

We validated this PKA reporter in GCB-DLBCL lines by several manipulations that have known effects on PKA. Forskolin, an activator of adenylyl cyclases, is commonly used to elevate intracellular levels of cyclic adenosine 3′,5′-monophosphate (cAMP), a "second messenger" that allosterically stimulates PKA kinase activity by promoting assembly of the tetrameric holoenzyme (38). In the OCI-Ly7 cell line, forskolin reproducibly increased *E* from LPAR-AKAR-WT, without a change in *E* from LPAR-AKAR-mt, in a classic dose–response pattern (Figure 2(B)). cAMP is normally hydrolyzed by phosphodiesterases (39), among which PDE4B is a prominent member in DLBCL cells (40). Similar to the effect of forskolin, *E* from LPAR-AKAR-WT was increased by two PDE4 inhibitors, RS25344 (41) and FDA-approved roflumilast (42), without affecting LPAR-AKAR-mt, while the PKA inhibitor KT5720 produced a slight reduction (Figure 2(C)).

PKA is well-established as an important negative regulator of signaling by the T-cell receptor (43, 44), but its role in BCR signaling is understood less well (45). We found that BCR crosslinking by antibodies, mimicking antigen-induced BCR signaling, elevated *E* from LPAR-AKAR-WT in GCB-DLBCL lines, over a time course (Figure 2 (D)) similar to that of AKT activation by BCR crosslinking (Data S1, Figure S5D). Aguiar and colleagues showed that forskolin and PDE4 inhibitors increased cAMP levels in DLBCL cell lines, presumably also increasing PKA activity, resulting in inhibition of the BCR signaling mediator SYK (46), with the further consequence that the BCR signaling mediator PI3K is also inhibited (47). SYK has been shown to inhibit PKA activity in breast cancer cells by phosphorylating Y330 of the PKA catalytic subunit (48), but others reported that PKA activity was increased by phosphorylation of the same site by receptor tyrosine kinases in other non-lymphoid cell types (49). In GCB-DLBCL lines, we found that the SYK inhibitor P505-15 reduced basal *E* from LPAR-AKAR-WT and blocked its increase by BCR crosslinking (Figure 2(E)). This indicates that SYK, which is activated by both the tonic (18) and antigen-induced types of BCR signaling (Data S1, Figures S5E and S5F), promotes PKA activity as an additional consequence of BCR signaling, possibly providing negative feedback to dampen BCR signaling.

### 3.7 | Evaluating reporter FRET by SFCM

Because FRET assessment by FCM requires data post-processing, we investigated whether spectral flow cytometry (SFCM) with real-time channel unmixing may provide a useful alternative. SFCM measures fluorescence in multiple channels for each exciting laser, whose

**FIGURE 1** Effects on FRET of AKT kinase activity reporters of stable knockout and/or inducible expression of proteins affecting AKT activity. (A) 48 h of doxycycline (Dox)-induced expression of a constitutively active form of AKT (myristoylated murine AKT1, mAKT) increases FRET efficiency (*E*) of a "live" (active) AKT activity reporter (Lyn-AktAR2-EV) in two GCB-DLBCL lines. No increase in *E* is seen after induction of a control protein (luciferase, Luc). Baseline *E* of a "dead" (inactive, non-phosphorylatable) AKT activity reporter (Lyn-AktAR2-EV-D) is shown for comparison. The absolute increase of *E* with induction of MyrAKT versus Luc was 10.8% versus 0.5% in SUDHL-4, and 8.3% versus 0.4% in OCI-Ly7. Means of three biological replicates are displayed; error bars represent the *SD* (***$p < 0.001$; two-tailed paired *t*-test). (B) *E* of the active reporter is increased by stable PTEN knockout in the same GCB-DLBCL lines, with baseline *E* of the inactive reporter shown for comparison. The absolute increase of *E* with PTEN KO was 1.4% in OCI-Ly7 and 7.8% in SUDHL-4. Means of four biological replicates are displayed; error bars represent the *SD* (**$p < 0.01$; two-tailed paired *t*-test). (C) In two GCB-DLBCL lines with stable PTEN knockout and a Dox-inducible expression vector for PTEN re-expression, *E* of the active reporter is decreased by increasing concentrations of Dox. Means of three biological replicates are displayed; error bars represent the *SD*. (D) Dose–response curves of inhibition of AKT activity, measured with the active reporter, by ipatasertib and allosteric AKT inhibitors MK-2206 and AKT-VIII in two GCB-DLBCL lines. *E* values are normalized according to the range of *E* values between those of untreated cells with the active reporter (100%) or the inactive reporter (0%); negative values are attributed to measurement imprecision and noise. (E) Kinetic monitoring with the Lyn-AktAR2-EV active reporter shows rapid inhibition of baseline AKT activity by ipatasertib (final concentration, 2 μM) in the GCB-DLBCL line OCI-Ly7; there is no effect on FRET of the inactive reporter. (F) AKT activity of two GCB-DLBCL lines is rapidly increased by BCR crosslinking with antibodies specific for the immunoglobulin heavy chain (IgH) isotype expressed by each line; there is no effect on the inactive reporter, or with antibodies to other IgH isotypes [Color figure can be viewed at wileyonlinelibrary.com]

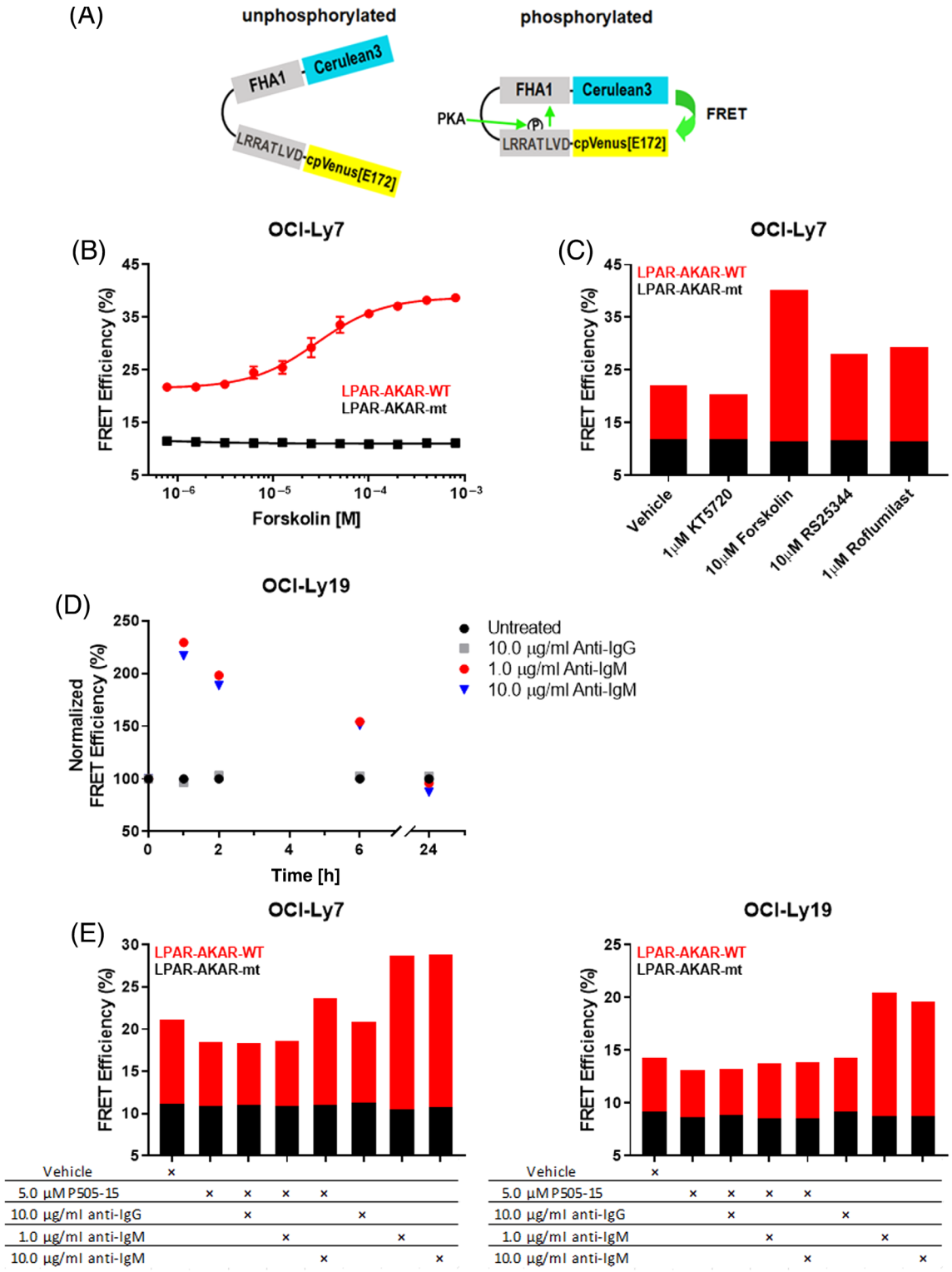


**FIGURE 2** Detection of PKA kinase activity by a FRET-based reporter. (A) Principle of the FRET-based reporter of PKA activity. Phosphorylation of threonine (T) in a peptide domain based on a known PKA target leads to its binding by the FHA1 domain of the reporter; this brings donor (Cerulean3) and acceptor (cpVenus[E172]) fluorophores of the reporter into greater proximity, and increases the FRET signal between them when illuminated. (B) Dose–response effect of forskolin (1-h incubation) on PKA kinase activity, reflected by *E* values of the active LPAR-AKAR-WT reporter, in the GCB-DLBCL line OCI-Ly7. Means of four biological replicates, performed on different days, are displayed; error bars represent the standard error of the mean. There is no effect of forskolin on the inactive LPAR-AKAR-mt reporter. (C) Effect of 1-h incubation with additional modulators of PKA activity: the PKA inhibitor KT5720, and two inhibitors of PDE4 phosphodiesterases (roflumilast and RS25344). (D) Time course of elevation in PKA activity, measured by LPAR-AKAR-WT, in response to specific BCR crosslinking antibody in the IgM-expressing GCB-DLBCL line OCI-Ly19. There is no response with antibodies to the IgG isotype. (E) Effect of the SYK inhibitor P505-15 and/or anti-BCR antibodies on PKA activity in GCB-DLBCL lines. Agents were used in 1-h incubations, plus a 15-min preincubation with P505-15 when used with anti-BCR antibodies. In both lines, SYK inhibition lowers basal and BCR crosslinking-induced PKA activity [Color figure can be viewed at wileyonlinelibrary.com]

combination constitutes a "spectral fingerprint" that is characteristic for each fluorophore (50, 51). For a reference, we first evaluated FRET determination on the Aurora spectral flow cytometer (Cytek Biosciences) by the three-channel method, using raw intensity values from three of the 48 channels to represent $I_{DD}$, $I_{DA}$, and $I_{AA}$ for post-acquisition calculation of $E$ by the method of Chen et al. $E$ values from the Aurora agreed well with corresponding $E$ values from the Fortessa for the low-FRET and high-FRET controls, and for resting cells with live or dead kinase activity reporters (Data S3, Table S3), confirming $E$ as an instrument-independent measure of FRET. The stability of moving median $\bar{E}$ values from the Aurora, over the wide range of reporter abundance selected for analysis, was similar to that from the Fortessa (Data S1, Figure S6A), but the Aurora provided greater precision in single-cell $E$ values (Data S1, Figure S6B), consistent with previous reports of less "spreading error" (21). The dose–response assessment of PKA activity stimulation by forskolin on the Aurora (Data S1, Figure S6C) was similar to results on the Fortessa (Figure 2(B)).

We then used the full set of fluorescence measurements by the Aurora, and its built-in capability of spectral unmixing, to evaluate real-time display of FRET assessment. When multiple fluorophores are used in combination, unmixing algorithms use their spectral fingerprints to determine their respective contributions to the total "raw" fluorescence of each event, and thus their intensity values. To apply spectral unmixing for FRET assessment (SU-FRET), we used cells bearing low-FRET or high-FRET controls to generate spectral fingerprints, respectively designated FRET-Low and FRET-High (Data S1, Figure S7A), and added them to the library of fluorophore spectra in the SpectroFlo software. With these fingerprints, the instrument can unmix the fluorescence of reporter-bearing cells into an intensity-weighted linear combination of FRET-Low and FRET-High emission (and autofluorescence). Those intensities are calculated in real-time, and displayed in an orthogonal 2-parameter plot. As expected, the calculated intensities of low-FRET and high-FRET control cells lie along the two axes of this plot, defining an easily-visualized range of FRET in which reporter cells lie somewhere in-between (Figure 3(A)).

Among notable features of SU-FRET, prominent is that it provides much better discrimination between different states of FRET than is possible with the real-time alternative of a "FRET ratio" (Figure 3(B)). In addition, a greater spread of SU-FRET values is seen for the live PKA reporter than for the dead reporter or the low-FRET and high-FRET controls (Figure 3(B)); a similar greater spread was seen for the live AKT reporters by the three-channel method, at least with the Aurora (Data S1, Figure S6B). Since a change in FRET can only occur for the live reporter, as its level of phosphorylation changes, this suggests that there is baseline biological variability in the activity of these kinases. Finally, although SU-FRET does not directly yield an $E$ value, we found a remarkably linear relationship between a derivative of the unmixed FRET-Low and FRET-High intensities of reporter-bearing cells and their $E$ values (Data S1, Figure S7B).

We performed several tests to confirm the validity of SU-FRET, relying on the predictable increase in AKT activity caused by BCR crosslinking. When OCI-Ly7 cells expressing Lyn-AktAR2-EV were either left untreated or stimulated with non-fluorescent anti-BCR, then washed and mixed in different proportions, distinct populations were seen on the SU-FRET dot plot, and the proportions of cells identified in regions of lower or higher SU-FRET matched their expected proportions (Data S1, Figure S8A). We then tested whether the distinction between BCR-stimulated and unstimulated reporter-bearing cells by SU-FRET could be simultaneously verified by using fluorescently-labeled anti-BCR. We found that the increase in SU-FRET from Lyn-AktAR2-EV was the same when using anti-BCR labeled with Alexa Fluor 647 (AF647), whose excitation and emission spectra are separated well from those of C3 and cpV, as when using unlabeled anti-BCR; similarly, the binding of AF647-labeled anti-BCR did not change SU-FRET from Lyn-AktAR2-EV-D (Data S1, Figure S8B). Since SU-FRET from the AKT reporter was free from interference by AF647, we mixed Lyn-AktAR2-EV cells that were either unstimulated or stimulated with AF647-labeled anti-BCR, and found that AF647 signal (indicative of BCR crosslinking) marked cells with increased SU-FRET (Data S1, Figure S8C). This also made possible a kinetic assay to demonstrate that the binding of AF647-labeled anti-BCR precedes AKT activation, detected post facto by an increase in $E$ or the "SU-FRET ratio" of unmixed intensities (FRET-High/FRET-Low; Data S1(Figure S8B)), or in real time by two-parameter mapping of SU-FRET (Movie S1).

In addition to providing a real-time assessment of FRET, SU-FRET differs from FCM-FRET in requiring no additional efforts to allow the use of additional or multiple fluorophores, even when spectrally similar to the FRET donor and acceptor. We compared spectral unmixing and three-channel methods in kinetic assays after the addition of anti-BCR to cells that were either otherwise-unlabeled or labeled with fluorophores with increasing spectral similarity to cpV: AF647, phycoerythrin (PE), or DyLight 488 (Data S1, Figure S9A). Binding of DyLight 488-labeled anti-BCR interfered with the three-channel method, producing an artifactual increase in FRET from Lyn-AktAR2-EV, as compared to unlabeled anti-BCR and the other fluorophores, but SU-FRET was equivalent with all fluorophores (Data S1, Figure S9B). After finding that SU-FRET from Lyn-AktAR2-EV was stable when cells are placed on ice (Data S1, Figure S9C), we placed unstimulated AKT reporter-bearing cells on ice, and either left them unstained or stained them with a panel of differently-labeled antibodies to B-cell surface markers (Data S1, Figure S9D), resembling the type of multiparameter staining often used to define subsets of hematopoietic cells (52). SU-FRET from Lyn-AktAR2-EV was the same for both sets of cells (Figure 3(C)), indicating that SU-FRET was unaffected by those additional fluorophores, or by anti-BCR when used on ice.

### 3.8 | Using spectrally-unmixed FRET (SU-FRET) in studies of gene knockout

Our previous studies of gene KO (Figure 1 and (18)) utilized delivery of plasmids via electroporation, which is typically successful in only a fraction of cells, and associated with varying degrees of toxicity. We

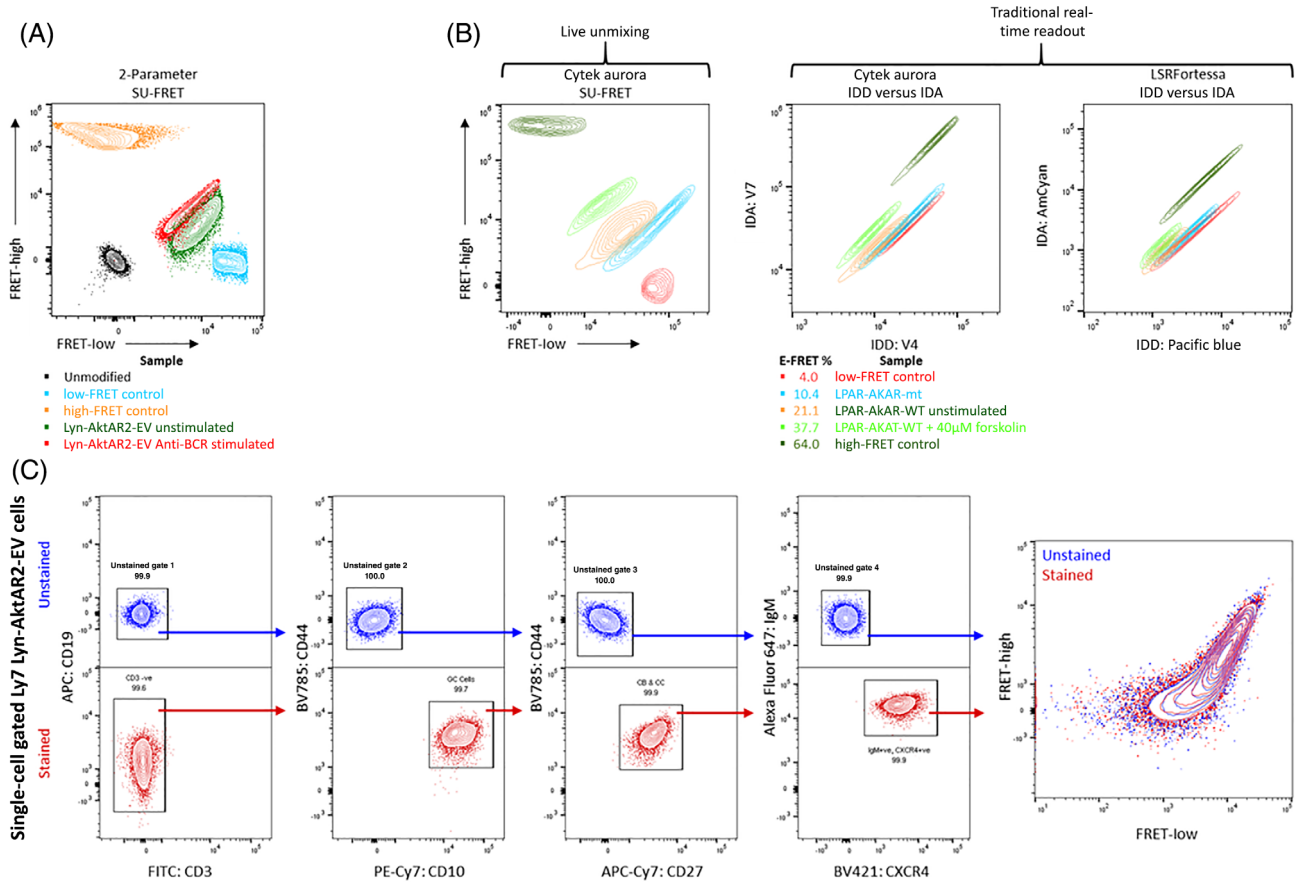


**FIGURE 3** Spectrally-unmixed FRET (SU-FRET) discriminates differences in FRET, in real time and without interference from other fluorophores. (A) Principle of SU-FRET. The fluorescence of cells with FRET reporters or controls is measured by the Cytek Aurora spectral flow cytometer and unmixed in real time into a linear combination of intensities of FRET-Low and FRET-High emission, displayed in an orthogonal two-parameter plot. The calculated intensities of low-FRET and high-FRET control OCI-Ly7 cells lie along the two axes of this plot, as expected, whereas those of cells expressing the live AKT activity reporter (Lyn-AktAR2-EV) lie somewhere in-between. Unmodified cells are at the origin. (B) FRET from OCI-Ly7 cells expressing controls or PKA reporters, including strong PKA stimulation of the live reporter with forskolin, determined in real time. SU-FRET (left panel) provides superior discrimination of FRET differences, as compared to assessment by a "FRET ratio" (center and right panels). (C) Independence of SU-FRET from other fluorophores. OCI-Ly7 cells with the Lyn-AktAR2-EV reporter were treated as two groups, either unstained (top panels) or stained with labeled antibodies (bottom panels) recognizing B-cell surface markers (CD19-APC, CD44-BV785, CD10-PE-Cy7, CD27-APC-Cy7, CXCR4-BV421, and IgM-AF647) or the T-cell marker CD3 (FITC-labeled). Single-cell events from both groups were gated first by FSC-A versus SSC-A and then FSC-A versus FSC-H (not shown). Gated events from the two groups were then separately and sequentially gated by the antibody combinations shown, from left to right. The unmixed High-FRET and Low-FRET intensities for final gated events from the stained and unstained groups were then overlaid in different colors in the SU-FRET contour plot at the far right, demonstrating no change in SU-FRET due to the presence of other fluorophores [Color figure can be viewed at wileyonlinelibrary.com]

therefore tested the use of lentiviral transduction for KO of genes involved in BCR signaling and/or AKT activity. We first used a single lentivirus for stable expression of both Cas9 and a guide RNA (gRNA), along with resistance to the rapidly-toxic antibiotic puromycin. Only a small proportion of OCI-Ly7 cells bearing the Lyn-AktAR2-EV reporter were initially resistant to puromycin, but these were expanded and then examined for their SU-FRET response to BCR stimulation with AF647-labeled anti-IgM. Targeting of CXCR4 was used as a negative control, since its KO by electroporation was previously shown to have no effect on AKT activity in GCB-DLBCL lines (18), and almost all CXCR4-targeted cells bound by anti-IgM were found in a region of high SU-FRET (Figure 4(A)), indicating preservation of the AKT response to BCR stimulation. With a viral gRNA targeting two of the three genes of human AKT (AKT1 and AKT2), a large fraction of cells binding IgM failed to increase their SU-FRET, suggesting that KO of AKT1/2 had occurred, but only in a subset of cells. This was supported by findings in cells with targeting of IGHM, used as a positive control because IgM is required for BCR expression and stimulation: only a fraction of cells showed reduced IgM staining, but those cells also failed to show increased SU-FRET (Figure 4(A)).

Because the combined Cas9/gRNA virus gave low transduction efficiency and incomplete KO, we tested a lentivirus expressing only gRNA and puromycin resistance in AKT reporter-bearing OCI-Ly19 cells that had also been engineered for Dox-inducible expression of Cas9. After puromycin selection, Dox was added and cells were evaluated by SFCM over several days for SU-FRET, before and after

ISAC CYTOMETRY Journal of Quantitative Cell Science PART A

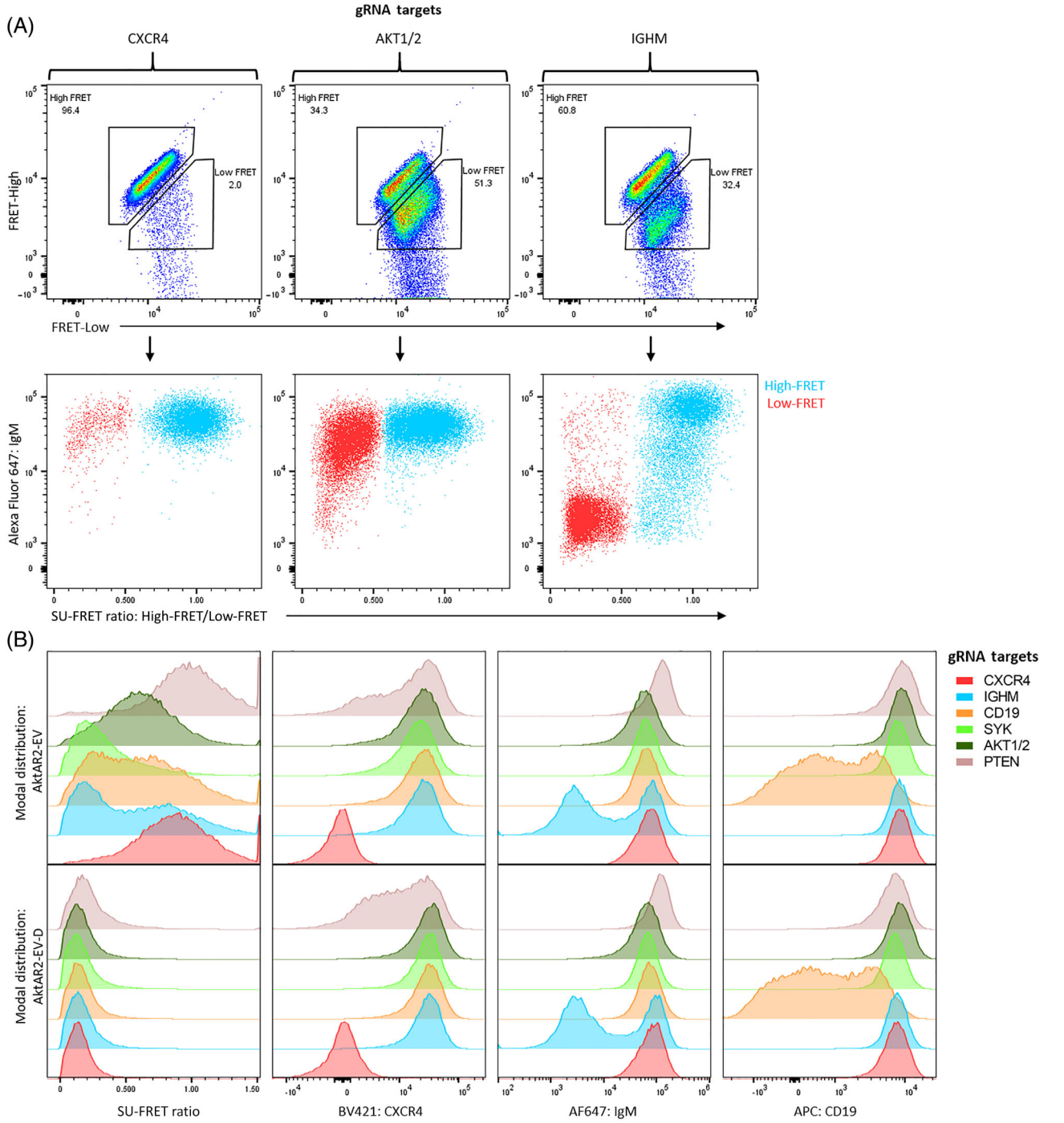


**FIGURE 4** SU-FRET detects effects of gene knockout on AKT activation by BCR signaling. (A) SU-FRET response to BCR crosslinking varies with the gene targeted and the degree of knockout (KO). Lentiviral vectors were used to deliver Cas9 protein, puromycin resistance, and a guide RNA (gRNA) targeting the genes shown in OCI-Ly7 cells expressing Lyn-AktAR2-EV. Puromycin-resistant cells were then stimulated with AF647-labeled anti-IgM (1 μg/ml for 10 min) and analyzed for SU-FRET response. There was no effect of targeting CXCR4, but targeting IGHM was inhibitory to cells in which KO was achieved, as shown by the level of surface IgM. (B) Effect of gRNAs targeting various genes relevant to AKT activation by BCR signaling, on OCI-Ly19 cells with live (top row) and dead (bottom row) AKT reporters. Lentiviral vectors were used to deliver gRNAs and puromycin resistance, in cells with Dox-inducible Cas9. SFCM data were obtained 5 days after Dox addition, and at 60 min after stimulation with AF647-labeled anti-IgM (1 μg/ml). SU-FRET is displayed as the per-cell ratio (FRET-High/FRET-Low) of unmixed intensities (left panels); other panels show surface expression of three targeted genes [Color figure can be viewed at wileyonlinelibrary.com]

periods of acute anti-BCR stimulation. Cells were also evaluated for the expression of targeted proteins: surface-detectable proteins (IgM, CXCR4, and CD19) were stained and detected simultaneously with SU-FRET measurement, while intracellular proteins (SYK, AKT, and PTEN) were stained in separate, parallel aliquots after fixation and permeabilization. Five days after Dox addition, BCR stimulation

produced increases in SU-FRET from Lyn-AktAR2-EV (but not Lyn-AktAR2-EV-D), to a degree that varied as expected with the function of the gene targeted, but also with the uniformity and degree of the KO and protein loss achieved, which we attribute to differences in gRNA efficiency. As before, targeting IGHM produced loss of surface IgM in only a fraction of cells, which showed less SU-FRET response to BCR stimulation (Figures 4(B), Data S1 (Figures S10A and S10B)). However, CXCR4 was lost in all cells, with preservation of their response to anti-BCR as expected (Figures 4(B) and Data S1, Figure S10B). The entire population of SYK-targeted cells showed reduced SU-FRET response to anti-IgM by 10 min (Data S1, Figure S10C), consistent with uniform loss of SYK protein (Data S1, Figure S10B) and its known critical role in BCR signal transduction. A fraction of PTEN-targeted cells showed increased basal SU-FRET with Lyn-AktAR2-EV (Data S1, Figure S10C), as expected from stable KO studies (Figure 1) and its role as a negative regulator of AKT activation, and consistent with staining that showed PTEN protein loss in only a fraction of cells (Data S1, Figure S10B). A fraction of PTEN-targeted cells also showed a reduction in surface CXCR4 (Figure 4(B)), consistent with the negative regulation of CXCR4 transcription by AKT (18). Surface CD19 protein was lost from all CD19-targeted cells, but to a highly variable degree at 5 days of Dox, and CD19-targeted cells showed only a modest reduction in SU-FRET response to anti-IgM, which was even less at shorter durations of stimulation (Data S1, Figures S10B and S10C). AKT-targeted cells showed only a modest reduction in SU-FRET response to anti-IgM, likely because only two of the three AKT genes were targeted by the gRNA used.

The results of this KO experiment suggest that if an SFCM instrument with sorting capability were available, a gRNA library screen could be done to identify genes whose KO has an effect detectable by changes in SU-FRET. To support this, and present the results more succinctly, we combined the SFCM results for Lyn-AktAR2-EV from all six gRNAs, separately for unstimulated cells and at 60 min after BCR stimulation, as if they had been acquired from a single culture (Data S1, Figure S11A). We then analyzed the results by gating first on defined regions of SU-FRET, and then by surface IgM and CD19 status. For unstimulated cells, regions of normal, high and low basal FRET were set based on the CXCR4-KO negative control (Data S1, Figure S11B); for BCR-stimulated cells, regions of high and low were set based on the populations of unmodified and BCR-KO cells in the IGHM-targeted positive control (Data S1, Figure S11C). For each gRNA, the numbers of events in each region were "scaled" as a percentage of all events for that gRNA, to normalize differences between gRNA species in the number of events acquired (Data S1, Figure S11D and Data S3, Tables S4–S7). In the unstimulated sample, cells with elevated SU-FRET were found to be highly enriched for PTEN gRNA (Figure 5(A)), even though KO of PTEN protein was only partial (Data S1, Figure S10B). BCR-stimulated events with low SU-FRET (representing cells with impaired AKT activation) were enriched for CD19 and IgM gRNAs in regions with respective loss of those proteins, as expected, and for SYK gRNA in cells with retained expression of CD19 and IgM (Figure 5(B)). Events with high SU-FRET were similarly enriched for CD19 and IgM gRNAs in regions with respective loss of those proteins, but depleted of SYK gRNA in cells with retained CD19 and IgM expression.

## 4 | DISCUSSION

FRET is a potentially quantitative indicator of proximity between donor and acceptor fluorophores in the 1–10 nm range, well below the ~20 nm limit of resolution of super-resolution fluorescence imaging microscopy methods such as stochastic optical reconstruction microscopy. With proper assay design, donor-acceptor proximity and/or orientation change can directly reflect a biomolecular phenomenon, such as protein–protein interaction (8, 53), protein-membrane proximity (54, 55), or protein conformation (56, 57), or enable an artificial construct to report indirectly on a phenomenon such as the enzymatic activity of a kinase or protease (58). FRET reporters are well-established for the reliable measurement of kinase activity (16, 17), and provide many advantages: fast response, desirable for real-time studies; application to single live cells, thereby maintaining cellular context and allowing kinetic analyses and the analysis of subpopulations; low cost per assay, since no reagents are needed for signal detection; parallel use of a non-phosphorylatable reporter, as a control (23); and flexible application to different kinases, by changing the target peptide used.

FRET is therefore a powerful tool that has been used in many studies of cell biology, as well as for molecular studies in vitro. However, the full application of FRET to cell biology research has been hindered by requirements for specialized instrumentation and data processing, and the low throughput or cell immobilization required for fluorescence microscopy. Because FCM is well-established, widely available for measuring fluorescence in cell biology research, and has high throughput capability, it is desirable for FRET-based applications. FCM has been used to assess intensity-based FRET, but most commonly by a simple FRET ratio ($I_{DA}$ vs. $I_{DD}$) that is instrument-dependent. Using spectral corrections and other calibrations, determination of the apparent FRET efficiency ($E$) by FCM has been shown to measure FRET with high reliability and in instrument-independent terms (5, 6), including from FRET-based kinase activity reporters (18, 59). (FRET by fluorescence lifetime can also be measured by FCM, although custom instrumentation and analysis are required (60, 61).) Processing FCM-generated data for the calculation of $E$ is required, for which we and others (62, 63) have provided software to expedite the task. Furthermore, FRET measurement by FCM is suitable for applications other than kinase activity reporters, such as protein–protein interaction (8, 53). Recently-developed single-fluorophore biosensors can also report on kinase activity, and should be suitable for FCM (64–66).

As we have shown, FRET assessment by FCM can be a valuable tool for studies of cell biology. However, with current commercially-available instruments and software, determination of $E$ by FCM cannot be done in real time, thereby limiting FRET-based sorting to the less-informative FRET ratio. Perhaps more importantly, limited sampling of the emission spectrum by FCM, combined with tediousness

ISAC CYTOMETRY Journal of Quantitative Cell Science PART A

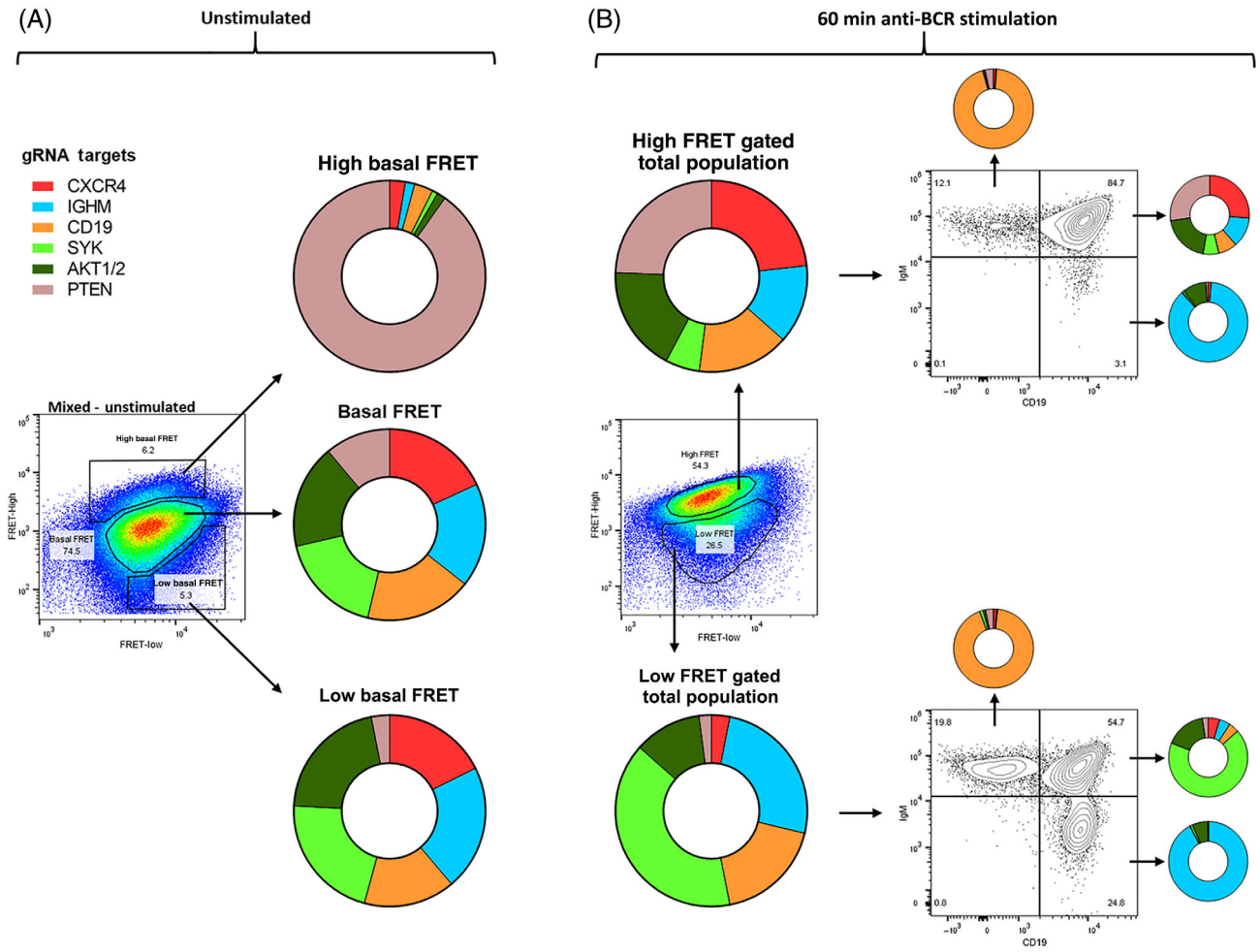


**FIGURE 5** Gating on SU-FRET implicates genes regulating AKT activation. (A) Combined SFCM data from the KO experiment shown in Figure 4(B), for unstimulated cells bearing the live AKT reporter. In SU-FRET regions based on cells with gRNA targeting the negative control CXCR4, donut plots show the scaled proportions of cells according to gRNA-targeted genes. Cells with high basal SU-FRET are found to be enriched for cells with targeting of PTEN. (B) Similar to A, but for the live reporter sample at 60 min after AF647-labeled anti-IgM (1 μg/ml). Cells were gated first by SU-FRET response to BCR stimulation, and then by surface expression of IgM and/or CD19. SYK gRNA is enriched in low-response cells that retain the expression of IgM and CD19. Among cells with normal SU-FRET response to BCR stimulation, the SYK gRNA proportion is reduced [Color figure can be viewed at wileyonlinelibrary.com]

of cross-talk compensation, makes the use of FRET in the presence of other fluorophores rather difficult. We found that these problems are overcome by SFCM, whose built-in spectral unmixing feature enables real-time precise and sensitive discrimination between cells with different FRET levels. Assessing FRET by spectral unmixing (SU-FRET) is simple, requiring only one-time data acquisition from cells expressing low-FRET or high-FRET constructs and unmodified cells. With the increasing availability of instruments capable of SFCM, which improves discrimination between fluorophores, the simplicity of SU-FRET may increase the use of FRET in cell biology research, especially with the ability to employ additional fluorophores. For example, SU-FRET may enable transgenic FRET reporters to be evaluated in cell subsets that require multiple fluorophores to define, such as many types of hematopoietic cells.

SU-FRET also provides a non-graphical index of FRET, through the SU-FRET ratio of unmixed FRET-High and FRET-Low intensities; however, this is not the same as *E*, although it could be used to estimate *E* from a calibration (Data S1, Figure S7B), nor is it similarly independent of instrumentation or experimental conditions. One obvious conditional factor is the choice of low-FRET and high-FRET controls that provide spectral fingerprints for unmixing; the controls that we used varied greatly in their FRET efficiency (*E* values of ~5% and ~65%, respectively). Using controls that encompass a more narrow range of *E*, as might be accomplished empirically with linkers of slightly different lengths to separate the donor and acceptor fluorophores (5), might expand the graphical separation between samples with intermediate *E* values. Likewise, substituting the low-FRET control with a zero-FRET one would extend the dynamic range of SU-FRET to E values below 5%. An additional potential limitation of SU-FRET is that it has not yet been shown to be reliable for non-stoichiometric FRET systems, such as to monitor protein:protein interactions in cells, in which donor and acceptor fluorophores are

attached to different proteins rather than stoichiometrically linked in a single reporter construct. In such situations, the spectral signatures of low-FRET and high-FRET controls may be insufficient to calibrate FRET signatures across variable acceptor-to-donor ratios, and therefore this more general type of FRET application is currently best served using the quantitative E-FRET method. However, as compensation for these limitations, SU-FRET is simple to use, gives results in real time, and facilitates the use of multiple fluorophores. Data S1 (Table S8) presents features of the three-channel and SU-FRET methods in parallel.

We focused our study of FRET by flow cytometry on the use of reporters of kinase activity, which is of widespread interest in diverse areas such as cell signaling, metabolism, and drug development. Many methods used to assess kinase activity have significant shortcomings, such as low throughput, loss of cellular context, or applicability only to cells in aggregate. Because AKT kinase activity is promoted by phosphorylation at certain highly-conserved AKT residues (Ser473 and Thr308 of AKT1), detection by specific antibodies is often used as a surrogate indicator of AKT activity. However, we found that this did not provide results that agreed with other evidence of AKT activity, in contrast to using FCM with AktAR2-based reporters (18). pS473 may be an especially poor surrogate for AKT kinase activity, being less reliable than pT308 (67) or rendered non-essential by phosphorylation of S477 and T479 (25), and both S473 and T308 are paradoxically hyperphosphorylated after treatment with ATP-competitive AKT inhibitors (68), whose effect on AKT activity was reliably detected by FCM and AktAR2-based reporters.

With the PKA reporter, we found a particular mechanism by which BCR signaling and PKA activity are interconnected. In its function as a negative regulator of BCR signaling, PKA activity is increased by cAMP after BCR signaling, perhaps through PTGER4, which is strongly induced by BCR crosslinking (69). PTGER4, a receptor for prostaglandin E2, generates cAMP in B cells (70) and has a negative effect on the proliferation of normal mouse B cells and human B cell lymphoma, for which it may function as a tumor suppressor (69). However, we found another mechanism by which BCR signaling activates PKA, enabling it to function as a negative regulator of BCR signaling: PKA phosphorylation by BCR-activated SYK. Previous reports differed as to whether phosphorylation of the PKA catalytic subunit, likely at Y330 and mediated by SYK in B cells, was activating (49) or inhibitory (48) of PKA kinase activity; our reporter studies showed that inhibition of SYK, which is activated by both tonic and antigen-induced BCR signaling, inhibited PKA activity in GCB-DLBCL lines.

An exciting possibility suggested by our studies is that cells could be sorted on the basis of functional difference detectable by a real-time assay based on SU-FRET. The example that we modeled was one that could be used to detect genes involved in the increase of AKT activity by acute BCR stimulation; after introduction of a library of gRNA species, cells with less BCR-induced increase in SU-FRET from a live AKT reporter could be sorted and analyzed for their gRNA composition, thus implicating genes necessary for the normal increase. It is plausible that a similar screen could be done with reporters specific for other kinases, or with other types of stimuli. Our example was somewhat complicated by not being able to achieve KO in all cells for some targeted genes, but in effect the resulting mixed cultures provided further evidence that SU-FRET can detect and discriminate the effect of KO in individual cells on the basis of FRET. Similarly, an actual full-library screen might suffer from incompleteness of KO for certain gRNA species targeting phenotype-essential genes, but that would not affect the true positivity of their representation in the population of cells sorted on the basis of SU-FRET.

The most prominent limitation of reporter assays is that cells must be engineered to express the reporter construct; this requires time and effort in advance of its use, may have unknown artifacts or non-physiologic aspects, and excludes certain applications, such as analysis of primary tumor or tissue samples. The results are also limited to providing an assessment of relative changes in activity of the enzyme interrogated, and not an absolute measure in biochemical terms. In addition, the performance of kinase activity reporters is highly dependent on the target peptide for specificity, and on subcellular localization for sensitivity. Specificity is an issue that has levels of complexity; in the case of AKT, AktAR2-based reporters are presumed to report on the combined activity of all AKT isoforms (although this has not been established), which is generally desirable but makes them unsuitable for studies of specific AKT isoforms. Similarly, the different isoforms of PKA are presumably all capable of phosphorylating the target peptide used in AKAR2, but it is well-known that PKA activity is often compartmentalized by A-kinase anchoring proteins (AKAPs); reporter localization, which is controlled by the Lyn peptide tag in our reporters, may therefore be especially important. In all cases, it is important to establish that a particular reporter performs as expected, reporting faithfully on activity of the kinase(s) in question; genetic and pharmacologic manipulations are important in this process, and validated the target peptides that we used respectively for AKT and PKA.

Among other limitations of our kinase reporter assays, using reporter phosphorylation (as reflected by FRET) to measure kinase activity depends on the assumption that reporter dephosphorylation is insignificant or unchanged between conditions being compared. This may not always be the case; we observed a rapid decline in $E$ from the active AKT reporter after AKT inhibition, implying that the $E$ value reflects a balance between reporter phosphorylation and active dephosphorylation. However, even if a change in $E$ is not solely due to kinase activity (i.e., is affected by a change in dephosphorylation), the reporter may ultimately provide relevant information about the net activity of the pathway in question. Finally, while it is advantageous that the reporter assay works well in live cells, we found that it does not work reliably in fixed cells (data not shown), limiting the collection of samples at different times for later batch analysis, although we did find that reporter signal was stabilized by keeping cells in the cold.

In summary, we have provided methods and applications that illustrate and extend the use of flow cytometry to measure FRET in live cells.

## ACKNOWLEDGMENTS

Cell sorting and other analyses were done at the MD Anderson Cancer Center Flow Cytometry Core Facility, supported by Cancer Center

Support Grant (CCSG) NCI P30 CA16672. Sanger sequencing was done by the MD Anderson Cancer Center Sequencing and Microarray Facility, supported by the CCSG. FRET microscopy studies were done at the Advanced Microscopy Core Facility, supported by NCI grant S10 RR029552. Dr. Zen Gong and Dr. Stephen Zhou of Cytek Biosciences provided a special version of SpectroFlo that allowed merging of raw and unmixed data, for determining FRET by both three-measurement and unmixed approaches.

## AUTHOR CONTRIBUTIONS

**Jared Henderson:** Conceptualization; data curation; formal analysis; funding acquisition; investigation; methodology; project administration; resources; software; supervision; validation; visualization; writing-original draft; writing-review & editing. **Ondrej Havranek:** Conceptualization; data curation; formal analysis; funding acquisition; investigation; methodology; project administration; resources; software; supervision; validation; visualization; writing-original draft; writing-review & editing. **Man Chun Ma:** Formal analysis; methodology; software. **Vaclav Herman:** Investigation; validation. **Kristyna Kupcova:** Investigation; validation. **Tereza Chrbolkova:** Investigation; validation. **Mariana Pacheco-Blanco:** Investigation; validation. **Zhiqiang Wang:** Investigation; validation. **Justin Comer:** Investigation; validation. **Tomasz Zal:** Conceptualization; data curation; formal analysis; investigation; methodology; software; supervision; validation; writing-review & editing. **Eric Davis:** Conceptualization; data curation; formal analysis; funding acquisition; investigation; methodology; project administration; resources; software; supervision; validation; visualization; writing-original draft; writing-review & editing.

## CONFLICT OF INTEREST

The authors have no competing interests to declare.

## ORCID

*Ondrej Havranek* https://orcid.org/0000-0001-5826-3557

*Richard Eric Davis* https://orcid.org/0000-0001-7311-0065

## REFERENCES

1. Algar WR, Hildebrandt N, Vogel SS, Medintz IL. FRET as a biomolecular research tool–understanding its potential while avoiding pitfalls. Nat Methods. 2019;16:815–29.
2. Lee HN, Mehta S, Zhang J. Recent advances in the use of genetically encodable optical tools to elicit and monitor signaling events. Curr Opin Cell Biol. 2020;63:114–24.
3. Bajar BT, Wang ES, Zhang S, Lin MZ, Chu J. A guide to fluorescent protein FRET pairs. Sensors. 2016;16:1488–511.
4. Zal T, Gascoigne NR. Photobleaching-corrected FRET efficiency imaging of live cells. Biophys J. 2004;86:3923–39.
5. Chen H, Puhl HL 3rd, Koushik SV, Vogel SS, Ikeda SR. Measurement of FRET efficiency and ratio of donor to acceptor concentration in living cells. Biophys J. 2006;91:L39–41.
6. Nagy P, Bene L, Hyun WC, Vereb G, Braun M, Antz C, et al. Novel calibration method for flow cytometric fluorescence resonance energy transfer measurements between visible fluorescent proteins. Cytometry A. 2005;67:86–96.
7. Coullomb A, Bidan CM, Qian C, Wehnekamp F, Oddou C, Albiges-Rizo C, et al. QuanTI-FRET: a framework for quantitative FRET measurements in living cells. Sci Rep. 2020;10:6504.
8. Hochreiter B, Kunze M, Moser B, Schmid JA. Advanced FRET normalization allows quantitative analysis of protein interactions including stoichiometries and relative affinities in living cells. Sci Rep. 2019;9:8233.
9. Annamdevula NS, Sweat R, Griswold JR, Trinh K, Hoffman C, West S, et al. Spectral imaging of FRET-based sensors reveals sustained cAMP gradients in three spatial dimensions. Cytometry A. 2018;93:1029–38.
10. Levy S, Wilms CD, Brumer E, Kahn J, Pnueli L, Arava Y, et al. SpRET: highly sensitive and reliable spectral measurement of absolute FRET efficiency. Microsc Microanal. 2011;17:176–90.
11. Lin F, Zhang C, Du M, Wang L, Mai Z, Chen T. Superior robustness of ExEm-spFRET to IIem-spFRET method in live-cell FRET measurement. J Microsc. 2018;272:145–50.
12. Megias D, Marrero R, Martinez Del Peso B, Garcia MA, Bravo-Cordero JJ, Garcia-Grande A, et al. Novel lambda FRET spectral confocal microscopy imaging method. Microsc Res Tech. 2009;72:1–11.
13. Ferrer-Font L, Pellefigues C, Mayer JU, Small SJ, Jaimes MC, Price KM. Panel design and optimization for high-dimensional Immunophenotyping assays using spectral flow cytometry. Curr Protoc Cytom. 2020;92:e70.
14. Robinson JP. Spectral flow cytometry-quo vadimus? Cytometry A. 2019;95:823–4.
15. Hochreiter B, Garcia AP, Schmid JA. Fluorescent proteins as genetically encoded FRET biosensors in life sciences. Sensors. 2015;15:26281–314.
16. Maryu G, Miura H, Uda Y, Komatsubara AT, Matsuda M, Aoki K. Live-cell imaging with genetically encoded protein kinase activity reporters. Cell Struct Funct. 2018;43:61–74.
17. Ni Q, Mehta S, Zhang J. Live-cell imaging of cell signaling using genetically encoded fluorescent reporters. FEBS J. 2018;285:203–19.
18. Havranek O, Xu J, Köhrer S, Wang Z, Becker L, Comer JM, et al. Tonic B-cell receptor signaling in diffuse large B-cell lymphoma. Blood. 2017;130:995–1006.
19. Zal T, Zal MA, Gascoigne NR. Inhibition of T cell receptor-coreceptor interactions by antagonist ligands visualized by live FRET imaging of the T-hybridoma immunological synapse. Immunity. 2002;16:521–34.
20. He L, Wu X, Simone J, Hewgill D, Lipsky PE. Determination of tumor necrosis factor receptor-associated factor trimerization in living cells by CFP->YFP->mRFP FRET detected by flow cytometry. Nucleic Acids Res. 2005;33:e61.
21. Niewold P, Ashhurst TM, Smith AL, King NJC. Evaluating spectral cytometry for immune profiling in viral disease. Cytometry A. 2020;97:1165–79.
22. Manning BD, Toker A. AKT/PKB signaling: navigating the network. Cell. 2017;169:381–405.
23. Gao X, Zhang J. Spatiotemporal analysis of differential Akt regulation in plasma membrane microdomains. Mol Biol Cell. 2008;19:4366–73.
24. Zhou X, Clister TL, Lowry PR, Seldin MM, Wong GW, Zhang J. Dynamic visualization of mTORC1 activity in living cells. Cell reports. 2015;10:1767–77.
25. Liu P, Begley M, Michowski W, Inuzuka H, Ginzberg M, Gao D, et al. Cell-cycle-regulated activation of Akt kinase by phosphorylation at its carboxyl terminus. Nature. 2014;508:541–5.
26. Zhang J, Hupfeld CJ, Taylor SS, Olefsky JM, Tsien RY. Insulin disrupts beta-adrenergic signalling to protein kinase a in adipocytes. Nature. 2005;437:569–73.
27. Ebner M, Lucic I, Leonard TA, Yudushkin I. PI(3,4,5)P3 engagement restricts Akt activity to cellular membranes. Mol Cell. 2017;65:416–31. e6.
28. Komatsu N, Aoki K, Yamada M, Yukinaga H, Fujita Y, Kamioka Y, et al. Development of an optimized backbone of FRET biosensors for kinases and GTPases. Mol Biol Cell. 2011;22:4647–56.
29. Kowarz E, Loscher D, Marschalek R. Optimized sleeping beauty transposons rapidly generate stable transgenic cell lines. Biotechnol J. 2015;10:647–53.

30. Covassin LD, Siekmann AF, Kacergis MC, Laver E, Moore JC, Villefranc JA, et al. A genetic screen for vascular mutants in zebrafish reveals dynamic roles for Vegf/Plcg1 signaling during artery development. Dev Biol. 2009;329:212–26.
31. Hirai H, Sootome H, Nakatsuru Y, Miyama K, Taguchi S, Tsujioka K, et al. MK-2206, an allosteric Akt inhibitor, enhances antitumor efficacy by standard chemotherapeutic agents or molecular targeted drugs in vitro and in vivo. Mol Cancer Ther. 2010;9:1956–67.
32. Jo H, Lo PK, Li Y, Loison F, Green S, Wang J, et al. Deactivation of Akt by a small molecule inhibitor targeting pleckstrin homology domain and facilitating Akt ubiquitination. Proc Natl Acad Sci U S A. 2011;108:6486–91.
33. Saura C, Roda D, Roselló S, Oliveira M, Macarulla T, Pérez-Fidalgo JA, et al. A first-in-human phase I study of the ATP-competitive AKT inhibitor Ipatasertib demonstrates robust and safe targeting of AKT in patients with solid tumors. Cancer Discov. 2017;7:102–13.
34. Ghobrial IM, Siegel DS, Vij R, Berdeja JG, Richardson PG, Neuwirth R, et al. TAK-228 (formerly MLN0128), an investigational oral dual TORC1/2 inhibitor: a phase I dose escalation study in patients with relapsed or refractory multiple myeloma, non-Hodgkin lymphoma, or Waldenstrom's macroglobulinemia. Am J Hematol. 2016;91:400–5.
35. Hsieh AC, Liu Y, Edlind MP, Ingolia NT, Janes MR, Sher A, et al. The translational landscape of mTOR signalling steers cancer initiation and metastasis. Nature. 2012;485:55–61.
36. Davis RE, Ngo VN, Lenz G, Tolar P, Young R, Romesser PB, et al. Chronic active B cell receptor signaling in diffuse large B cell lymphoma. Nature. 2010;463:88–92.
37. Durocher D, Henckel J, Fersht AR, Jackson SP. The FHA domain is a modular phosphopeptide recognition motif. Mol Cell. 1999;4:387–94.
38. England JP, Hao Y, Bai L, Glick V, Hodges HC, Taylor SS, et al. Switching of the folding-energy landscape governs the allosteric activation of protein kinase a. Proc Natl Acad Sci U S A. 2018;115:E7478–85.
39. Fertig BA, Baillie GS. PDE4-mediated cAMP Signalling. J Cardiovasc Dev Dis. 2018;5:8–21.
40. Smith PG, Wang F, Wilkinson KN, Savage KJ, Klein U, Neuberg DS, et al. The phosphodiesterase PDE4B limits cAMP-associated PI3K/AKT-dependent apoptosis in diffuse large B-cell lymphoma. Blood. 2005;105:308–16.
41. Saldou N, Obernolte R, Huber A, Baecker PA, Wilhelm R, Alvarez R, et al. Comparison of recombinant human PDE4 isoforms: interaction with substrate and inhibitors. Cell Signal. 1998;10:427–40.
42. Hatzelmann A, Morcillo EJ, Lungarella G, Adnot S, Sanjar S, Beume R, et al. The preclinical pharmacology of roflumilast–a selective, oral phosphodiesterase 4 inhibitor in development for chronic obstructive pulmonary disease. Pulm Pharmacol Ther. 2010;23:235–56.
43. Arumugham VB, Baldari CT. cAMP: a multifaceted modulator of immune synapse assembly and T cell activation. J Leukoc Biol. 2017;101:1301–16.
44. Wehbi VL, Tasken K. Molecular mechanisms for cAMP-mediated Immunoregulation in T cells–role of anchored protein kinase a signaling units. Front Immunol. 2016;7:222.
45. Cooney JD, Aguiar RC. Phosphodiesterase 4 inhibitors have wide-ranging activity in B-cell malignancies. Blood. 2016;128:2886–90.
46. Kim SW, Rai D, McKeller MR, Aguiar RC. Rational combined targeting of phosphodiesterase 4B and SYK in DLBCL. Blood. 2009;113:6153–60.
47. Cooney JD, Lin AP, Jiang D, Wang L, Suhasini AN, Myers J, et al. Synergistic targeting of the regulatory and catalytic subunits of PI3Kdelta in mature B-cell malignancies. Clin Cancer Res. 2018;24:1103–13.
48. Yu S, Huang H, Iliuk A, Wang WH, Jayasundera KB, Tao WA, et al. Syk inhibits the activity of protein kinase a by phosphorylating tyrosine 330 of the catalytic subunit. J Biol Chem. 2013;288:10870–81.
49. Caldwell GB, Howe AK, Nickl CK, Dostmann WR, Ballif BA, Deming PB. Direct modulation of the protein kinase a catalytic subunit alpha by growth factor receptor tyrosine kinases. J Cell Biochem. 2012;113:39–48.
50. Feher K, von Volkmann K, Kirsch J, Radbruch A, Popien J, Kaiser T. Multispectral flow cytometry: the consequences of increased light collection. Cytometry A. 2016;89:681–9.
51. Gregori G, Patsekin V, Rajwa B, Jones J, Ragheb K, Holdman C, et al. Hyperspectral cytometry at the single-cell level using a 32-channel photodetector. Cytometry A. 2012;81:35–44.
52. Kjeldsen MK, Perez-Andres M, Schmitz A, Johansen P, Boegsted M, Nyegaard M, et al. Multiparametric flow cytometry for identification and fluorescence activated cell sorting of five distinct B-cell subpopulations in normal tonsil tissue. Am J Clin Pathol. 2011;136:960–9.
53. von Kolontaj K, Horvath GL, Latz E, Buscher M. Automated nanoscale flow cytometry for assessing protein-protein interactions. Cytometry A. 2016;89:835–43.
54. Lee WY, Tolar P. Activation of the B cell receptor leads to increased membrane proximity of the Igalpha cytoplasmic domain. PLoS One. 2013;8:e79148.
55. Temmerman K, Nickel W. A novel flow cytometric assay to quantify interactions between proteins and membrane lipids. J Lipid Res. 2009;50:1245–54.
56. Caron NS, Munsie LN, Keillor JW, Truant R. Using FLIM-FRET to measure conformational changes of transglutaminase type 2 in live cells. PLoS One. 2012;7:e44159.
57. Sanabria H, Rodnin D, Hemmen K, Peulen TO, Felekyan S, Fleissner MR, et al. Resolving dynamics and function of transient states in single enzyme molecules. Nat Commun. 2020;11:1231.
58. Bozza WP, Di X, Takeda K, Rivera Rosado LA, Pariser S, Zhang B. The use of a stably expressed FRET biosensor for determining the potency of cancer drugs. PLoS One. 2014;9:e107010.
59. Doucette J, Zhao Z, Geyer RJ, Barra MM, Balunas MJ, Zweifach A. Flow cytometry enables multiplexed measurements of genetically encoded intramolecular FRET sensors suitable for screening. J Biomol Screen. 2016;21:535–47.
60. Alturkistany F, Nichani K, Houston KD, Houston JP. Fluorescence lifetime shifts of NAD(P)H during apoptosis measured by time-resolved flow cytometry. Cytometry A. 2019;95:70–9.
61. Houston JP, Yang Z, Sambrano J, Li W, Nichani K, Vacca G. Overview of fluorescence lifetime measurements in flow cytometry. Methods Mol Biol. 2018;1678:421–46.
62. Szaloki N, Doan-Xuan QM, Szollosi J, Toth K, Vamosi G, Bacso Z. High throughput FRET analysis of protein-protein interactions by slide-based imaging laser scanning cytometry. Cytometry A. 2013;83:818–29.
63. Szentesi G, Horvath G, Bori I, Vamosi G, Szollosi J, Gaspar R, et al. Computer program for determining fluorescence resonance energy transfer efficiency from flow cytometric data on a cell-by-cell basis. Comput Methods Programs Biomed. 2004;75:201–11.
64. Kawai Y, Sato M, Umezawa Y. Single color fluorescent indicators of protein phosphorylation for multicolor imaging of intracellular signal flow dynamics. Anal Chem. 2004;76:6144–9.
65. Liu W, Deng M, Yang C, Liu F, Guan X, Du Y, et al. Genetically encoded single circularly permuted fluorescent protein-based intensity indicators. J Phys D Appl Phys. 2020;53:113001.
66. Mehta S, Zhang Y, Roth RH, Zhang JF, Mo A, Tenner B, et al. Single-fluorophore biosensors for sensitive and multiplexed detection of signalling activities. Nat Cell Biol. 2018;20:1215–25.
67. Vincent EE, Elder DJ, Thomas EC, Phillips L, Morgan C, Pawade J, et al. Akt phosphorylation on Thr308 but not on Ser473 correlates

ISAC CYTOMETRY Journal of Quantitative Cell Science PART A

with Akt protein kinase activity in human non-small cell lung cancer. Br J Cancer. 2011;104:1755–61.
68. Okuzumi T, Fiedler D, Zhang C, Gray DC, Aizenstein B, Hoffman R, et al. Inhibitor hijacking of Akt activation. Nat Chem Biol. 2009;5: 484–93.
69. Murn J, Alibert O, Wu N, Tendil S, Gidrol X. Prostaglandin E2 regulates B cell proliferation through a candidate tumor suppressor, Ptger4. J Exp Med. 2008;205:3091–103.
70. Fedyk ER, Phipps RP. Prostaglandin E2 receptors of the EP2 and EP4 subtypes regulate activation and differentiation of mouse B lymphocytes to IgE-secreting cells. Proc Natl Acad Sci U S A. 1996;93: 10978–83.

## SUPPORTING INFORMATION

Additional supporting information may be found online in the Supporting Information section at the end of this article.